Measuring The Gravitational Field with an Atomic Ruler

Shijie Chai

Department of Physics

University of Otago

New Zealand

A thesis presented for the degree of

Doctor of Philosophy at the University of Otago

2018

To mum, dad and especially my wife.

Declaration

This thesis is an account of research undertaken between *December 2014* and *October 2018* at the Department of Physics, Division of Sciences, University of Otago, Dunedin, New Zealand under the supervision of Dr. Mikkel F. Andersen. Except where acknowledged in the customary manner, the material presented in this thesis is, to the best of my knowledge, original and has not been submitted, either in whole or part, for a degree at any university.

Shijie Chai

Acknowledgments

Through my Ph.D. journey, I find there are so many people I wish to thank.

First and foremost, I would like to thank my supervisor Dr. Mikkel F. Andersen. Without your support, I could not get this today. I always feel incredibly lucky to have had the opportunity to study and work in your group. You are knowledgeable and innovative. I am inspired by your enthusiasm for pursuing science and truth. Furthermore, the way you interpret science and technology are very inspiring and informative. Your deep understanding of nature reshapes the angle I view the world. I have learned so much from you ranging from theory to practice. Moreover, the high standard you set indeed pushes me to a new scope of my ability. Additionally, you are so nice and kind. The financial support you provided reduces tons of pressure for me to go through my Ph.D. journey. MIKKEL, THANK YOU!

To Julia, thank you a million for being my coach. You are a rigorous, hard-working, organized and supportive person. I learned a lot from you. The ability that you perform and implement experiments is impressive, so is your Hungarian cakes. I will never forget the efforts you dedicated and the help you offered which have turned out to be the treasures for my future researches. You are not only my teacher but also my friend. At this stage, I could not come up with anything else, but "THANK YOU"!

To Mim and Eyal, thank you for being the postdocs in the lab. You are friendly, smart and supportive who have given me lots of help during the last three years. The knowledge that you brought from your fields broaden my horizon. Additionally, the spirit you pursue science truly inspired me. Thank you!

To the rest of the Group: Fung, Adrian, Matt, Rhys, Luke, Carolyn, Jordan, Taren, Boom, Fluke, Phillip, Eric, Chris, Laura, Up and Marvin, it's delightful to work with you guys. Thank you for creating such a friendly and warm environment in a cold atom lab.

I'm going to miss you all.

To my Chinese friend Xiaoquan Yu, a theoretical physicist, thank you for explaining physics to me. Your enthusiasm and deep understanding of physics are impressive and unforgettable. I hope you have great success in your future researches.

To the fantastic people in the Physics Department, Amita, Bianca, Xavier, Maddy, Pat, Fan, Madhuri, Boyang, Steven, and so on, thank you for sharing equipment and experiences. To the members of the electronic and mechanical workshop: Peter S, Peter M, Barbara, Myles, thank you for all the help about the kit and piece you made. Without these, I could not finish my project. To the IT group Peter S and Simon, thank you for helping me with the computers. To administration staff, Brenda, Sandy, Diana, Anita, Bev, Shae and Nick, thank you so much for making things so organized.

To my neighbors: Sifen and Lixing, thank you. I am incredibly lucky to have you such a lovely couple to be my neighbors. Thank you for giving my wife and me the feeling of home.

Last but not least, to my loving and encouraging family: my parents, parents-in-law and my 91-year old grandmother who have given me tons of support and understanding. Thank you for never doubting my ability to succeed. Especially to my darling wife, Jianan Zhang. Thank you for your unconditional love and tremendous support. Without you, I couldn't go such far and explore the new world in my life. I LOVE YOU!

Abstract

This thesis presents the experimental and theoretical studies of the survival resonances in a dissipative atom-optics system, and their applications. We demonstrate this resonant phenomenon by using an alternative approach to the standard atom-optics δ-kicked rotor (AODKR), where we add spatially periodic dissipation or loss to each pulse. The system evolution is therefore non-unitary.

We first investigate the emergence of the survival resonances by exposing a cloud of laser-cooled Rubidium-85 atoms to standing-wave light pulses. The frequency of the light is tuned close to an open atomic transition. Scattering of the light from the standing wave leads the atoms to decay into a dark state that is far-off-resonance to both the standing-wave light and the subsequent detection light. Once the atoms go to the dark state, they are considered to be lost. The atom number is thereby *not* a conserved quantity. Consequently, a meaningful dynamic observable is the survival probability of the atoms. Varying the pulse interval reveals a series of resonant peaks at integer multiples of half the Talbot time. These peaks are deemed survival resonances and are a matter-wave interferometric phenomenon. The appearance of the peaks can be conceptually understood through the matter-wave Talbot-Lau effect. For a complete understanding, we build a model to simulate the system which captures the dynamics well.

In addition to acting as an optical mask that modulates the wave functions' amplitude, the still present optical dipole force of the standing wave imprints a phase pattern to the atomic wave functions. This gives rise to a micro-lensing effect that increases the peak survival dramatically. Using such an effect can help to enhance the incisiveness of the resonances, which might find applications in precision measurements.

The width of survival resonance peaks narrows faster than expected from the Fourier-limit when the pulse number is changed. The standard AODKR displays a similar sub-

Fourier behavior.

This thesis also demonstrates two applications of using survival resonances. The temporally pulsed spatially periodic dissipation is used for preparing well-defined initial conditions. Feeding back lost atoms gives a non-thermal atomic state that enhances subsequent survival resonance measurements. This can find its application in the state preparation in atom interferometry.

To show the feasibility of using survival resonances in an atom interferometer, we construct a proof-of-concept atomic gravimeter. With a vertically arranged standing-wave light beam, we perform an interferometric measurement of the gravitational acceleration g utilizing the survival resonances. Gravity removes the survival resonances, but they re-emerge when the standing wave co-moves with the free-falling atomic cloud. To study the performance of this technique and find a good parameter combination, we carry out a series of simulations and experiments. We measure g with a precision of 5 ppm using a drop distance of less than 1 mm. The sensitivity improves with the square of the drop time, which indicates we can reach a precision of the μ-Gal regime with a drop distance of 10 cm. The simple implementation makes this technique an attractive candidate for a low cost and compact atomic gravimeter.

Contents

List of Figures

We believe that there is romance in precision measurement and that ability to extend the absolute accuracy of measurement by one decimal point frequently demands as much ingenuity, perseverance and analytical competence as does the discovery of a new principle or effect in science.

——*Allen V. Astin*

Chapter 1

Introduction

1.1 Atom interferometers

From slash-and-burn to spacecraft, from knot note to supercomputer, from the stone tools to modern science and technology, human-kind have never stopped to explore the nature. The development of modern technologies demands an ever-increasing requirement on the precision of measurements. For instance, a farmer sows and harvests according to the seasons while navigation of a rocket relies on an atomic clock that typically provides precision at the level of 10^{-16} [1, 2]. Now, precision measurements have enabled technologies that have improved our daily life.

Among all the modern precision measurements, the atom interferometric technologies have never failed to attract attention and interests for their impressive accuracies [3–5]. The ability of such ingenious methodology allows for a deep understanding of the fundamental sciences as well as a wide range of practical applications, making it a fast developing field.

Before we rush to this fascinating topic, it is helpful to clarify some basic concepts:

1. What is an interferometer?

2. Why can we observe interferometric phenomena using atoms?

3. What is the difference between a light and an atom interferometer and why is the latter attractive?

Now, let's begin the journey.

Light interferometer

An interferometer is an instrument that utilizes the principle of superposition to generate an interference pattern by overlapping waves. Analyzing the interferometric pattern gives precise measurements.

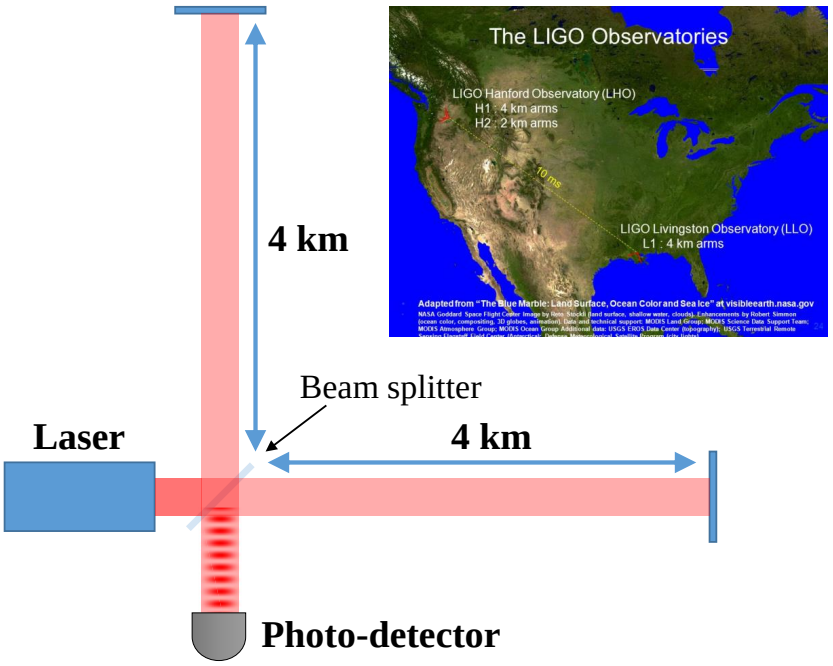

Figure 1.1: The advanced Laser Interferometer Gravitational-Wave Observatory (LIGO) [6].

Before we talk about the atom interferometer, it is helpful to know the working principle of its light counterpart. Let's consider the renowned light interferometer: the advanced "Laser Interferometer Gravitational-Wave Observatory" (LIGO). Figure 1.1 shows that

LIGO works by splitting a laser beam and sending it in two directions. After traveling for the same distance along 4 km long vacuum tubes, they are bounce back off mirrors and come back to re-combine. The light waves of these two laser beams are made to line up such that they cancel each other at the output and nothing will be detected at the photo-detector. But, if a gravitational wave distorts the space-time, the resulting change of the distance that each laser beam travels will cause the waves to no longer cancel. The photo-detector records the resulting signal. LIGO measures the relative distance with a sensitivity up to $\Delta L/L \sim 10^{-24}$ [7]. With such amazing precision, the LIGO group has detected several gravitational waves [8–12], which open a new era of cosmology. This shows that the centuries-old light interferometry technology is still at the forefront of precision measurements, highlighting the power of interferometric measurements.

The de Broglie hypothesis

Interference is a phenomenon that can only be obtained by using waves. Prior to the Ph.D. thesis "recherches sur la théorie des quanta" by Louis de Broglie in 1924 [13], interferometers was restricted to the light domain. In his thesis, de Broglie postulated the wave nature of electrons and suggested that interferences can be extended to all matter. The corresponding wavelength of a particle is given by:

$$\lambda_{\text{de Broglie}} = \frac{h}{p}, \tag{1.1}$$

where h is Planck's Constant and p is the momentum of the particle. This concept is known as the "wave-particle duality" that forms the cornerstone of quantum mechanics. Since atoms can be treated as waves, it is feasible to observe interferences using them.

Atom interferometers

Atom interferometers are conceptually analogous to their optical counterpart [3–5]. In both cases, an incident wave is split into two (or more) paths by a "beam splitter" and

travels for a while along different paths. They are redirected to overlap and recombine through a final beam splitter to produce an interference pattern. The fringes reveal information about effects that affect the waves' phase.

However, the realization of an atom interferometer is technically difficult. In the 1980s, the advent of laser-cooling technologies led to the birth of atomic sensing [14–17]. Since the first measurement using atom interferometers in the 1980s [18–20], it has evolved into a state of the art technique for precision measurements [21–24]. The ability to cool atoms to a quantum degenerate state in the late 90s provided an atomic source with a higher degree of coherence [25]. Nowadays atom interferometers use this to improve their performance [26–28].

Although the light interferometer techniques are very well developed and widely used, its atomic counterpart is still attractive. Atoms, unlike photons, carry mass that interacts with inertial forces such as gravity [29], which opens a new way of measuring inertial-related quantities [3]. This feature makes atomic interferometers an ideal tool in a range of practical and fundamental applications. For example, atom interferometers can measure gravity gradients [30–32], rotations [24, 33–35], the fine structure constant α [36–39] and the Newtonian gravitational constant G [40–42]. They also provide a tool for more sensitive test of the general relativity and have been proposed to gravitational wave detectors [27, 43–49].

1.2 Atomic gravimeter

One of the focuses of this thesis is measuring the local gravitational acceleration g by constructing a new atomic gravimeter [50, 51]. Similarly to the other types of gravimeters, atomic gravimeters are essentially an accelerometer that is specialized for measuring the downward acceleration on earth's surface. Conventionally, it displays its measurements in the unit of Gal (1 Gal = 1 cm/s^2), but the most commonly used unit is micro-Gal

($1\ \mu\text{Gal} = 10^{-8}\ \text{m/s}^2$).

Precision measurement of g has abundant applications. Geologists and earth scientists investigate the mass distribution beneath the ground through determining the local gravitational field accurately. Variations of the mass density can be extracted from the changes in the local gravitational acceleration. Gravity survey benefits mineral prospecting, seismology, and geodesy. Besides the practical applications, the strong interaction between atoms and the gravitational field also provides tools for measuring fundamental gravity-related quantities, i.e., the Newtonian gravitational constant G and makes it ideal for the tests of the weak equivalence principle [52, 53].

The first atomic gravimeter was demonstrated by Kasevish and Chu in 1991 [19]. With a Mach-Zehnder configuration, they used stimulated Raman transition as beam splitters and mirror to interfere a cloud of laser-cooled sodium atoms. They obtained a resolution to changes in g of 3×10^{-6} with a drop time of 20 ms. Using a fountain geometry and extending the overall drop time to 100 ms led the same group to reach a resolution of 3×10^{-8} in 1999 [20].

From then on, the work in atomic gravimeters took two separated paths. One is aiming for higher precision [21, 22, 27–29], while the other is for portable and commercial devices [54, 55]. The sensitivity of atom interferometry generally scales linearly with the space-time area enclosed by the interferometer [26, 56]. This led to the construction of the 10-meter drop tower that can increase the overall interrogation time to sec-regime [26, 57]. Accordingly, ultra-cold atoms are used to maintain the atoms in the interrogation zone [26, 58]. Besides extending the drop time, large-momentum-transfer beam splitters (LMT-BS) used for splitting atomic waves is also developed. For example, consecutive Bragg pulses are applied to transfer more momenta to the atoms, i.e., $24\hbar k_L$ [59] and $102\hbar k_L$ [26]. In our recent work, we showed a momentum separation up to $200\hbar k_L$ by kicking atoms with finite-duration standing-wave pulses [60]. Recently, alkaline-earth-metal atoms draw attention in the field due to their interesting characteristics [61]. For example, their

zero electronic angular momentum in the $^1S_0$ ground state makes them less sensitive to magnetic gradients. Additionally, the blue/near-UV range resonance transitions result in LMT-BS that corresponds to higher sensitivity.

In terms of commercial and compact atomic gravimeters, μ-Quans provides an absolute atomic gravimeter that performs measurements at the μ-Gal level [62, 63]. AOSense provided a compact atomic gravimeter to an aerospace customer in 2010 [64].

To further improve the performance and robustness, Hamilton and colleagues embedded the atom interferometer into an optical cavity [54, 65]. This leads the laser pulses to bounce back and forth inside the cavity, which results in an increase of the effective optical power and reducing of the imperfection of the wavefronts of the standing wave. Abend and co-workers proposed a new compact gravity-sensing device where an "atom chip" is used for creating ultra-cold atoms [55]. This design scales down the size of the system and reduces the preparation time of the atomic source. Consequently, it may pave the way for miniaturized and robust devices.

1.3 Atom-optics δ-kicked/killed rotor

Periodically driven one-dimensional (1-D) system play a central role in the studies of nonlinear dynamics, quantum chaos, and classical-quantum correspondence [66–71]. They exhibit a wide range of dynamical phenomena and are the simplest system for studying chaotic behavior. An important experimental platform is atom-optics δ-kicked rotor (AODKR) [66, 72, 73]. It consists of laser-cooled atoms receiving δ kicks at regular time intervals from a spatially periodic potential formed by a far-off-resonance standing wave of light. Its rich dynamics has allowed for clear experimental observations of a prodigious range of quantum effects. Particularly, experiments have shown that specific combinations of parameters and initial conditions can lead to directional transport in symmetric systems and hierarchies of quantum resonances and quantum accelerator modes (where

the transfer of momentum to atoms is unlimited) [66, 67, 74–79]. The δ kicks can act as a beam splitter and the AODKR is therefore capable of generating coherent superposition states with highly different momenta (more than $200\hbar k_L$) [60]. In 2002, Pascal and co-workers experimentally demonstrated the possibility of using AODKR to discriminate two frequencies, far below the Fourier limit [80]. This leads to the suggestion of using the sub-Fourier characteristics of such a quantum-chaotic system for high precision gravity measurements [81–84].

Unlike the well established Mach-Zehnder configuration [21, 22], the interferometers based on AODKR-design is a multi-path interferometer [52,85]. The δ kicks in the AODKR cause a spatially periodic phase modulation to the particles' wave function, which leads to the splitting of an initial momentum eigenstate into multiple diffraction orders. This thesis studies an alternation to the standard AODKR that is initially introduced by McDowall and co-workers in Ref. [86]. Instead of using a far-off-resonance standing-wave light, we tune the light frequency near to an open atomic transition. This leads atoms to scatter photons from the standing wave and spontaneously decay to a dark state. In addition to a phase modulation, the light pulses therefore also modulate the wave function's amplitude due to the spatially periodic loss. In terms of the classical rotor [87], this alternative approach gives each pulse a finite probability of "survival" or "death" of the particle that depends on its angle when the pulse is applied. We thereby name this system as the "δ-killed rotor" [50]. The system is non-unitary and a meaningful dynamic observable is the survival probability of the atoms after a pulse train.

By measuring the survival probability, the system displays a series of resonances for particular kicking periods, which are deemed "survival resonances" [50, 52]. These resonances are related to the quantum resonances that are well known from the standard AODKR. Nevertheless, the physical principles underpinning the resonance effects are distinct. The appearance of standard quantum resonances is based on phase pattern revivals due to the matter-wave Talbot effect and is highly sensitive to the initial momentum of

atoms [78]. When using an incoherent atomic source, these resonances are observed on a large background of non-resonant atoms [67]. Contrarily, survival resonances are based on the matter-wave Talbot-Lau effect, which allows for their clear observation using incoherent atomic waves effectively without a large unwanted background. This is because quantum resonances are only based on the external states, while the survival resonances are a result of the modulation of both internal and external degrees of freedom. The clear survival resonance peaks are thereby an attractive candidate for precision measurements.

1.4 Thesis Structure

This thesis will demonstrate the survival resonances and their applications in a sequence as follows:

Part I presents the theoretical description and the experimental realization of the system. Chapter 2 investigates the atomic motion in an optical standing wave. Chapter 3 analyzes the evolution of the atoms exposed to the light pulse sequence. Chapter 4 outlines the basic concepts of laser cooling and trapping techniques. Chapter 5 describes the experimental implementation of the 1-D atom-optics system that is driven by the temporally and spatially periodic dissipation.

Part II displays the experimental results of the survival resonances. Chapter 6 experimentally investigates the survival resonances in detail. In particular, it describes the appearance of these resonant peaks and studies the dynamical behavior of the system as a function of different parameters.

Part III demonstrates two applications based on the survival resonances. Chapter 7 exploits this resonant phenomenon for the preparation of a well-defined initial atomic state that can enhance the subsequent survival resonances. Chapter 8 presents a proof-of-principle atomic gravimeter utilizing the survival resonances.

Finally, Chapter 9 concludes the thesis and outlines the future work that may improve

the sensitivity of the measurements based on the survival resonances.

The work presented in this thesis is heavily based on the paper [50, 51].

1.5 Outcomes during my Ph.D.

The research described in this thesis has so far resulted in the following peer reviewed publications:

1. Shijie Chai, Mikkel F. Andersen, **Feedback enhanced survival resonances in a dissipative atom-optics system**, manuscript in preparation.

2. Shijie Chai, Julia Fekete, Mikkel F. Andersen, **Measuring the local gravitational field using survival resonances in a dissipatively driven atom-optics system**, conditionally accepted by Phys. Rev. A with minor corrections need to be done.

3. Shijie Chai, Julia Fekete, Peter McDowall, Simon Coop, Thue Lindballe, and Mikkel F. Andersen, **Survival resonances in an atom-optics system driven by temporally and spatially periodic dissipation**, Phys. Rev. **A 97**, 033616 (2018).

4. J. Fekete, S. Chai, S. A. Gardiner, and M. F. Andersen, **Resonant transfer of large momenta from finite-duration pulse sequences**, Phys. Rev. **A 95**, 033601 (2017).

Part I

Theory and Experiments

Chapter 2

Diffraction of atomic waves via a standing-wave light pulse

The atom-light interaction plays a crucial role in many atom-optics experiments. We can use laser light to coherently manipulate atoms and code information to the atomic wave functions. Laser light can construct reflective, refractive, and absorptive elements for matter-waves through the atom-light interaction [3–5]. These beautiful properties provide us with a kit to stop or accelerate, cool or heat, split or recombine, and probe atoms.

This chapter will give the theoretical description of how to use a short standing-wave light pulse as a matter-wave beam splitter. We begin by deriving the mathematical expressions for the electromagnetic field of the optical standing wave. Subsequently, the chapter will use two different models to explain the atom-light interaction. One of them is the simple two-level model that only contains one atomic transition, while the other is a more realistic four-level model that consists of the relevant transitions in ^{85}Rb atoms. Lastly, it will present the diffraction effect of the standing-wave pulse on the atomic waves.

2.1 The standing wave light field

In the analogy of the micro-fabricated diffraction gratings [88–90], an optical standing wave provides the possibility to construct a light-based grating due to its spatial periodicity [91, 92]. The section will give the mathematical scenario of the standing wave [93], particularly a static one and a moving one. The term "moving standing wave" refers to the position of nodes (or anti-nodes) that move spatially with time. Strictly speaking, it is therefore no longer a standing wave, but a moving wave.

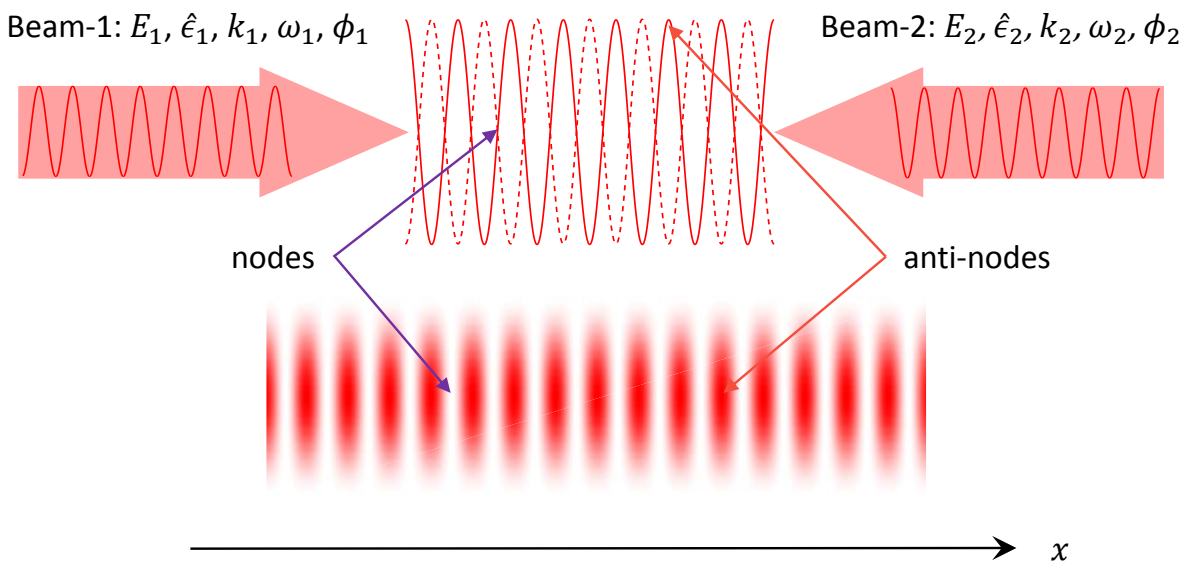

Figure 2.1: The formation of a standing-wave light field. Counter-propagating two laser beams 1 and 2 gives rise to a interferometric pattern. The intensity profile clearly shows nodes and anti-nodes of the standing wave. E the electric amplitude, $\hat{\boldsymbol{\epsilon}}$ the polarization unit vector, $\boldsymbol{k}$ the wave vector, ω the optical angular frequency and ϕ the phase.

The emergence of the standing-wave pattern is essentially a light-wave interferometric phenomenon. Laser beams utilized for creating standing waves are fundamentally transverse electromagnetic waves. For a well collimated monochromatic light beam, we can use

a plane wave to describe its profile along its propagation direction:

$$\boldsymbol{E}(\boldsymbol{r},t)=\frac{1}{2}\hat{\boldsymbol{\varepsilon}}Ee^{i(\boldsymbol{k}\cdot\boldsymbol{r}-\omega t)}+\text{c.c.}, \tag{2.1}$$

where E is the electric field amplitude, $\boldsymbol{r}$ the position, $\boldsymbol{k}$ the wave vector with the magnitude of $k=2\pi/\lambda$ (λ being the wavelength) and ω the angular frequency of the light. c.c. means the complex conjugate. $\hat{\boldsymbol{\varepsilon}}$ is the polarization unit vector that defines the orientation of the electric field. Note that in Eq. 2.1, we omitted the transverse profile of the beam, which is valid if the beam diameter is sufficiently large with respect to the atomic cloud. It will be discussed in Sec. 5.3.

Figure 2.1 displays a protocol for constructing a standing wave, where we counter-propagate two plane waves: 1 (forward) and 2 (backward). The superposition of these two waves has the form:

$$\begin{aligned}\boldsymbol{E}_{\text{SW}}(\boldsymbol{r},t)&=\boldsymbol{E}_1(\boldsymbol{r},t)+\boldsymbol{E}_2(\boldsymbol{r},t)\\&=\frac{1}{2}\hat{\boldsymbol{\varepsilon}}_1E_1e^{i(\boldsymbol{k_1}\cdot\boldsymbol{r}-\omega_1t)}+\frac{1}{2}\hat{\boldsymbol{\varepsilon}}_2E_2e^{i(\boldsymbol{k_2}\cdot\boldsymbol{r}-\omega_2t)}+\text{c.c.},\end{aligned} \tag{2.2}$$

where the subscript "SW" refers to standing wave. Equation 2.2 gives the general expression of overlapping any two plane waves.

In the experiment, we restrict the laser beam 1 and 2 to be counter-propagating along the x-axis ($k_2=-k_1$) and to have a lin $\parallel$ lin polarization configuration ($\hat{\boldsymbol{\varepsilon}}_1=\hat{\boldsymbol{\varepsilon}}_2=\hat{\boldsymbol{\varepsilon}}$). Equation 2.2 then becomes:

$$\begin{aligned}\boldsymbol{E}_{\text{SW}}(x,t)&=\boldsymbol{E}_1(x,t)+\boldsymbol{E}_2(x,t)\\&=\frac{1}{2}\hat{\boldsymbol{\varepsilon}}E_1e^{i(k_1x-\omega_1t)}+\frac{1}{2}\hat{\boldsymbol{\varepsilon}}E_2e^{i(-k_1x-\omega_2t)}+\text{c.c.}.\end{aligned} \tag{2.3}$$

Starting from Eq. 2.3, this section demonstrates two cases of the standing wave as follows:

CASE-I: a static standing wave whose pattern does not move spatially with time. We typically obtain a stationary standing wave by retro-reflecting a laser beam with a mirror. The retro-beam therefore shares the same frequency ($\omega_2=\omega_1=\omega_0$). The electric field of

the stationary standing wave is then described as:

$$\begin{aligned}\boldsymbol{E}_{\mathrm{SW}}(x,t) &= \boldsymbol{E}_1(x,t) + \boldsymbol{E}_2(x,t) \\ &= \frac{1}{2}\hat{\boldsymbol{\varepsilon}}E_1 e^{i(k_1 x-\omega_0 t)} + \frac{1}{2}\hat{\boldsymbol{\varepsilon}}E_2 e^{i(-k_1 x-\omega_0 t)} + \text{c.c.}. \\ &= \hat{\boldsymbol{\varepsilon}}E_2\cos(k_1 x)\, e^{-i\omega_0 t} + \frac{1}{2}\hat{\boldsymbol{\varepsilon}}\,(E_1 - E_2)\, e^{i(k_1 x-\omega_0 t)} + \text{c.c.}.\end{aligned} \tag{2.4}$$

When $E_2 = E_1$, Eq. 2.4 becomes:

$$\begin{aligned}\boldsymbol{E}_{\mathrm{SW}}(x,t) &= \hat{\boldsymbol{\varepsilon}}E_1\cos(k_1 x)\left(e^{i\omega_0 t} + e^{-i\omega_0 t}\right) \\ &= 2\hat{\boldsymbol{\varepsilon}}E_1\cos(k_1 x)\cos(\omega_0 t)\,.\end{aligned} \tag{2.5}$$

In this situation, the nodes [where $\cos(k_1 x) = 0$] are completely dark, which allows for the best contrast.

CASE-II: a moving standing wave whose pattern accelerates at a constant acceleration a. When the frequency difference between the two counter-propagating beams is linearly chirped, the interferometric pattern moves with a constant acceleration. For convenience, we initiate the two frequencies to be ω_0 and chirp them at the same rate $\dot{\omega}$ but with opposite sign:

$$\begin{aligned}\omega_1 &= \omega_0 - \dot{\omega}t, \\ \text{and } \omega_2 &= \omega_0 + \dot{\omega}t,\end{aligned} \tag{2.6}$$

which give the time-dependent phase for each beam:

$$\begin{aligned}\phi_1 &= \omega_0 t - \frac{1}{2}\dot{\omega}t^2, \\ \text{and } \phi_2 &= \omega_0 t + \frac{1}{2}\dot{\omega}t^2.\end{aligned} \tag{2.7}$$

Assuming $E_2 = E_1$ and substituting ϕ_1 and ϕ_2 from Eq. 2.7 into Eq. 2.3 give:

$$\begin{aligned}\boldsymbol{E}_{\mathrm{SW}}(x,t) &= \boldsymbol{E}_1(x,t) + \boldsymbol{E}_2(x,t) \\ &= \frac{1}{2}\hat{\boldsymbol{\varepsilon}}E_1 e^{i\left(k_1 x-\omega_0 t+\frac{1}{2}\dot{\omega}t^2\right)} + \frac{1}{2}\hat{\boldsymbol{\varepsilon}}E_1 e^{i\left(-k_1 x-\omega_0 t-\frac{1}{2}\dot{\omega}t^2\right)} + \text{c.c.}. \\ &= 2\hat{\boldsymbol{\varepsilon}}E_1\cos\left(k_1 x + \frac{1}{2}\dot{\omega}t^2\right)\cos(\omega_0 t) \\ &= 2\hat{\boldsymbol{\varepsilon}}E_1\cos\left[k_1\left(x + \frac{1}{2}\frac{\dot{\omega}}{k_1}t^2\right)\right]\cos(\omega_0 t)\,.\end{aligned} \tag{2.8}$$

Equation. 2.8 shows the motion of the interference pattern explicitly depends on time t and moves at a constant acceleration $a = \dot{\omega}/k_1$. When $\dot{\omega} = 0$, $\boldsymbol{E}_{\mathrm{SW}}(x,t)$ in Eq. 2.8 becomes the stationary standing wave (see in Eq. 2.5).

2.2 The atomic system

We now study the evolution of the atomic wave function when it is exposed a brief standing-wave light pulse. Two atomic models are used to explain the dynamics of the system.

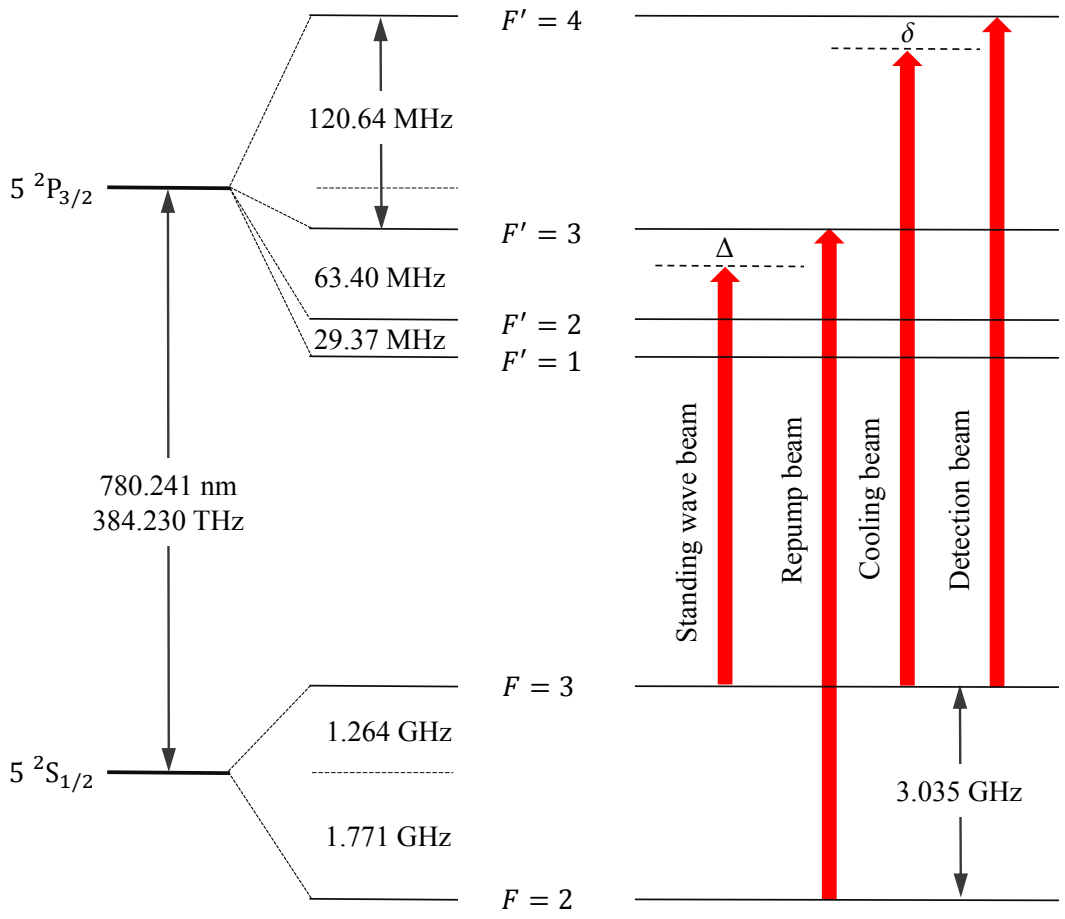

Figure 2.2: ^{85}Rb atom D2-line transition hyperfine structure [94] (not to scale), with red arrows showing optical frequencies for the typical lasers in the experiments. The cooling laser frequency is tuned below the F = 3 to F$'$ = 4 closed atomic transition, with δ within $2 \sim 5$ natural line width Γ. The repump light is locked on resonance of the F = 2 to F$'$ = 3 atomic transition. The detection beam is on resonance of the closed atomic transition from F = 3 to F$'$ = 4. The standing-wave light is tuned near to one of the open atomic transitions with its detuning Δ being within two natural line width.

Figure 2.2 shows the D2-line hyperfine structure of the ^{85}Rb atom [94]. There are two hyperfine ground states F = 2 and F = 3 and four excited hyperfine states F$'$ = 1, F$'$ = 2, F$'$ = 3 and F$'$ = 4.

Figure 2.2 also displays the optical frequencies for the main laser light used for manipulating atoms. This chapter will focus on the standing-wave light rather than the cooling, repump and detection light which we will describe in detail in Chapter 5. Figure 2.2 shows one of the possible standing-wave light frequencies, which is near-resonance to the open atomic transition from $F = 3$ to $F' = 3$ with a finite detuning Δ. When the standing wave light is tuned to other transitions in the following experiments, we will point out the parameter correspondingly.

2.2.1 The two-level model

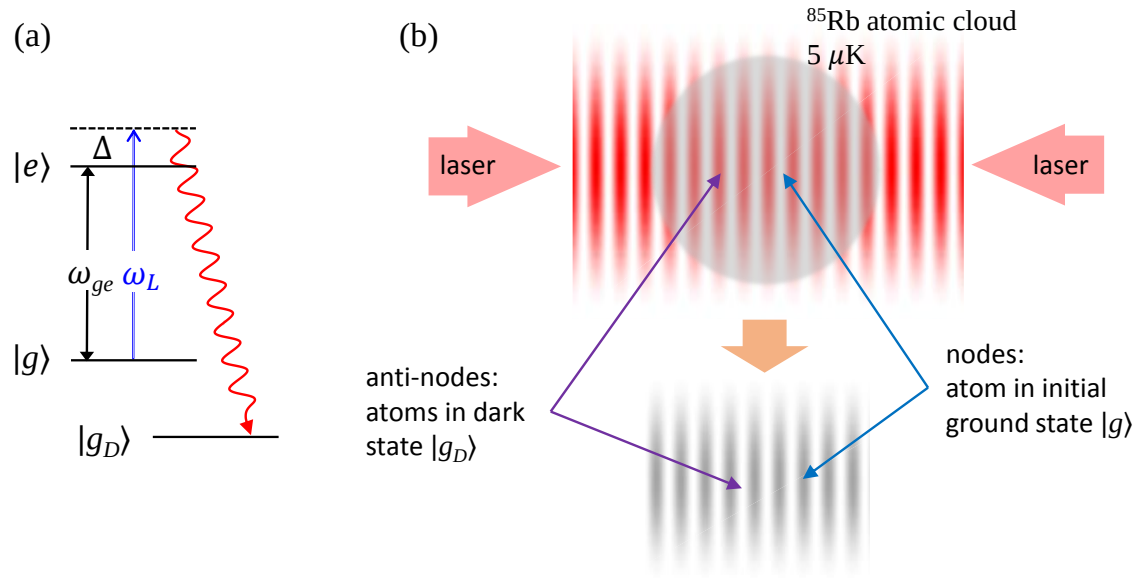

Figure 2.3: A three-level atom interacts with a near-resonance standing-wave light field (not to scale).

(a) Simplified energy level diagram (not to the scale). The blue arrow represents the absorption of a photon from the standing-wave beam whose frequency is tuned to $\omega_{\mathrm{L}} = \omega_{\mathrm{ge}} + \Delta$, where ω_{ge} denotes the on-resonance atomic transition frequency and Δ is the laser detuning. The red wavy line shows the spontaneous emission to an internal atomic state $|g_{\mathrm{D}}\rangle$ that is a dark state, where we consider the atoms to be lost from the system [50, 52, 91, 92]. In this figure, we omit the spontaneously decay back to its initial ground state $|g\rangle$.

(b) Schematic diagram for producing an atomic absorption grating with a near-resonance standing-wave beam. The standing-wave light acts as an absorption grating that depletes atoms from their initial ground state $|g\rangle$ to the dark state $|g_{\mathrm{D}}\rangle$ everywhere except in the vicinity of the nodes. Grey circle and stripes show the atomic density distribution of atoms in $|g\rangle$.

Generally, the atom has an infinite number of allowed transitions. This was known even prior to the development of quantum mechanics, where people had identified Balmer series

of the hydrogen atom [95,96]. Each of the spectral lines is associated with a specific atomic transition between two energy eigenstates. Nevertheless, for most situations dealing with the atom-light interaction, it is sufficient to only take the closest transition into account, since the other transitions are off-resonance to the light field and the interaction energy is weak. We therefore use a two-level model to describe the system in this part.

Figure. 2.3(a) shows a simplified level diagram of ^{85}Rb atoms, whose ground state ($|g\rangle$) and excited state ($|e\rangle$) are coupled through a near-resonant standing wave light field. For the light frequency near to the open atomic transition from F = 3 to F$'$ = 3 (see Fig. 2.2), $|g\rangle$ is the F = 3 ground state and $|e\rangle$ is the F$'$=3 excited hyperfine state. The F = 2 ground state is ∼3 GHz off-resonance to the standing-wave light, which makes it to be a non-interacting state and we deem the "dark state" ($|g_D\rangle$). We consider the atoms to be lost once they decay to the this state. The three level atom in Fig. 2.3 can therefore be treated as a two-level system that is coupled to the environment [50, 97].

When exposing the atoms to a standing wave light field shown in Fig. 2.3(b), they will scatter photons from the standing wave and go to the dark state at the high intensity region (away from the nodes). For those atoms in the vicinity of the nodes, they see no light and therefore remain in the initial state. The standing-wave beam thereby effectively acts as an absorption grating, since it removes the atoms periodically along the standing wave's coordinate [52, 91, 92]. Besides the amplitude modulation, the finite detuning of the standing wave leads to the formation of a spatially periodic dipole potential that will imprint a phase pattern on the atomic wave function [50, 51]. This results in a phase modulation to the atoms, which is similar to the one used in the standard AODKR [72,73]. The standing-wave pulse thereby acts as a hybrid of amplitude and phase gratings [50,51].

Dynamics in the standing wave

During the experiment, we expose the atoms to a series of standing-wave light pulses. In this chapter, we will focus on the dynamics of the system during the pulse. The calculation

closely follows Peter's thesis [86].

The Hamiltonian of a two-level atom interacting with a near-resonant standing wave is given by [50–52, 86, 97]:

$$H = \frac{p^2}{2M} + \hbar\omega_g|g\rangle\langle g| + \left(\hbar\omega_e - \frac{i\hbar\Gamma}{2}\right)|e\rangle\langle e| + V_I(x,t), \tag{2.9}$$

where we have omitted the atom-atom interaction, which is valid for a dilute sample. In Eq. 2.9, p is the atomic momentum and M is the mass of the atom. $\hbar\omega_g$ and $\hbar\omega_e$ are the atomic energies for the ground state $|g\rangle$ and excited state $|e\rangle$. The imaginary term $-i\hbar\Gamma/2$ accounts for the relaxation of the excited state to the dark state $|g_{\mathrm{D}}\rangle$. We ignore the spontaneously decay back to its initial ground state $|g\rangle$, which results in an incoherent background. The atom-light interaction energy $V_I(x,t)$ is described by using the dipole approximation $V_I(x,t) = -\boldsymbol{d}\cdot\boldsymbol{E}_{\mathrm{SW}}$, where $\boldsymbol{d}$ is the atomic dipole moment and $\boldsymbol{E}_{\mathrm{SW}}$ is the electric field of the standing-wave light [98]. For simplicity, using $\boldsymbol{E}_{\mathrm{SW}} = 2\hat{\boldsymbol{\varepsilon}}E_1\cos(k_Lx)\cos(\omega_0t)$ for a perfectly balanced standing wave in Eq. 2.5, H becomes:

$$\begin{aligned} H =& \frac{p^2}{2M} + \hbar\omega_g|g\rangle\langle g| + \left(\hbar\omega_e - \frac{i\hbar\Gamma}{2}\right)|e\rangle\langle e| \\ &+ \hbar\Omega\left(|e\rangle\langle g| + |g\rangle\langle e|\right)\cos(k_Lx)\cos(\omega_Lt), \end{aligned} \tag{2.10}$$

where ω_L is the light frequency, and Ω is the on-resonance Rabi frequency at the anti-nodes:

$$\Omega = -\frac{\langle g|\hat{\boldsymbol{\varepsilon}}\cdot\boldsymbol{d}|e\rangle 2E_1}{\hbar}. \tag{2.11}$$

The term $\frac{p^2}{2M}$ in H of Eqs. 2.9 and 2.10 is the kinetic energy that accounts for the atomic motion along the standing wave prorogation axis. When it is much less than the atom-light interaction energy $V_I(x,t)$, we can ignore the atomic motion during the light pulse, which is known as the Raman-Nath approximation [99]. When the system is in the Raman-Nath regime, the Hamiltonian H in Eq. 2.10 is given by:

$$\begin{aligned} H =& \hbar\omega_g|g\rangle\langle g| + \left(\hbar\omega_e - \frac{i\hbar\Gamma}{2}\right)|e\rangle\langle e| \\ &+ \hbar\Omega\left(|e\rangle\langle g| + |g\rangle\langle e|\right)\cos(k_Lx)\cos(\omega_Lt), \end{aligned} \tag{2.12}$$

which governs the dynamics of the system during the light pulse.

Evolution of the system

The time evolution of the two-level atom in the standing-wave light field can be described by the Schrödinger equation [86, 95, 97]:

$$i\hbar\frac{\partial\psi}{\partial t} = H\psi, \tag{2.13}$$

where ψ is the atomic state that is a function of time t and position x. We can use the basis formed by the two internal states $|g\rangle$ and $|e\rangle$ of the atom to describe ψ:

$$\psi(x,t) = a_g(x,t)|g\rangle + a_e(x,t)|e\rangle, \tag{2.14}$$

where $a_g(x,t)$ and $a_e(x,t)$ denote the probability amplitudes of the ground state $|g\rangle$ and excited state $|e\rangle$ for a given time t at position x.

For convenience, we now use the matrix formalism to calculate the evolution. The atomic state $\psi(x,t)$ of Eq. 2.14 and the Hamiltonian H of Eq. 2.12 can be represented by:

$$|\psi,t\rangle \doteq \begin{bmatrix} a_g(x,t) \\ a_e(x,t) \end{bmatrix}, \tag{2.15}$$

and

$$H \doteq \begin{bmatrix} \hbar\omega_g & \hbar\Omega\cos(k_L x)\cos(\omega_L t) \\ \hbar\Omega^*\cos(k_L x)\cos(\omega_L t) & \hbar\omega_e - \frac{i\hbar\Gamma}{2} \end{bmatrix}. \tag{2.16}$$

To further simplify H, we chose the ground state $|g\rangle$ energy to be zero and use $\hbar\omega_{ge}$ to represent the atomic energy for the excited state $|e\rangle$. Thus, H becomes:

$$H \doteq \begin{bmatrix} 0 & \hbar\Omega\cos(k_L x)\cos(\omega_L t) \\ \hbar\Omega^*\cos(k_L x)\cos(\omega_L t) & \hbar\omega_{ge} - \frac{i\hbar\Gamma}{2} \end{bmatrix}, \tag{2.17}$$

where $\omega_{ge} = \omega_e - \omega_g$ denotes the on-resonance angular frequency of the atomic transition from $|g\rangle$ to $|e\rangle$.

Rotating wave approximation

For brief pulses (Raman-Nath regime), time-dependent Hamiltonian in Eq. 2.17 fully describes the system dynamics. However, it is preferential to simplify the calculation by

using rotating wave approximation to remove the fast oscillating time-dependent term $\cos(\omega_L t)$. In this part, We will outline the rotating wave approximation in detail.

To simplify the Hamiltonian in Eq. 2.17, we gauge-transfer the system to a rotating frame using the unitary operator $\mathcal{U} = e^{-i\omega_L t}$, whose matrix form is:

$$\mathcal{U} = \begin{bmatrix} 1 & 0 \\ 0 & e^{-i\omega_L t} \end{bmatrix}, \tag{2.18}$$

The atomic state $|\psi, t\rangle$ in Eq. 2.15 subsequently becomes $|\widetilde{\psi}, t\rangle = \mathcal{U}^\dagger |\psi, t\rangle$:

$$|\widetilde{\psi}, t\rangle \doteq \begin{bmatrix} 1 & 0 \\ 0 & e^{i\omega_L t} \end{bmatrix} \begin{bmatrix} a_g(x,t) \\ a_e(x,t) \end{bmatrix} = \begin{bmatrix} a_g(x,t) \\ a_e(x,t)\mathrm{e}^{i\omega_L t} \end{bmatrix}. \tag{2.19}$$

Rewriting $|\widetilde{\psi}, t\rangle$ in Eq. 2.19 using $c_g(x,t) = a_g(x,t)$ and $c_e(x,t) = a_e(x,t)\mathrm{e}^{i\omega_L t}$:

$$|\widetilde{\psi}, t\rangle \doteq \begin{bmatrix} c_g(x,t) \\ c_e(x,t) \end{bmatrix}. \tag{2.20}$$

Taking the time derivative of the atomic state $|\widetilde{\psi}, t\rangle$ and using the Schrödinger equation in Eq. 2.13 yields:

$$\begin{aligned} i\hbar \frac{\partial(\mathcal{U}^\dagger |\psi, t\rangle)}{\partial t} &= \mathcal{U}^\dagger i\hbar \frac{\partial |\psi, t\rangle}{\partial t} + i\hbar \frac{\partial \mathcal{U}^\dagger}{\partial t} |\psi, t\rangle \\ &= \mathcal{U}^\dagger H |\psi, t\rangle + i\hbar \frac{\partial \mathcal{U}^\dagger}{\partial t} |\psi, t\rangle \\ &= \mathcal{U}^\dagger H \mathcal{U} (\mathcal{U}^\dagger |\psi, t\rangle) + i\hbar \frac{\partial \mathcal{U}^\dagger}{\partial t} \mathcal{U} (\mathcal{U}^\dagger |\psi, t\rangle). \end{aligned} \tag{2.21}$$

The atomic state $|\widetilde{\psi}, t\rangle$ is then governed by the gauge-transformed Hamiltonian $\widetilde{H} = \mathcal{U}^\dagger H \mathcal{U} + i\hbar \frac{d\mathcal{U}^\dagger}{dt}\mathcal{U}$:

$$\begin{aligned}
\widetilde{H} \doteq & \begin{bmatrix} 1 & 0 \\ 0 & e^{i\omega_L t} \end{bmatrix} \begin{bmatrix} 0 & \hbar\Omega\cos(k_L x)\cos(\omega_L t) \\ \hbar\Omega^*\cos(k_L x)\cos(\omega_L t) & \hbar\omega_{ge} - \frac{i\hbar\Gamma}{2} \end{bmatrix} \begin{bmatrix} 1 & 0 \\ 0 & e^{-i\omega_L t} \end{bmatrix} \\
& + i\hbar\frac{\partial}{\partial t}\left(\begin{bmatrix} 1 & 0 \\ 0 & e^{i\omega_L t} \end{bmatrix} \right) \begin{bmatrix} 1 & 0 \\ 0 & e^{-i\omega_L t} \end{bmatrix} \\
= & \begin{bmatrix} 0 & \hbar\Omega\cos(k_L x)\cos(\omega_L t)e^{(-i\omega_L t)} \\ \hbar\Omega^*\cos(k_L x)\cos(\omega_L t)e^{(i\omega_L t)} & -\left(\hbar\Delta + \frac{i\hbar\Gamma}{2}\right) \end{bmatrix} \\
= & \begin{bmatrix} 0 & \hbar\Omega\cos(k_L x)\left(\frac{e^{(i\omega_L t)}+e^{(-i\omega_L t)}}{2}\right)e^{(-i\omega_L t)} \\ \hbar\Omega^*\cos(k_L x)\left(\frac{e^{(i\omega_L t)}+e^{(-i\omega_L t)}}{2}\right)e^{(i\omega_L t)} & -\left(\hbar\Delta + \frac{i\hbar\Gamma}{2}\right) \end{bmatrix} \\
= & \begin{bmatrix} 0 & \frac{\hbar\Omega}{2}\cos(k_L x) \\ \frac{\hbar\Omega^*}{2}\cos(k_L x) & -\left(\hbar\Delta + \frac{i\hbar\Gamma}{2}\right) \end{bmatrix} + \begin{bmatrix} 0 & \frac{\hbar\Omega}{2}\cos(k_L x)e^{(-2i\omega_L t)} \\ \frac{\hbar\Omega^*}{2}\cos(k_L x)e^{(2i\omega_L t)} & 0 \end{bmatrix},
\end{aligned} \tag{2.22}$$

where $\Delta = \omega_{ge} - \omega_L$ is the light detuning of the standing wave to the atomic transition. The effect given by the fast oscillating term with a frequency of $2\omega_L$ will average to zero. We can therefore throw it away, which is know as the rotating wave approximation. $\widetilde{H}$ is therefore given by:

$$\widetilde{H} \doteq \begin{bmatrix} 0 & \frac{\hbar\Omega}{2}\cos(k_L x) \\ \frac{\hbar\Omega^*}{2}\cos(k_L x) & -\left(\hbar\Delta + \frac{i\hbar\Gamma}{2}\right) \end{bmatrix}. \tag{2.23}$$

The Hamiltonian $\widetilde{H}$ is now time-independent, which will populate the atoms to a superposition state of the ground and excited states. The survival probability after the light pulse (the experimental output) is given by $\int |c_g(x,t)|^2 dx$.

Grating operator

We now investigate the evolution of the system governed by Hamiltonian $\widetilde{H}$ in Eq. 2.23, where we can define a "grating operator" that gives the effect of the standing wave pulse

on the atoms. We will outline the calculation in detail, which is firstly derived in Peter's thesis [86].

We use the dressed state picture to investigate the dynamics of a two-level atom coupled to a near-resonance standing-wave light field. In the dressed state picture, coupling the two levels through the external field results in two new eigenstates that are called dressed states [100]. They are the superpositions of the two uncoupled bare states. Once the dressed states and their eigenvalues are found, it is easy to compute the dynamics of the system.

Hamiltonian $\widetilde{H}$ in Eq. 2.23 has two spatially varying eigenvalues:

$$\lambda_{1,2} = -\frac{1}{2}\left(\hbar\Delta + \frac{i\hbar\Gamma}{2}\right) \mp \frac{1}{2}\sqrt{\left(\hbar\Delta + \frac{i\hbar\Gamma}{2}\right)^2 + (\hbar\Omega)^2\cos^2(k_L x)}, \tag{2.24}$$

and two corresponding eigenvectors:

$$\begin{aligned} |1\rangle &\doteq \begin{bmatrix} \frac{\hbar\Omega\cos(k_L x)}{2\lambda_1} \\ 1 \end{bmatrix} = \begin{bmatrix} \frac{V}{\lambda_1} \\ 1 \end{bmatrix}, \text{ and} \\ |2\rangle &\doteq \begin{bmatrix} 1 \\ \frac{2\lambda_2}{\hbar\Omega\cos(k_L x)} \end{bmatrix} = \begin{bmatrix} 1 \\ \frac{\lambda_2}{V} \end{bmatrix}, \end{aligned} \tag{2.25}$$

where $V = \hbar\Omega\cos(k_L x)/2$ is used to simplify the expressions. The new eigenstates in Eq. 2.25 are the dressed states of the atom, which can be used to calculate the time evolution of the atomic wave function $|\widetilde{\psi}, t\rangle$ in Eq. 2.20. Using $\lambda_1, \lambda_2, |1\rangle$ and $|2\rangle$ in Eqs. 2.24 and 2.25, one can get:

$$\begin{aligned} \begin{bmatrix} c_g(x,t) \\ c_e(x,t) \end{bmatrix} &= \frac{1}{1-\frac{\lambda_2}{\lambda_1}} \begin{bmatrix} 1 & \frac{V}{\lambda_1} \\ \frac{\lambda_2}{V} & 1 \end{bmatrix} \begin{bmatrix} \mathrm{e}^{-\frac{i}{\hbar}\lambda_2 t} & 0 \\ 0 & \mathrm{e}^{-\frac{i}{\hbar}\lambda_1 t} \end{bmatrix} \begin{bmatrix} 1 & -\frac{V}{\lambda_1} \\ -\frac{\lambda_2}{V} & 1 \end{bmatrix} \begin{bmatrix} c_g(x,0) \\ c_e(x,0) \end{bmatrix} \\ &= \frac{1}{1-\frac{\lambda_2}{\lambda_1}} \begin{bmatrix} \mathrm{e}^{-\frac{i}{\hbar}\lambda_2 t} - \frac{\lambda_2}{\lambda_1}\mathrm{e}^{-\frac{i}{\hbar}\lambda_1 t} & -\frac{V}{\lambda_1}\mathrm{e}^{-\frac{i}{\hbar}\lambda_2 t} + \frac{V}{\lambda_1}\mathrm{e}^{-\frac{i}{\hbar}\lambda_1 t} \\ \frac{\lambda_2}{V}\mathrm{e}^{-\frac{i}{\hbar}\lambda_2 t} - \frac{\lambda_2}{V}\mathrm{e}^{-\frac{i}{\hbar}\lambda_1 t} & -\frac{\lambda_2}{\lambda_1}\mathrm{e}^{-\frac{i}{\hbar}\lambda_2 t} + \mathrm{e}^{-\frac{i}{\hbar}\lambda_1 t} \end{bmatrix} \begin{bmatrix} c_g(x,0) \\ c_e(x,0) \end{bmatrix}. \end{aligned} \tag{2.26}$$

Equation 2.26 gives the time evolution of the wave function when exposing the atom to a short standing-wave light pulse. From Eq. 2.26, we can obtain the general expression

for $c_g(x,t)$ and $c_e(x,t)$ at any position x and time t, when the Raman-Nath condition is valid. We assume that the atoms are all initially populated in the ground state $|g\rangle$ and leave $c_e(x,0) = 0$. The probability amplitude of finding atom in $|g\rangle$ after a pulse is then given by:

$$c_g(x,\tau) = \frac{1}{1-\frac{\lambda_2}{\lambda_1}}\left(\mathrm{e}^{-\frac{i}{\hbar}\lambda_2\tau} - \frac{\lambda_2}{\lambda_1}\mathrm{e}^{-\frac{i}{\hbar}\lambda_1\tau}\right) c_g(x,0). \tag{2.27}$$

Additionally, we already assumed that the atoms pumped to the excited state $|e\rangle$ will spontaneously decay into the dark state $|g_D\rangle$ after each pulse. $c_e(x,t)$ is therefore zero before each of the subsequent pulses. We can thereby define a "grating operator" G that describe the effect of the standing-wave light pulse on the wave function of atoms remaining in $|g\rangle$:

$$G(x,\tau) = \frac{1}{1-\frac{\lambda_2}{\lambda_1}}\left(\mathrm{e}^{-\frac{i}{\hbar}\lambda_2\tau} - \frac{\lambda_2}{\lambda_1}\mathrm{e}^{-\frac{i}{\hbar}\lambda_1\tau}\right). \tag{2.28}$$

G is the analytical solution of Eq. 2.26 that describes the effect of the standing wave light pulse on the wave function of the atoms remaining in their initial ground state. It is a function of position x and pulse duration τ but not the total time t. This means we only need to compute G once during the entire experimental sequence, and can apply it to the atomic wave function for the following pulses. Since the two eigenvalues $\lambda_{1,2}$ are complex values, G also has real and complex components, which means it contains both the phase and amplitude modulations [50].

2.2.2 The four-level model

The above two-level model is valid if only one excited hyperfine state is coupled to the ground state by the light. However, in a real atom, there are usually more than one possible transition. Figure 2.2 shows the D-2 line of the ^{85}Rb atom having four excited hyperfine states. The detuning Δ is not neglectable compared to the hyperfine splitting of the excited states. When exposing the atoms to the standing-wave light, more than one excited hyperfine states will contribute to the dynamics. A two-level model may thereby

fail to capture some aspects. Consequently, this sub-section will extend the two-level model to a four-level model that accounts for more possible atomic transitions on the D2-line.

As shown in Fig. 2.2, the F = 3 ground state is the initial ground state denoted $|3\rangle$, and the F = 2 ground state is the dark state $|g_{\mathrm{D}}\rangle$. The standing-wave light couples $|3\rangle$ to three excited states $|e\rangle$ that are $\mathrm{F}' = 2, 3$ and 4 states. Again, invoking the Raman-Nath approximation and using the electric field $\boldsymbol{E}_{\mathrm{SW}}$ given in Eq. 2.5, the Hamiltonian H for the four-level model is an extension of its two-level counterpart in Eq. 2.12:

$$\begin{aligned} H =& \hbar\omega_3|3\rangle\langle 3| + \sum_{e=2}^{4}\left(\hbar\omega_e - \frac{i\hbar\Gamma}{2}\right)|e\rangle\langle e| \\ &+ \sum_{e=2}^{4}\hbar\Omega_{3e}\left(|e\rangle\langle 3| + |3\rangle\langle e|\right)\cos\left(k_L x\right)\cos\left(\omega_L t\right), \end{aligned} \tag{2.29}$$

where Ω_{3e} is the on-resonance Rabi frequency for each atomic transition at the anti-nodes of the standing wave. Following the same procedure used for the two-level model (rotating-wave approximation), $\widetilde{H}$ takes the form:

$$\widetilde{H} \doteq \begin{bmatrix} 0 & \frac{\hbar\Omega_{32'}}{2}\cos(k_L x) & \frac{\hbar\Omega_{33'}}{2}\cos(k_L x) & \frac{\hbar\Omega_{34'}}{2}\cos(k_L x) \\ \frac{\hbar\Omega^*_{32'}}{2}\cos(k_L x) & -\left(\hbar\Delta_{32'} + \frac{i\hbar\Gamma}{2}\right) & 0 & 0 \\ \frac{\hbar\Omega^*_{33'}}{2}\cos(k_L x) & 0 & -\left(\hbar\Delta_{33'} + \frac{i\hbar\Gamma}{2}\right) & 0 \\ \frac{\hbar\Omega^*_{34'}}{2}\cos(k_L x) & 0 & 0 & -\left(\hbar\Delta_{34'} + \frac{i\hbar\Gamma}{2}\right) \end{bmatrix}, \tag{2.30}$$

where Δ_{3e} denotes the standing-wave detuning of the corresponding atomic transition. The atomic state $|\widetilde{\psi}, t\rangle$ also extends to a four-component column vector:

$$|\widetilde{\psi}, t\rangle \doteq \begin{bmatrix} c_3(x,t) \\ c_{2'}(x,t) \\ c_{3'}(x,t) \\ c_{4'}(x,t) \end{bmatrix}. \tag{2.31}$$

Using $\widetilde{H}$ in Eq. 2.30 will leave the atoms in a superposition of the different internal states. However, we are only interested in the atoms remaining in their initial ground

state. We can thereby again define a grating operator G that describes the effect of the standing wave on the wave function remaining in F = 3 state:

$$G(x,\tau) = \langle 3| \exp\left(-\frac{i}{\hbar}\tilde{H}\tau\right)|3\rangle. \tag{2.32}$$

The analytical expression for $G(x,\tau)$ can be fairly complex for the four-level atom. We thereby use the built-in MATLAB function "eig" to solve it numerically (see Appendix A).

2.3 Diffraction of atomic waves

This section will study the diffraction effect of the standing-wave light pulse on atoms. We will use two pictures to address this phenomenon: one is the photon picture, and the other is the semi-classical picture.

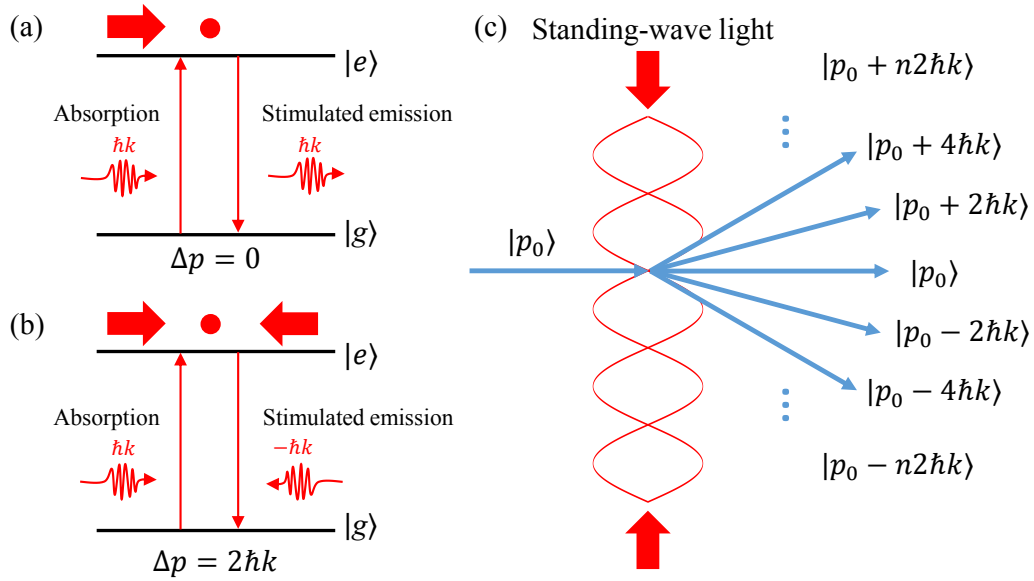

Figure 2.4: Matter-wave diffraction through a short standing-wave light pulse [3]. (a) An atom experiences no net momentum transfer in a traveling light wave since it absorbs and stimulatedly emits a photon to the same direction. (b) An atom experiences a $2\hbar k_L$ momentum transfer in a standing-wave light wave. (c) The standing-wave light pulse acts as a grating that split the atomic wave function into different diffraction orders that are differing by $2\hbar k_L$ due to the two-photon process.

The diffraction effect builds on the momentum transfer from the light to the atoms. To understand this, we consider the interaction between a two-level atom and a resonant photon.

As illustrated in Fig. 2.4(a), the absorption of a photon from a traveling wave results in a momentum transfer to the atom. The momentum change of the atom has the unit of $\hbar k_L$, known as photon recoil. The atom subsequently undergoes a stimulated emission to release a photon to the traveling wave. Since the emitted photon has the same direction of the original photon, the net momentum transfer is 0. However, if exposing the atoms to a standing wave, it can be stimulated to emit the photon to the direction opposite to the absorbed photon. This results in a net momentum transfer of $2\hbar k_L$, shown in Fig. 2.4(b). After a number of the absorption-stimulated emission processes, the atomic waves can scatter into a series of diffraction orders that are separated by $2\hbar k_L$ [see Fig. 2.4(c)].

As illustrated in Fig. 2.4(c), since the standing-wave light pulse can coherently split the incoming plane wave into a number of diffraction orders, we can thereby use it as a matter-wave beam splitter.

The following sub-sections utilize the semi-classical picture to quantitatively study how to use the standing wave light pulses as beam splitters. It will demonstrate the diffraction effect on the atomic waves with three different cases. We first go through two extreme situations that are the far-off resonant and on-resonant standing waves and then the near-resonant standing wave.

2.3.1 Far-off-resonance light

In the case of a far-off-resonance standing wave ($\Delta \gg \Gamma$), we have $\Delta + \Gamma \approx \Delta$. To the second order we take the detuning to be much greater than the Rabi frequency $\frac{\Omega^2}{\Delta^2} \approx 0$,

such that the eigenvalues $\lambda_{1,2}$ in Eq. 2.24 can be reformed by using Taylor expansion:

$$\begin{aligned}\lambda_1 &= -\left(\hbar\Delta + \frac{\hbar\Omega^2}{4\Delta}\cos^2(k_L x)\right), \\ \lambda_2 &= \frac{\hbar\Omega^2}{4\Delta}\cos^2(k_L x),\end{aligned} \tag{2.33}$$

where we ignore any order that is higher than 2. Subsequently we can show $\frac{\lambda_2}{\lambda_1} \approx 0$:

$$\begin{aligned}\frac{\lambda_2}{\lambda_1} &= -\frac{\frac{\hbar\Omega^2}{4\Delta}\cos^2(k_L x)}{\left(\hbar\Delta + \frac{\hbar\Omega^2}{4\Delta}\cos^2(k_L x)\right)} \\ &= -\frac{\hbar\Omega^2\cos^2(k_L x)}{4\Delta\left(\hbar\Delta + \frac{\hbar\Omega^2}{4\Delta}\cos^2(k_L x)\right)} \\ &= -\frac{\hbar\Omega^2\cos^2(k_L x)}{4\hbar\Delta^2\left(1 + \frac{\Omega^2}{\Delta^2}\frac{\cos^2(k_L x)}{4}\right)} \\ &\approx -\frac{\Omega^2}{\Delta^2}\frac{\hbar\cos^2(k_L x)}{4\hbar} \\ &\approx 0\end{aligned} \tag{2.34}$$

Using the results from Eq. 2.33 and Eq. 2.34, the grating operator G in Eq. 2.28 becomes the familiar unitary phase grating operator:

$$\begin{aligned}G(x,\tau) &= \frac{1}{1-\frac{\lambda_2}{\lambda_1}}\left(\mathrm{e}^{-\frac{i}{\hbar}\lambda_2\tau} - \frac{\lambda_2}{\lambda_1}\mathrm{e}^{-\frac{i}{\hbar}\lambda_1\tau}\right) \\ &\approx \exp\left(-\frac{i}{\hbar}\frac{\hbar\Omega^2}{4\Delta}\cos^2(k_L x)\,\tau\right) \\ &= \exp\left(-\frac{i}{\hbar}\frac{\hbar\Omega^2}{8\Delta}\cos(2k_L x)\,\tau\right) \\ &= \exp\left(-i\phi_d\cos(2k_L x)\right),\end{aligned} \tag{2.35}$$

where $\phi_d = \Omega^2\tau/8\Delta$ is the kicking strength [66]. In this case, the light yields a conservative spatially periodic potential [72, 73] and the grating operator only affects the phase of the atomic wave function.

Now consider a plane atomic wave $|p_0\rangle$, where p_0 is the initial momentum along the standing-wave axis. After exposed to a short standing wave, the atomic wave function is

given by:

$$\begin{aligned}\Psi &= G(x,\tau)|p_0\rangle \\ &= \exp\left(-i\phi_d \cos\left(2k_L x\right)\right)|p_0\rangle \\ &= \sum_{n=-\infty}^{+\infty} (-i)^n J_n\left(\phi_d\right) \exp\left(in2k_L x\right)|p_0\rangle \\ &= \sum_{n=-\infty}^{+\infty} (-i)^n J_n\left(\phi_d\right)|p_0 + n2\hbar k_L\rangle,\end{aligned} \tag{2.36}$$

where we use the Jacobi-Anger expansion to expand the term $\exp\left(-i\phi_d \cos\left(2k_L x\right)\right)$. J_n is the Bessel function of the first kind, and $\exp\left(in2k_L x\right)$ is a translation operator that shifts the wave function in momentum space. From Eq. 2.36, we see that the initial plane wave is diffracted into a coherent superposition of different momentum states $|p_0 + n2\hbar k_L\rangle$, and the amplitude for the nth order diffraction is $J_n(\phi_d)$.

Equation 2.36 shows that a short far-off-resonance standing-wave pulse can split atomic waves into superpositions of momentum states that differ by $2\hbar k_L$ without changing the internal state. This can be visually understood in Fig. 2.4(c), where the incident atomic wave is split into a discrete orders separated by $2\hbar k_L$. The far-off-resonance standing-wave pulse has acted as a phase grating.

2.3.2 On-resonance light

Another extreme case is when the standing-wave light is on-resonant ($\Delta = 0$). The grating operator G is a spatially varying function, which has no phase component in it [86]. We again consider a plane atomic wave $|p_0\rangle$. After exposing to a brief pulse, the atomic wave is given by [52]:

$$\Psi = \sum_{n=-\infty}^{+\infty} \exp\left(-\frac{\Omega^2}{\Gamma}\tau\right) I_n\left(-\frac{\Omega^2}{\Gamma}\tau\right)|p_0 + n2\hbar k_L\rangle, \tag{2.37}$$

where Ω denotes the Rabi frequency and I_n is the modified Bessel function [101]. We once again see the quantization of the atomic momentum in the unit of $2\hbar k_L$. This indicate that the on-resonant standing-wave light pulse can be used as a beam splitter in a multi-path

atomic interferometers [52].

2.3.3 Near-resonance light

When the standing-wave light frequency is near to an open atomic transition ($\Delta \sim \Gamma$), G in Eq. 2.28 or 2.32 can be rearranged in a form of:

$$G(x,\tau) = A(x,\tau)\exp\left[-i\phi(x,\tau)\right], \tag{2.38}$$

where $A(x,\tau)$ and $\phi(x,\tau)$ are the functions of the position x and pulse duration τ. $A(x,\tau) \in [0,1]$ and $\phi(x,\tau) \in [0,2\pi)$ for all x and τ. It simultaneously modulates the phase and amplitude of the atomic wave function.

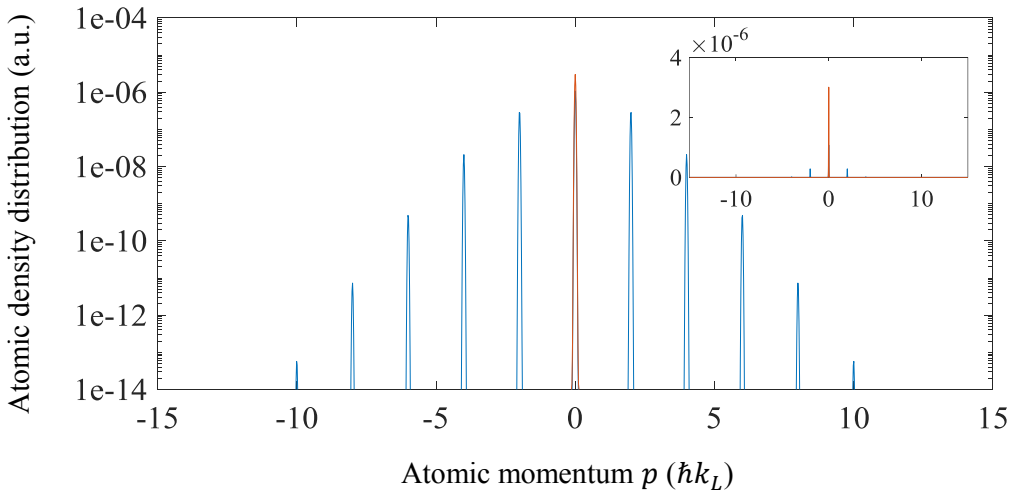

Figure 2.5: The momentum space representation of atomic density before (red line) and after (blue lines) a near-resonant standing wave light pulse based on Eq. 2.32.

To demonstrate the effect of the near-resonant standing-wave light pulse on the atoms, we show a momentum space representation of the atomic density before and after a pulse in Fig. 2.5.

To clearly resolve different diffraction orders after the pulse, we conduct the calculation by using a Gaussian atomic wave packet with a width much less than $2\hbar k_L$ (see the red

peak in Fig. 2.5). We then expose this wave packet to a standing wave pulse that is 10 MHz red detuned to the $F = 3$ to $F' = 3$ transition. After the pulse, the wave function of the atoms remaining in their initial state is split into a number of diffraction orders. The momentum space density distribution resembles a comb with a tooth spacing of $2\hbar k_L$ (see the blue peaks in Fig. 2.5). Integrating the probability density shows a loss of 93% of the atomic population in the initial ground state.

From Fig. 2.5, we see that the near-resonant standing wave light pulse can coherently diffract the atomic waves into a superposition of the momentum states that are differing by $2\hbar k_L$. It is therefore can also be used as a matter-wave beam splitter.

2.4 Summary

The standing-wave light pulse provides a powerful tool for making a matter-wave beam splitter. We mathematically derived the expression of the electric field of the standing-wave light beam, and also theoretically investigated the atom-light interaction with the two-level and four-level models, respectively. The grating operator G describes the effect of the standing-wave pulse on the atomic waves. Using it, we found the atomic waves are split into a number of diffraction orders separated by $2\hbar k_L$. When the light frequency is tuned near to an open atomic transition, both the phase and amplitude of the wave function are modulated. The near-resonance standing-wave light pulse therefore acts as a hybrid of phase and amplitude grating.

Chapter 3

The evolution of an atom optics driven system

In atom interferometry, the sensitivity typically scales linearly with the space-time area enclosed by different diffraction arms [26, 59]. This means to obtain a meaningful signal requires a wait time after splitting the atomic waves into different paths. The chapter describes how the atomic wave function evolves during the waiting time after a standing-wave light pulse. Particularly, the section will address two renowned near-field diffraction phenomena that are the matter-wave Talbot and Talbot-Lau effects, which happen for particular combinations of the initial conditions and the pulse intervals. It subsequently reveals the dynamics of the system after a train of pulses utilizing the dynamics during the pulse and the evolution between pulses. This enables us to simulate the outputs of the experiments. We show a protocol for performing gravity measurement and give a theoretical description of the system's dynamics in the presence of the local gravitational field.

3.1 Free evolution between pulses

After being split by the standing-wave light pulse, the atomic wave function evolves freely, which leads to a dispersion of the atomic waves without changing the internal state of the atom. The evolution is governed by the Schrödinger equation [95]:

$$i\hbar\frac{\partial|\psi\rangle}{\partial t} = H_{\text{free}}|\psi\rangle, \tag{3.1}$$

where the free evolution Hamiltonian is $H_{\text{free}} = \frac{p^2}{2M}$ with p the momentum operator and M the mass of the atom. After a time T, the wave function $|\psi, T\rangle$ is then given by [95]:

$$\begin{aligned} |\psi, T\rangle &= F(T)|\psi, 0\rangle \\ &= \exp\left(-\frac{i}{\hbar}\frac{p^2}{2M}T\right)|\psi, 0\rangle, \end{aligned} \tag{3.2}$$

where $|\psi, 0\rangle$ is the initial wave function, and $F(T)$ the time evolution operator.

3.2 Survival resonances

We now study the conditions for observing the matter-wave Talbot and Talbot-Lau effects by utilizing the grating operator G given in Chapter 2 and the time evolution operator $F(T)$ in Eq. 3.2. These two effects are the physical principle that underpins the survival resonances.

3.2.1 The Matter-wave Talbot effect

The Talbot effect is a near-field diffraction phenomenon, which was discovered by Henry Fox Talbot using light in 1836 [102]. When a monochromatic plane wave incidents on a diffraction grating, it will form a self-image of the grating itself downstream at a series of regular distances. The Talbot distance $L_{\text{T}} = 2d^2/\lambda$ separates these distances, where d is the grating periodicity and λ the wavelength of the incident light [103].

In analogy to the light Talbot effect [103], we can use de Broglie matter waves to observe such phenomena. Early experiments were carried out by using atomic beams diffracted

by nanostructure gratings [88, 104, 105]. In later experiments, that were conducted in the time domain [106], where the material gratings were replaced by pulsed laser beams. The Talbot time T_{T} is a key parameter for understanding the formation of the Talbot fringes.

To mathematically address the matter-wave Talbot effect, we consider a plane wave $|p_0\rangle$, where p_0 is the initial atomic momentum. After exposure to a standing-wave pulse, it is then split and has the form of $\sum_n c_n|p_0 + n2\hbar k_L\rangle$, where $n \in \mathbb{Z}$ and c_n denotes the amplitude of the n^{th} diffraction order (see for example Eqs. 2.36 and 2.37). Applying the time evolution operator $F(T)$ from Eq. 3.2 gives:

$$\begin{aligned}
|\psi, T\rangle &= F(T) \sum_{n=-\infty}^{+\infty} c_n |p_0 + n2\hbar k_L\rangle \\
&= \sum_{n=-\infty}^{+\infty} c_n \exp\left(-\frac{i}{\hbar}\frac{p^2}{2M}T\right)|p_0 + n2\hbar k_L\rangle \\
&= \sum_{n=-\infty}^{+\infty} c_n \exp\left(-\frac{i}{\hbar}\frac{(p_0 + n2\hbar k_L)^2}{2M}T\right)|p_0 + n2\hbar k_L\rangle \\
&= \exp\left(-\frac{i}{\hbar}\frac{p_0^2}{2M}T\right)\sum_{n=-\infty}^{+\infty} c_n \exp\left[-i\left(\frac{p_0}{\hbar k_L}n + n^2\right)\frac{2\hbar k_L^2}{M}T\right]|p_0 + n2\hbar k_L\rangle,
\end{aligned} \tag{3.3}$$

where the global phase term $\exp\left(-\frac{i}{\hbar}\frac{p_0^2}{2M}T\right)$ has no physical significance. Now let's pay a closer attention to the phase term related to n:

$$\phi_n(T) = \left(\frac{p_0}{\hbar k_L}n + n^2\right)\frac{2\hbar k_L^2}{M}T. \tag{3.4}$$

The time T when the non-bracketed part becomes 2π is of extraordinary importance. This is the **Talbot time** T_{T} and is given by [67]:

$$T_{\mathrm{T}} = \frac{\pi M}{\hbar k_L^2}. \tag{3.5}$$

When p_0 equals to the integer multiples of $\hbar k_L$ and $T = T_{\mathrm{T}}$, Eq. 3.4 yields only integer multiples of 2π for all n [1]. This particular combination leads $F(T_{\mathrm{T}})$ to become an identity

[1] In a conventional AODKR, having $p_0 = n\hbar k_L$ ($n \in \mathbb{Z}$) and $T = T_{\mathrm{T}}$ leads N standing-wave pulses to effectively act as one pulse with a kicking strength of $N\phi_d$ that is N times larger than ϕ_d [67], where ϕ_d (see Eq. 2.35) is the kicking strength for the standard AODKR.

operator and the wave function revises completely at this time.

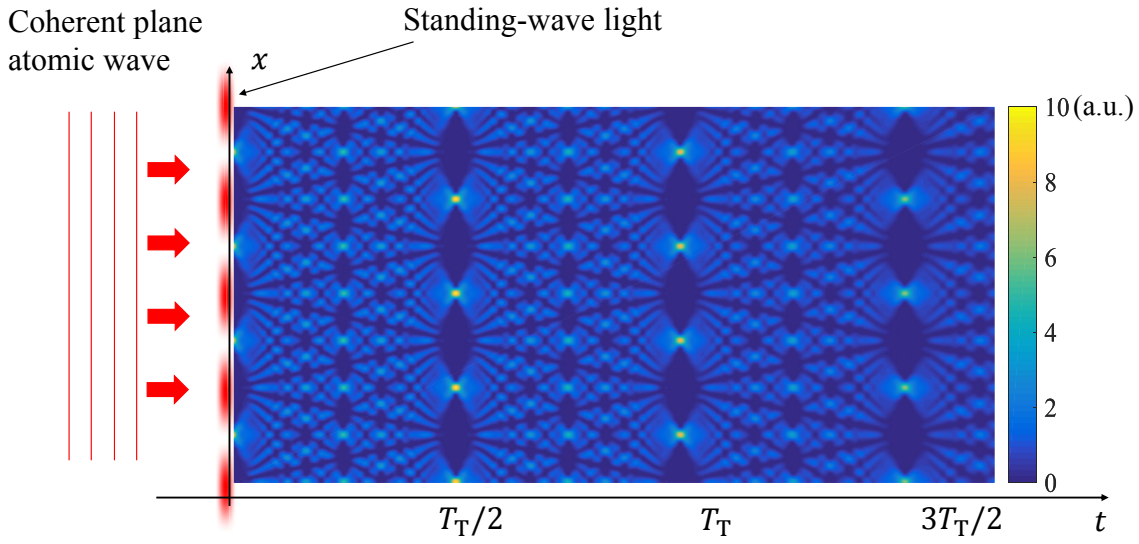

Figure 3.1: The matter-wave Talbot effect. The color map represents the calculated atomic density distribution at time t after a standing-wave light pulse. The horizontal axis is t, and the vertical axis is the coordinate along the standing wave. The red lines represent the coherent plane wave.

Figure 3.1 shows how a monoenergetic plane wave with $p_0 = 0$ evolves after exposure to an absorption grating. The color code shows the atomic density at position x and time t, where the atoms are localized at the bright spots in the figure. The atomic density distribution forms a perfect self-image of the standing wave at $t = T_T$. If we apply a second pulse when this high contrast distribution forms, it will have a high chance to survive it since most of the atoms are localized around the nodes of the standing wave.

3.2.2 The Matter-wave Talbot-Lau effect

To observe the matter-wave Talbot effect, we need to have a very small dispersion of the matter-wave packets for achieving a high resolution and good signal-to-noise. Using a Bose-Einstein condensate (BEC) or velocity-selected atoms can fulfill the small dispersion

requirement. In other words, these are two different variations of coherent sources [106].

It is not possible to observe the Talbot interference pattern when using a cloud of thermal atoms. This is because we can view a thermal cloud of atoms as an incoherent sum of plane-waves, which contain a wide range of momentum components. After one single pulse, different diffraction orders from all the initial momentum components will incoherently superpose and wash out the interferometric fringes. Nevertheless, if we place a second grating at time T, the combination of these two grating will form a velocity filter [92] and a coherent echo will be set up at the same time T after the second grating. This two-grating configuration is the so called Lau scheme or Talbot-Lau scheme [107]. To see the echo-phenomenon, this sub-section will outline a calculation of the expected signal by using the method provided in the Refs. [103, 108, 109].

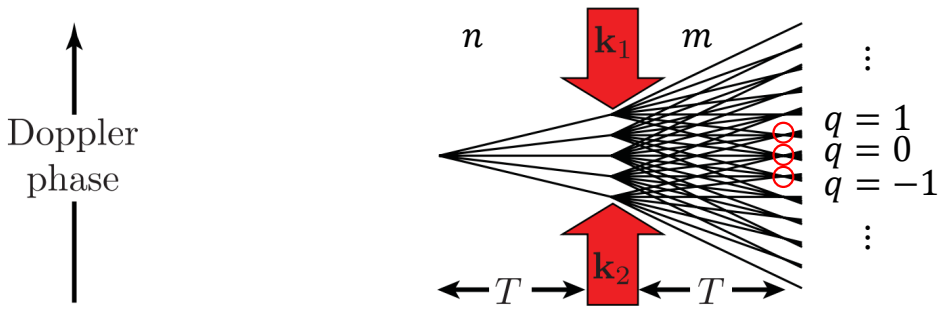

Figure 3.2: Doppler phase diagram for atoms split by the standing wave pulses [108].

We carry out the calculation by first considering the signal for a well-defined initial momentum $p_0 = Mv_0 = \hbar k_0$ (where we ignore the vector properties by restricting the momentum along the standing-wave propagation direction), and then integrating this signal over the initial momentum distribution $\varrho(p_0)$ of the thermal atomic cloud. We assume that the atomic wave function just before the standing wave light pulse is $\psi_{k_0}(x, 0-) = \exp(ik_0 x)$.

After exposing to a brief standing wave light pulse (see the grating operator G in Eq. 2.38), the wave function is split into a number of diffraction orders and has the form of:

$$\psi_{k_0}(x, 0+) = \sum_n c_n \exp[i(k_0 + 2nk_L)x], \tag{3.6}$$

where $n \in \mathbb{Z}$ and c_n represents the amplitude of the n-th diffraction order (see Fig. 3.2). After switching off the light pulse at $t = 0$, the wave function freely evolves for a duration T. Apply the time evolution operator $F(T)$ from Eq. 3.2, the atomic wave function just before the second pulse has the form:

$$\begin{aligned} \psi_{k_0}(x, T-) &= F(T) \sum_n c_n \exp[i(k_0 + 2nk_L)x] \\ &= \sum_n c_n \exp\left[-i\frac{\hbar(k_0 + 2nk_L)^2}{2M}T\right] \exp[i(k_0 + 2nk_L)x]. \end{aligned} \tag{3.7}$$

We see that each plane wave component, $\exp[i(k_0 + 2nk_L)x]$ in Eq. 3.7, acquires a phase $\phi = (\omega_{k_0} + n^2\omega_{2k_L} + n2k_Lk_0)T$ due to the free evolution. $\omega_{k_0} = \frac{\hbar k_0^2}{2M}$ contributes to a global phase that has no physical significance, $\omega_{2k_L} = \frac{\hbar(2k_L)^2}{2M}$ is the (two-photon) recoil frequency, and $n(2k_L)v_0T$ is the Doppler phase, which is proportional to the initial atomic velocity $v_0 = \frac{\hbar k_0}{M}$ [108].

At time $t = T$, applying a second pulse further diffracts the atomic wave function to have a form of:

$$\psi_{k_0}(x, T+) = \sum_m \sum_n c_m c_n \exp\left[-i\frac{\hbar(k_0 + 2nk_L)^2}{2M}T\right] \exp[i(k_0 + 2(n + m)k_L)x]. \tag{3.8}$$

Similar to the index number n, in Eq. 3.8, $m \in \mathbb{Z}$ and c_m indicates the amplitude of the m-th diffraction order due to the second pulse (see Fig. 3.2). After the second pulse, we evolve the wave function for another time T in the same manner as in Eq. 3.7, giving the

result:

$$\begin{aligned}\psi_{k_0}(x,2T) &= \sum_m \sum_n c_m c_n \exp\left[-i\frac{\hbar(k_0+(m+n)2k_L)^2}{2M}T\right]\exp\left[-i\frac{\hbar(k_0+2nk_L)^2}{2M}T\right] \\ &\quad \times \exp[i(k_0+2(m+n)k_L)x] \\ &= \sum_m \sum_n c_m c_n \exp\left[-i\frac{\hbar T}{2M}\left(2k_0^2+(m^2+2n^2+2mn)(2k_L)^2+(m+2n)(4k_0k_L)\right)\right] \\ &\quad \times \exp[i(k_0+(m+n)2k_L)x] \\ &= \exp\left[i\left(k_0x-2\omega_0T\right)\right]\sum_m\sum_n c_m c_n \\ &\quad \exp\left[-i\frac{\hbar T}{2M}\left((m^2+2n^2+2mn)(2k_L)^2+4(m+2n)k_0k_L\right)\right]\exp[i(m+n)2k_Lx].\end{aligned} \tag{3.9}$$

Figure 3.2 illustrates a diagram of the evolution of the Doppler phase for various amplitudes as a function of the time. The lines cross when different momentum states have the same Doppler phase. At these times, the Doppler free atomic interferometric patterns will emerge [108].

To simplify the calculation, we turn the attention to the q-th bundle that labels the crossing of different momentum states (see red circles in Fig. 3.2). Instead of summing over n and m, we sum the wave function over n and q thanks to the one-to-one correspondence relation $m = q - 2n$. $\psi_{k_0}(x,2T)$ in Eq. 3.9 is therefore given by:

$$\begin{aligned}\psi_{k_0}(x,2T) =& \exp\left[i\left(k_0x-2\omega_0T\right)\right]\sum_n\sum_{q-2n} c_{q-2n}c_n \\ & \exp\left[-i\frac{\hbar T}{2M}\left((q^2+2n^2-2qn)(2k_L)^2+2qk_0(2k_L)\right)\right]\exp[i(q-n)2k_Lx].\end{aligned} \tag{3.10}$$

The atomic density $\rho_{k_0}(x,2T) \equiv \psi^*_{k_0}(x,2T)\psi_{k_0}(x,2T)$ resulting from the initial wave vector k_0 is given by:

$$\begin{aligned}\rho_{k_0}(x,2T) =& \sum_{n'}\sum_{n}\sum_{q-2n}\sum_{q'-2n'} c^*_{q'-2n'}c^*_{n'}c_{q-2n}c_n \\ & \exp\Bigg[-i\frac{\hbar T}{2M}\Bigg((q^2-q'^2)(2k_L)^2+2(n^2-n'^2)(2k_L)^2+2(q-q')k_0(2k_L) \\ & -2(qn-q'n')(2k_L)^2\Bigg)\Bigg]\exp[i(q-q'+n'-n)2k_Lx].\end{aligned} \tag{3.11}$$

The spatial atomic density distribution is then given by averaging Eq. 3.11 over the initial momentum distribution $\varrho(p_0=\hbar k_0)$:

$$\rho(x,2T) = \int \varrho(k_0)dk_0\rho_{k_0}(x,2T). \tag{3.12}$$

When $q \neq q'$, the k_0-dependent term, $\exp\left[\frac{\hbar T}{2M}2(q-q')k_0(2k_L)\right]$ in Eq. 3.11 is rapidly oscillating and the Eq. 3.12 integrates to zero. When $q = q'$, $\rho(x,2T)$ in Eq. 3.11 is k_0-independent. Since $\int \varrho(k_0)dk_0$ integrates to 1. Equation 3.12 becomes:

$$\begin{aligned}\rho(x,2T) =& \sum_{n'}\sum_{n}\sum_{q-2n}\sum_{q-2n'} c^*_{q-2n'}c^*_{n'}c_{q-2n}c_n \\ & \exp\left[-i\frac{\hbar T}{2M}2(2k_L)^2\Bigg((n^2-n'^2)-q(n-n')\Bigg)\right]\exp[i(n'-n)2k_Lx].\end{aligned} \tag{3.13}$$

When $T = T_{\mathrm{T}}/2$, the first exponential term becomes an identity operator I. The atomic density $\rho(x,2T)$ therefore has the form:

$$\rho(x,2T) = \sum_{n'}\sum_{n}\sum_{q-2n}\sum_{q-2n'} c^*_{q-2n'}c^*_{n'}c_{q-2n}c_n\exp[i(n'-n)2k_Lx]. \tag{3.14}$$

We can further simplify the summation of Eq. 3.14 by defining $\chi = n'-n$, where $\chi \in \mathbb{Z}$. For a specific χ, n and n' have the one-to-one relation $n' = n+\chi$, and the sum in Eq. 3.14 can be rewritten as:

$$\rho_\chi(x,2T) = \sum_{q-2n}\sum_{n} c^*_{q-2n-2\chi}c^*_{n+\chi}c_{q-2n}c_n\exp[i\chi 2k_Lx], \tag{3.15}$$

where the quadruple sum reduces to a double sum. We can simplify Eq. 3.15 by using the

relation $m = q - 2n$:

$$\rho_\chi(x, 2T) = \sum_m \sum_n c^*_{m-2\chi} c^*_{n+\chi} c_m c_n \exp[i\chi 2k_L x]. \tag{3.16}$$

Using κ ($\kappa \in \mathbb{N}$) to replace χ in Eq. 3.16 yields:

$$\begin{aligned} \rho_\kappa(x, 2T) = \sum_m \sum_n & c^*_{m-2\kappa} c^*_{n+\kappa} c_m c_n \exp[i\kappa 2k_L x] + \\ & c^*_{m+2\kappa} c^*_{n-\kappa} c_m c_n \exp[-i\kappa 2k_L x] \\ = A(\kappa) \exp[i\kappa 2k_L x] & + A^*(\kappa) \exp[-i\kappa 2k_L x]. \end{aligned} \tag{3.17}$$

The summation of Eq. 3.17 shows that the Fourier component with spatial frequency $\kappa 2k_L$ revives when $T = T_\mathrm{T}/2$. Summing over all κ-values gives a self-image shown in Fig. 3.3(a).

Figure 3.3(b) shows that the self-image forms when the time between the gratings is any integer multiples of half the Talbot time $T = nT_\mathrm{T}/2$ (where $n \in \mathbb{N}$). When these self-images form, if a third standing-wave pulse is applied, the matter wave has a high probability of survival since the atoms are localized around the nodes. When there are more than two pulses, from the third pulse and onwards, the previous two pulses will set up the self-image and ensure a high survival when $T = nT_\mathrm{T}/2$.

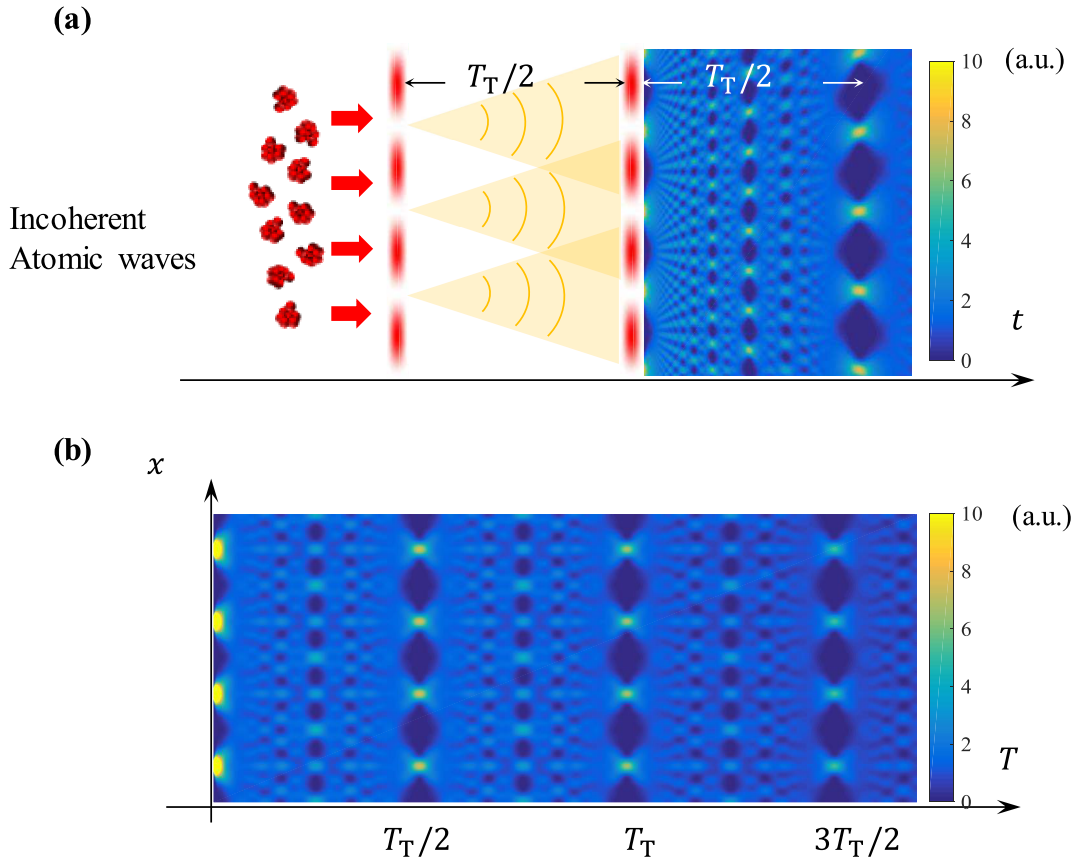

Figure 3.3: The matter-wave Talbot-Lau interference [50, 51]. The color code represents the atomic density and the vertical axis is the coordinate along the grating. (a) When impinging an incoherent atomic wave onto two identical gratings that are separated by a time $T_T/2$, a self-image forms the same time $T_T/2$ after the second grating. The horizontal axis is the total time t. (b) The atomic density distribution forms a series of self-images at the integer multiples of the half Talbot time when the two gratings are separated by the same time interval.

3.3 Dynamics during a pulse sequence

This thesis has so far given the atomic motion in the standing-wave light field (see Chapter 2) and the evolution of the atom in free space (see Section 3.1). We will then use these results to investigate the dynamics of the atom when exposing it to a standing-wave pulse sequence shown in Fig. 3.4. This is to compute the survival probability of the atoms

remaining in their initial state [50].

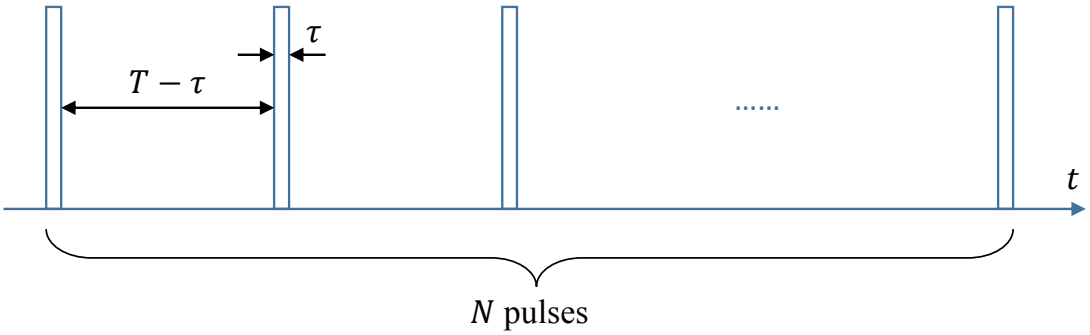

Figure 3.4: The diagram of a typical N-pulse train with the pulse duration τ and pulse interval $T-\tau$, where T is the pulse period.

Figure 3.4 illustrates that the pulse train is shaped to have a series of a top-hat profile with the pulse period T and pulse duration τ, we can therefore divide the time evolution into two segments: the dynamics during the pulse (described by the grating operator $G(x,\tau)$ from Eq. 2.38) and free dynamics between pulses (given by the time evolution operator $F(T)$ in Eq. 3.2). Exploiting the time evolution of the two situations, we can therefore find the pulse-to-pulse time evolution operator $U(T)$ as their product:

$$U(T) = F(T-\tau)G(x,\tau), \tag{3.18}$$

Recall that $G(x,\tau)$ only operates on the atoms in their initial ground state and $F(T-\tau)$ does not change the internal state of the atoms, so $U(T)$ gives the dynamics of the wave function of the atoms remaining in the initial ground state. Similar to Chapter 2, we take the F = 3 hyperfine ground state as the initial ground state. After receiving N pulses, the atomic wave function $|\psi_3, NT\rangle$ is then given by:

$$|\psi_3, NT\rangle = U^N(T)|\psi_3, 0\rangle, \tag{3.19}$$

where $|\psi_3, 0\rangle$ is the initial atomic wave function. Since $G(x,\tau)$ is non-unitary, so is this evolution. The probability for atoms surviving in the F = 3 ground state is $\langle\psi_3, NT|\psi_3, NT\rangle$, which can be measured experimentally by the state detection (see Chapter 5).

When there are more than two pulses ($N \geq 2$), the previous two pulses will ensure that the atoms are near the nodes of the standing wave whenever $T = nT_{\mathrm{T}}/2$. This leads the atoms to survive the pulses and shows resonances [50, 86].

3.4 In presence of gravity

This section turns the attention to the evolution of the system in the presence of the local gravitational field [51]. We consider the gravitational potential Mgx, where g is the local gravitational acceleration. Additionally, we consider a time-dependent standing-wave light beam with a vertical arrangement, which can move spatially with a constant acceleration a (see Eq. 2.8) to match the free-falling frame of the atoms. For explanatory convenience, we will outline the derivations using the two-level model (see sub-Section 2.2.1), with the F = 3 hyperfine ground state as the initial ground state (see Fig. 2.2). It can be upgraded to the more advanced four-level model which is given in the end of this section.

The system Hamiltonian, after we introduce the gravitational potential and the electric field from Eq. 2.8, is given by:

$$\begin{aligned} H =& \frac{p^2}{2M} + Mgx - \left(\hbar\Delta + \frac{i\hbar\Gamma}{2}\right)|e\rangle\langle e| \\ &+ \frac{\hbar\Omega}{2}\cos\left[k_L\left(x + \frac{1}{2}at^2\right)\right](|e\rangle\langle 3| + |3\rangle\langle e|) \times \sum_{n'=0}^{N} \Pi\left(t - n'T, \tau\right), \end{aligned} \tag{3.20}$$

where $\sum_{n'=0}^{N}\Pi(t - n'T, \tau)$ is a series of top-hat functions with the pulse period T and pulse duration τ. The index n' shows the current pulse number, where $n' \in \mathbb{N}$.

The Hamiltonian H in Eq. 3.20 gives the full description of the system. In principle, one can use it to compute all the physical quantities that are of interest. Nevertheless, it is desirable to simplify the calculations by transforming H to a convenient frame. In this section, I will do this by preforming two gauge-transformations (with detailed derivations provided in Appendix B).

We first translate the wave function to a frame that moves at the standing-wave ac-

celeration a in position space by using the translation operator $\mathcal{T}(\Delta x) = \exp(i\Delta x p/\hbar)$ (with $\Delta x = \frac{at^2}{2}$). The gauge-transformed state $|\widetilde{\psi}\rangle = \mathcal{T}^\dagger|\psi\rangle$ is therefore governed by the Hamiltonian $\widetilde{H} = \mathcal{T}^\dagger H \mathcal{T} + atp$. H in Eq. 3.20 is therefore transformed to:

$$\begin{aligned}\widetilde{H} =& \frac{p^2}{2M} + Mg\left(x - \frac{1}{2}at^2\right) + apt - \left(\hbar\Delta + \frac{i\hbar\Gamma}{2}\right)|e\rangle\langle e| \\ &+ \frac{\hbar\Omega}{2}\cos(k_L x) \times \sum_{n'=0}^{N} \Pi\left(t - n'T, \tau\right) \times \left(|e\rangle\langle 3| + |3\rangle\langle e|\right).\end{aligned} \tag{3.21}$$

Now the standing wave is stationary, and the computation of the grating operator from Chapter 2 is again valid. However, the system is not spatially periodic because of the Mgx term.

To further simplify the Hamiltonian $\widetilde{H}$ in Eq. 3.21, we apply another gauge-transformation: $\mathcal{U}(\Delta p) = \exp(-ix \cdot \Delta p/\hbar)$ (with $\Delta p = Mgt$). The gauge-transformed state $|\widetilde{\widetilde{\psi}}\rangle = \mathcal{U}^\dagger|\widetilde{\psi}\rangle$ is then governed by the Hamiltonian $\widetilde{\widetilde{H}} = \mathcal{U}^\dagger \widetilde{H} \mathcal{U} - Mgx$. $\widetilde{H}$ in Eq. 3.21 is then transformed to:

$$\begin{aligned}\widetilde{\widetilde{H}} =& \frac{p^2}{2M} - (g-a)\,pt + \frac{Mg}{2}(g-3a)\,t^2 - \left(\hbar\Delta + \frac{i\hbar\Gamma}{2}\right)|e\rangle\langle e| \\ &+ \frac{\hbar\Omega}{2}\cos(k_L x) \times \sum_{n'=0}^{N} \Pi\left(t - n'T, \tau\right) \times \left(|e\rangle\langle 3| + |3\rangle\langle e|\right).\end{aligned} \tag{3.22}$$

After these two consecutive gauge-transformations, we now have a spatially periodic system and a stationary standing wave. This comes at the expense of having an explicit time-dependence of $\widetilde{\widetilde{H}}$ when the standing-wave light is off. The dynamics between pulses is now governed by the Hamiltonian $\widetilde{\widetilde{H}} = \frac{p^2}{2M} - (g-a)\,pt$, where we have omitted the term $\frac{Mg}{2}(g-3a)\,t^2$ since it only adds a global phase that has no physical significance.

Equation 3.22 is well suited for performing numerical calculations. During the pulse, invoking the Raman-Nath approximation, the grating operator G from Eq. 2.32 completely describes the evolution of the wave function of the atoms remaining in the F = 3 initial ground state. Importantly, since the gauge-transformed standing-wave pattern does not move spatially, we only need to calculate the grating operator once.

Between the pulses, the atoms undergo a free dynamics governed by the Hamiltonian $\widetilde{\widetilde{H}} = \frac{p^2}{2M} - (g-a)\,pt$. Although $\widetilde{\widetilde{H}}$ is explicitly time-dependent, it commutes

with itself at different times, which enables us to construct a time evolution operator $\widetilde{\widetilde{F}} = \exp\left(-\frac{i}{\hbar}\int_{t_1}^{t_2}\widetilde{\widetilde{H}}dt\right)$ from t_1 to t_2. In particular, we can establish the one-period time evolution operator $\widetilde{\widetilde{F}}_{n'}$ from $t = (n'-1)T$ to $t = n'T$:

$$\widetilde{\widetilde{F}}_{n'} = \exp\left(-\frac{i}{\hbar}\frac{p^2}{2M}T\right)\exp\left(\frac{i}{\hbar}\left[\frac{p\,(g-a)}{2}\left(2n'-1\right)\right]T^2\right). \tag{3.23}$$

In Eq. 3.23, the first term arises from the atomic kinetic energy. The second term incorporates the effect of gravity. When the acceleration of the standing wave a matches g, it becomes the identity operator and the system becomes equivalent to one where the atoms receive pulses horizontally (see Section 3.3).

Similar to Section 3.3, we can now obtain an expression for the time evolution operator after a N-pulse train. Taking the advantage of the temporal periodicity of the pulse sequence, we can construct a pulse-to-pulse evolution operator $\widetilde{\widetilde{U}}_{n'} = \widetilde{\widetilde{F}}_{n'}G$, from $t = (n'-1)T$ to $t = n'T$. Since $\widetilde{\widetilde{F}}_{n'}$ does not change the internal state of the atoms, $\widetilde{\widetilde{U}}_{n'}$ gives the dynamics of the wave function of the atoms remaining in the F = 3 initial ground state. After receiving N pulses, the atomic wave function $|\widetilde{\widetilde{\psi}}_3, NT\rangle$ is given by:

$$|\widetilde{\widetilde{\psi}}_3, NT\rangle = \widetilde{\widetilde{U}}_N\widetilde{\widetilde{U}}_{N-1}\cdots\widetilde{\widetilde{U}}_1|\widetilde{\widetilde{\psi}}_3, 0\rangle, \tag{3.24}$$

Since G is non-unitary, so is this evolution. Equation 3.24 allows for the computation of the survival probability as $\langle\widetilde{\widetilde{\psi}}_3, NT|\widetilde{\widetilde{\psi}}_3, NT\rangle$. There is no need for transferring $|\widetilde{\widetilde{\psi}}_3, NT\rangle$ back to its initial frame before computing the survival probability since the gauge-transformations are unitary so they do not change the survival probability.

The generalization to the four-level model is to replace the grating operator G from Eq. 2.28 to Eq. 2.32. Most of the numerical calculations in later chapters are based on the four-level model.

3.5 Numerical calculation

This section will introduce the approach of calculating the survival probability based on the dynamical evolution discussed in Sections 3.3 and 3.4, with the MATLAB code attached in Appendix A.

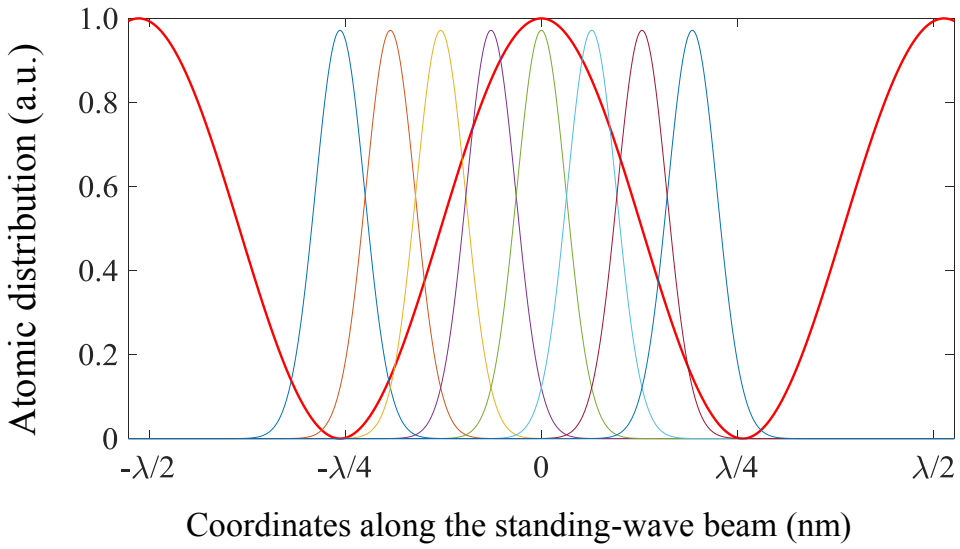

Figure 3.5: The ensemble of the initially Gaussian wave packets homogeneously cover one period of the standing-wave light field. The width of the Gaussian wave packets is determined by the initial temperature of the atomic cloud and that only few are plotted. The red line is an eye-guide for showing the intensity profile of the standing-wave light along the coordinate.

Figure 3.5 displays a set of initially Gaussian wave-packets that homogeneously cover one period of the standing-wave light. The width of the wave-packets is determined by the temperature of the atomic cloud. For a temperature of T_{temp}, the normalized momentum space wave function is [110]:

$$\phi(p) = \frac{1}{\sqrt{2\pi M k_{\text{B}} T_{\text{temp}}}} \exp\left(-\frac{p^2}{2M k_{\text{B}} T_{\text{temp}}}\right), \tag{3.25}$$

where p is the momentum, k_{B} the Boltzmann's constant, and M the mass of the atom.

The inverse Fourier-Transform gives the wave function in position space [95]:

$$\psi(x) = \frac{\sqrt{(2\pi M k_{\mathrm{B}} T_{\mathrm{temp}})}}{\hbar} \exp\left[-\frac{2\pi^2 M k_{\mathrm{B}} T_{\mathrm{temp}}}{\hbar^2} x^2\right]. \tag{3.26}$$

To simulate the distribution of the atomic cloud over the standing wave, we initiate $\psi(x - x_0)$ by employing a series of x_0-values that cover one period of the standing wave homogeneously (see Fig. 3.5).

We operate with G in position space where it is diagonal and then evolve the wave function between pulses in momentum space where $\widetilde{\widetilde{F}}_{n'}$ is diagonal. Fast Fourier Transform (FFT) and Inverse Fast Fourier Transform (IFFT) rapidly transfer the atomic wave function between these two spaces making the computation efficiently. Eventually, the survival probability compared to the experiments will be averaged over the initial ensemble.

3.6 Summary

This chapter studied the dynamics of an atomic wave function exposed to a standing-wave pulse sequence. The revival of the wave function gives rise to the observation of the matter-wave Talbot and Talbot-Lau effects. Using the temporal periodicity of the pulse sequence, we constructed a time evolution operator that can fully describe the dynamics of the system. We included the presence of the local gravitational field and an accelerating standing wave, yet we achieved easily computable expressions for the survival probability through a series of gauge-transformations. Finally, we outlined how to compute the survival probability numerically for an initial thermal atomic cloud.

Chapter 4

Laser cooling and trapping

The atomic interferometer described in this thesis requires a cloud of cold atoms to expose to the standing-wave light pulses. The atoms with low thermal expansion allow for a longer interrogation time, which can increase the precision of the measurement. It is therefore crucial to cool the atoms before we carry on the experiments. To reduce the thermal motion of the atoms, we use laser cooling technology to cool the ^{85}Rb atoms to ~ 5 μK. This chapter will present the basic concepts of the laser cooling, trapping, and the magneto-optical-trap (MOT). It also describes the polarization gradient cooling (PGC) that can further cool the atoms beyond the Doppler temperature limit.

4.1 Doppler cooling

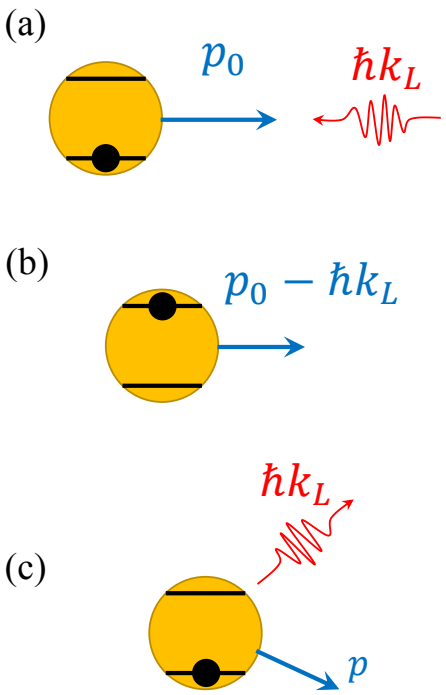

Figure 4.1: The mechanism of Doppler cooling. (a) A two-level atom moves at the momentum $\boldsymbol{p_0}$ toward a photon that has momentum $\hbar\boldsymbol{k_L}$. (b) The atom absorbs the photon and is excited to the higher level. The momentum decreases by amount of $\hbar k_L$. (c) The atom spontaneously decay back to the ground state and emits a photon. This results in the atom to move with momentum $\boldsymbol{p}$.

Laser cooling and trapping rely on the atom-photon interaction. Figure 4.1 illustrates the mechanism of the laser cooling. The photon carries energy $E = \hbar\omega_L$ and momentum $\boldsymbol{p} = \hbar\boldsymbol{k_L}$, where ω_L and $\boldsymbol{k_L}$ are the optical angular frequency and wave vector, respectively. In Fig. 4.1, we consider a two-level atom. When exposed to the light field, the atom absorbs a photon from the light beam and is pumped to the excited state. Meanwhile, the momentum carried by the photon transfers to the atom. This leads the atom to change its

monument by $\hbar \boldsymbol{k_L}$ [see Fig. 4.1(b)]. The atom in the excited state will then spontaneously decay back to the ground state and simultaneously emits a photon. The atom will gain a recoil momentum opposite to the momentum of the emitted photon [see Fig. 4.1(c)]. However, the spontaneous emission is in a random direction. The net momentum transfer due to spontaneous emissions averages to 0 after many absorption-emission cycles. While, the momenta from sequential absorptions build up, and the atom accelerate along the laser beam propagation direction. The force of light on the atom, that causes this acceleration, is named radiation pressure force [110–112]:

$$\boldsymbol{F} = \hbar \boldsymbol{k_L} R, \tag{4.1}$$

where R is the photon scattering rate:

$$R = \frac{\Gamma}{2} \frac{(I/I_{\text{sat}})}{1 + 4(\Delta/\Gamma)^2 + (I/I_{\text{sat}})}. \tag{4.2}$$

Δ is the laser detuning, Γ the decay rate, I the laser intensity and I_{sat} the saturation intensity [94,110,112]. In the low intensity case, the atom in a pair of counter-propagating laser beams experiences a net force $\boldsymbol{F} = \boldsymbol{F}_+ + \boldsymbol{F}_-$, where

$$\boldsymbol{F}_\pm = \pm \frac{\Gamma}{2} \hbar \boldsymbol{k_L} \frac{(I/I_{\text{sat}})}{1 + 4\left(\frac{\Delta \mp \boldsymbol{k_L v}}{\Gamma}\right)^2 + (I/I_{\text{sat}})}. \tag{4.3}$$

The laser detuning has the form of $\Delta \mp \boldsymbol{k_L v}$ due to the Doppler effect, with $\boldsymbol{v}$ the velocity of the atom. The net force is then given by:

$$\boldsymbol{F} \simeq \frac{8\hbar k_L^2 \frac{\Delta}{\Gamma} \frac{I}{I_{\text{sat}}}}{\left[1 + \frac{I}{I_{\text{sat}}} + 4\left(\frac{\Delta}{\Gamma}\right)^2\right]^2} \boldsymbol{v} = -\alpha \boldsymbol{v}, \tag{4.4}$$

where we have neglected the terms of order $(\boldsymbol{k_L v}/\Gamma)^4$ and higher. The negative sign comes from the red-detuned laser light. Equation 4.4 shows the net force is in the opposite direction of the atomic velocity. Therefore, a moving atom reduces its velocity in counter-propagating laser beams. When exposing atoms to three such laser pairs that are orthogonal to each other, the resulting force will damp the atomic motion in three

dimensions. This laser beam arrangement is known as optical molasses since the atomic motion is damped as they were traveling in a viscous fluid.

We now know that the absorption of photons followed by spontaneous decay process can reduce the atomic kinetic energy. It is then natural to ask how low the Doppler cooling temperature can be. The equilibrium temperature arises as a balance between the cooling and heating mechanisms.

For an atom with velocity $\boldsymbol{v}$, the cooling power is $\boldsymbol{F}\cdot\boldsymbol{v}$, with $\boldsymbol{F}$ from Eq. 4.4. The cooling power is thereby proportional to $\boldsymbol{v}^2$. The heating comes from the recoil of spontaneously emitted photons, which still provides a randomly fluctuating force, even though it averages to 0 after many cycles. The heating rate is proportional to the total scattering rate given in Eq. 4.2, which is independent of the atomic kinetic energy. Equating the heating and cooling rates yields the Doppler cooling limit [112]:

$$T_{\mathrm{Dopp}} = \frac{\hbar\Gamma}{2k_{\mathrm{B}}}, \tag{4.5}$$

where k_{B} is the Boltzmann's constant. For ^{85}Rb atom in our experiment, $T_{\mathrm{Dopp}} = 145.57\ \mu$K for the D2-line transition.

4.2 The Magneto-Optical-Trap

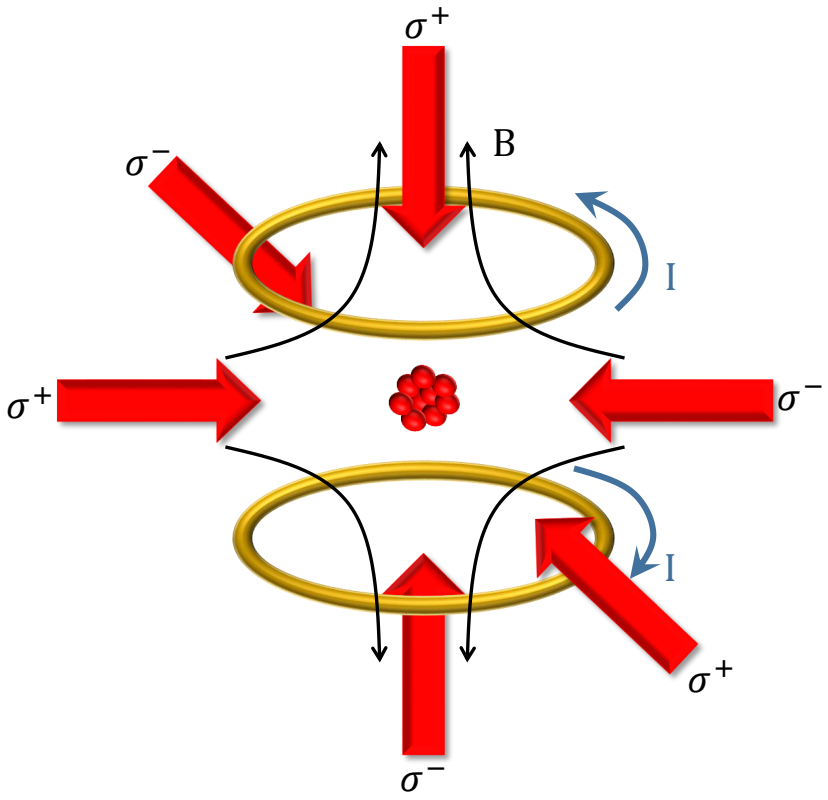

Figure 4.2: The schematic diagram of the magneto-optical trap (MOT). The anti-Helmholtz coils' center overlaps with the laser beams. The six beams are circularly polarized as labeled in the figure.

A Magneto-Optical Trap (MOT) provides a restoring force that prevents the atoms from diffusing out of the optical molasses by making use of a magnetic quadrupole field in addition to six cooling beams. Figure 4.2 displays the arrangement of the cooling lights and the magnetic field for constructing a MOT. The anti-Helmholtz coils generate a magnetic quadrupole field whose strength increases linearly along $x, y, z-$axes with a null point in the geometric center. This center is also where the six laser beams overlap.

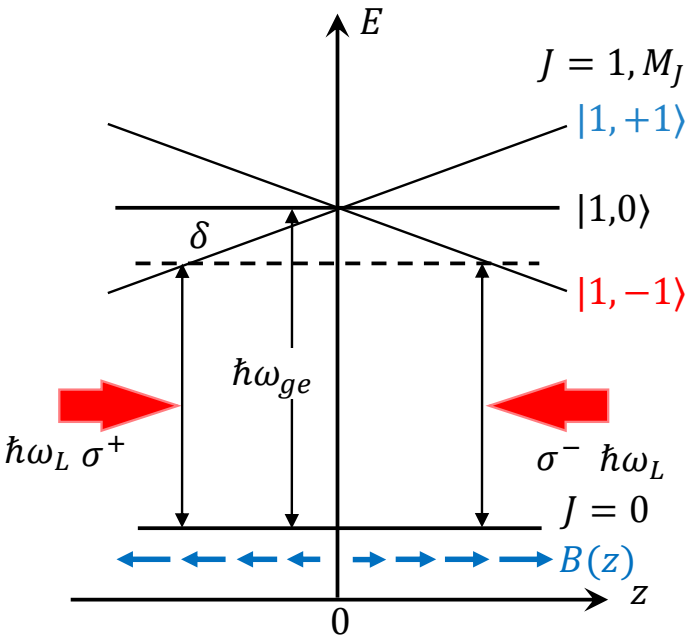

Figure 4.3: The working mechanism of the Magneto-Optical Trap in 1-D for an atom with a $J = 0 \rightarrow J' = 1$ transition. The on-resonance atomic frequency is ω_{ge}. The counter-propagating laser beams are circularly polarized and red-detuned to the atomic transition with the detuning of δ.

For simplicity, we first consider the MOT in one dimension. As illustrated in Fig. 4.3, we consider a simplified atomic model consisting of a ground state $|g\rangle$ and excited state $|e\rangle$, whose total angular momentum are $\mathbf{J}_g = 0$ and $\mathbf{J}_e = 1$. $\mathbf{J}_e = 1$ has three Zeeman sub-levels, which can be excited according to the selection rules.

As shown in Fig. 4.3, a right-hand circularly polarized laser beam (σ^+) illuminates from the left, while a left-hand circularly polarized laser beam (σ^-) illuminates from the right. These counter-propagating laser beams are tuned below the atomic transition with a detuning δ. The magnetic field breaks the degeneracy of the excited state due to the Zeeman effect: the excited state $M_e = +1$ is shifted up for $B > 0$ and down for $B < 0$ whereas the state $M_e = -1$ is shifted oppositely.

According to the selection rules [95, 110], the σ^+ light only excites the atom to the $M_e = +1$ state and the σ^- light only excites the atom to the $M_e = -1$ state. When the atom moves to the right side, the Zeeman effect will cause σ^- light to be closer to the atomic transition. Hence the atom will scatter more photons from the σ^- light than from the σ^+ light. This leads to a net force pointing towards the center of the trap. Similarly, when the atom moves to the left, σ^+ light will scatter more photons and push atoms towards the center.

Extending the 1-D situation (see Fig. 4.3) to 3-D by using six laser beams can trap the atoms in the center of the coil pair. Additionally, the trapping mechanism works for any $\mathbf{J}_g \rightarrow \mathbf{J}_e = \mathbf{J}_g + 1$ transition.

4.3 Sub-Doppler laser cooling

In 1988, Lett and co-workers carefully measured the temperature of the atomic cloud, which was much lower than the Doppler temperature T_{Dopp} [113]. This led to the study of the sub-Doppler laser cooling mechanism. Two groups, Jean Dalibard and Claude Cohen-Tannoudji [112] and Ungar and co-workers [114], developed a model that is a combination of the multilevel atomic structure, polarization gradients, light shifts and optical pumping. This resulted in that the Nobel Prize in Physics 1997 was awarded to Steven Chu, Claude Cohen-Tannoudji and William D. Phillips jointly "for development of methods to cool and trap atoms with laser light" [14]. This section will use the method in Ref. [110, 112] to explain the sub-Doppler cooling mechanism.

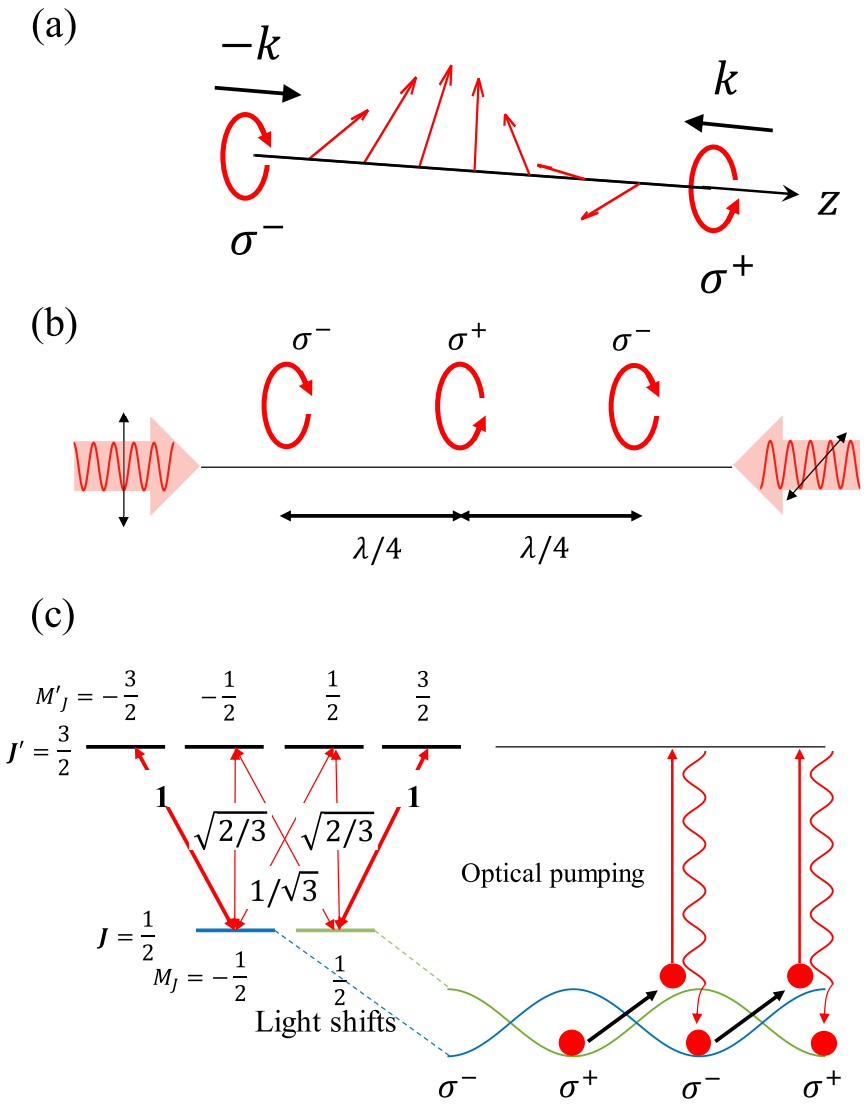

Figure 4.4: The working mechanism of the polarization gradient cooling. (a) The polarization gradient field for the σ^+-σ^- configuration. (b) The polarization gradient field for the lin⊥lin configuration. (c) The atomic level diagram and light shifts for the $J_g = 1/2 \leftrightarrow J_e = 3/2$ transition.

To make the MOT work, we counter-propagate two laser light beams with a σ^+-σ^- polarization configuration along the z direction (see Fig. 4.3). This leads the total electric

field $\boldsymbol{E}$ to have the form:

$$\begin{aligned}\boldsymbol{E} &= E_0\left[\hat{x}\cos(\omega_L t - k_L z) + \hat{y}\sin(\omega_L t - k_L z)\right] \\ &\quad + E_0\left[\hat{x}\cos(\omega_L t + k_L z) - \hat{y}\sin(\omega_L t + k_L z)\right] \\ &= 2E_0\cos(\omega_L t)\left[\hat{x}\cos(k_L z) - \hat{y}\sin(k_L z)\right],\end{aligned} \tag{4.6}$$

where $\hat{x}$ and $\hat{y}$ are the unit vector along the x and y axes. Equation 4.6 indicates that the resulting light field is linearly polarized whose polarization vector is fixed in time but rotates along the z-axis [shown in Fig. 4.4(a)]. In the 3-D MOT system, three orthogonal such light pairs interfere and give rise to a spatially varying polarization pattern. It can be simulated by using counter-propagating laser beams with a lin$\perp$lin polarization configuration as shown in Fig. 4.4(b). The light polarization changes from the right-hand ($\sigma+$) to left-hand circularly polarized ($\sigma-$) light over a distance of a quarter wavelength.

As illustrated in Fig. 4.4(c), we consider the simplest atomic model with a transition structure of $J_g = 1/2 \leftrightarrow J_e = 3/2$ in the light field shown in Fig. 4.4(b). When the atom see the $\sigma+$ light, it will be rapidly optically pumped to the $M_g = 1/2$ sub-level. According to the selection rules, the absorption will always lead to $\Delta M = 1$, while the spontaneous emissions result in $\Delta M = 0, \pm 1$. The atoms will therefore tend to build up the population in the $M_g = 1/2$ sub-level rather than $M_g = -1/2$ sub-level. Contrarily, when the atom see the $\sigma-$ light, it will accumulate in the $M_g = -1/2$ sub-level.

When driving the atomic transitions, the presence of the light field will also cause the shift of the atomic energy levels due to the Stark effect [95, 110]. The strength of these shifts depends on the Clebsch-Gordan coefficients. As shown in Fig. 4.4(c), the $M_g = 1/2$ (or $M_g = -1/2$) sub-level shows valleys (or hills) at pure $\sigma+$ light and hills (or valleys) at pure $\sigma-$ light. When traveling in such light field, the atom loses energy by climbing up the hills. Once the atom reaches the hill, it will be transferred to the $M_g = -1/2$ sub-level through the optical pumping and simultaneously shifted to the bottom of the potential. It will then climb the hill again and again, during which process the atom loses its energy and be cooled. This is the famous cooling mechanism called "Sisyphus cooling" [14, 110].

Typical sub-Doppler temperatures are around few micro-Kelvin for ^{85}Rb atoms.

Chapter 5

Experiments

This thesis has so far theoretically demonstrated the survival resonance and outlined the scenario of how to use the laser to cool atoms in Chapters 3 and 4, respectively. This chapter will describe how to implement these in practice. It will initially outline the experimental timing, and then describe the apparatus based on the sequence in chronological order.

5.1 Experimental sequence and computer control

This section will describe the experimental sequence and how to realize it via computer control.

5.1.1 Experimental sequence

Figure 5.1 outlines the three stages of the time sequence for one typical experimental run. We first laser cool and prepare the atoms in a specific atomic internal state (Stage-1); then expose them to a series of standing-wave light pulses (Stage-2); and finally measure the atomic survival through a normalized state detection (Stage-3).

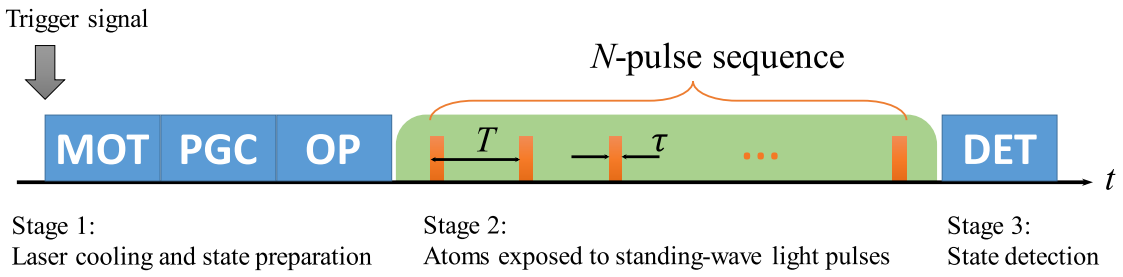

Figure 5.1: The time line for one typical experimental run (not to scale). Acronyms: MOT magneto-optical trap, PGC polarization gradient cooling, OP optically pumping, DET state detection. T is the pulse period and τ is the pulse duration. Experiments get triggered when the MOT is fully loaded.

A. Stage-1: Laser cooling and state preparation

As shown in Fig. 5.1, each experimental cycle starts by loading a cloud of ^{85}Rb atoms in the MOT, where the cooling and repump lights and the quadrupole coils are simultaneously on. Once the MOT is fully loaded, the sequence is trigged. By increasing the detuning while reducing the optical power of the cooling beam and simultaneously switching off the quadrupole magnetic field, we cool the atoms to 5 μK by PGC (see Section 4.3). We then prepare the atoms in a specific internal state. Section 5.2 provides the detailed description of the setup and parameters.

B. Stage-2: Exposure to a standing-wave pulse sequence

Immediately after the Stage-1, we turn off the cooling and repump lights and expose the atoms to a standing-wave pulse sequence. The period of the N-pulse train is T, and the duration for each pulse is τ, where τ is sufficiently short so that it fulfills the Raman-Nath condition. When the F = 3 ground state is the initial state (see Fig. 2.2), there will be dark states in this manifold [91, 92]. We apply a bias magnetic field perpendicular to the propagation and polarization directions of the light to quench these dark states. Section 5.3 describes in detail how to create a standing wave with a high spatial stability

and good contrast between the nodes and anti-nodes of it (see Eq. 2.3). Additionally, it describes how to suppress stray light during the experiment.

C. Stage-3: Detection – data acquisition and analysis

After Stage-2, we measure the atoms remaining in their initial state by using a photomultiplier tube to collect the fluorescence signal while exciting them on the closed $F = 3$ to $F' = 4$ transition. To reduce the affect of atom number fluctuation, we apply a normalized internal state detection sequence to read out the atom number in the initial and dark state separately. This sequence varies when different ground state is chosen to be the initial state. Section 5.4 in detail describes how the data acquisition and analysis work.

5.1.2 Computer control

To realize the sequence shown in Fig. 5.1, the system requires a time precision at the level of 10^{-9}. To achieve this, we use a National Instrument (NI) PCI-6733 high-speed analogue input/output (I/O) card [115] in combination with an Agilent-33250A arbitrary function generator to control the equipment.

We use the LabVIEW interface to program the PCI-6733 card and execute the MATLAB scripts to generate the analogue and transistor-transistor logic (TTL) signals, and read the signals from the oscilloscope. The LabVIEW program is developed by Simon, which is described in detail in Ref. [116].

5.2 Experimental apparatus

In general, generating cold atoms is well established in Refs. [96, 110, 117]. This section gives a brief description of the cold-atom apparatus in our lab. It includes the vacuum system, quadrupole magnetic field, compensation magnetic field, atomic source, and laser system.

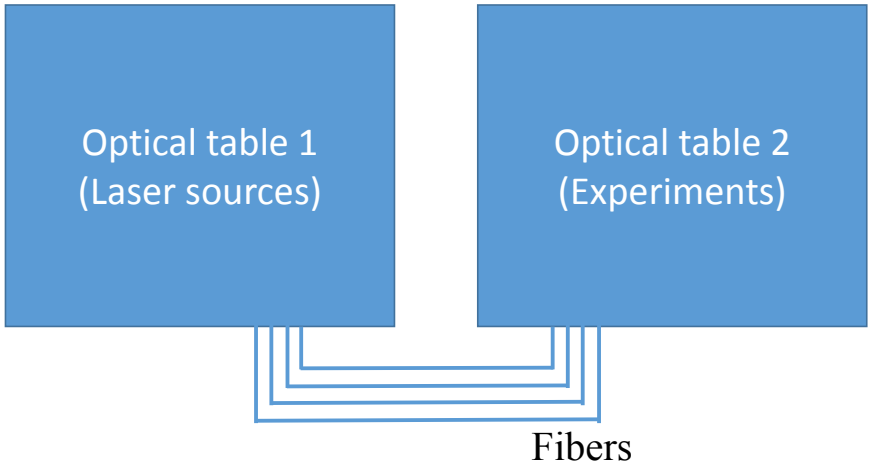

Figure 5.2: The diagram of the experimental arrangement.

As illustrated in the Fig. 5.2, we construct the apparatus on two pneumatically-supported optical tables. One is for the light sources, where we prepare all laser light used for manipulating atoms. The other is supporting the vacuum system, where the experiments take place. We deliver light from optical table 1 to 2 through fibers shown as blue lines.

5.2.1 Vacuum system

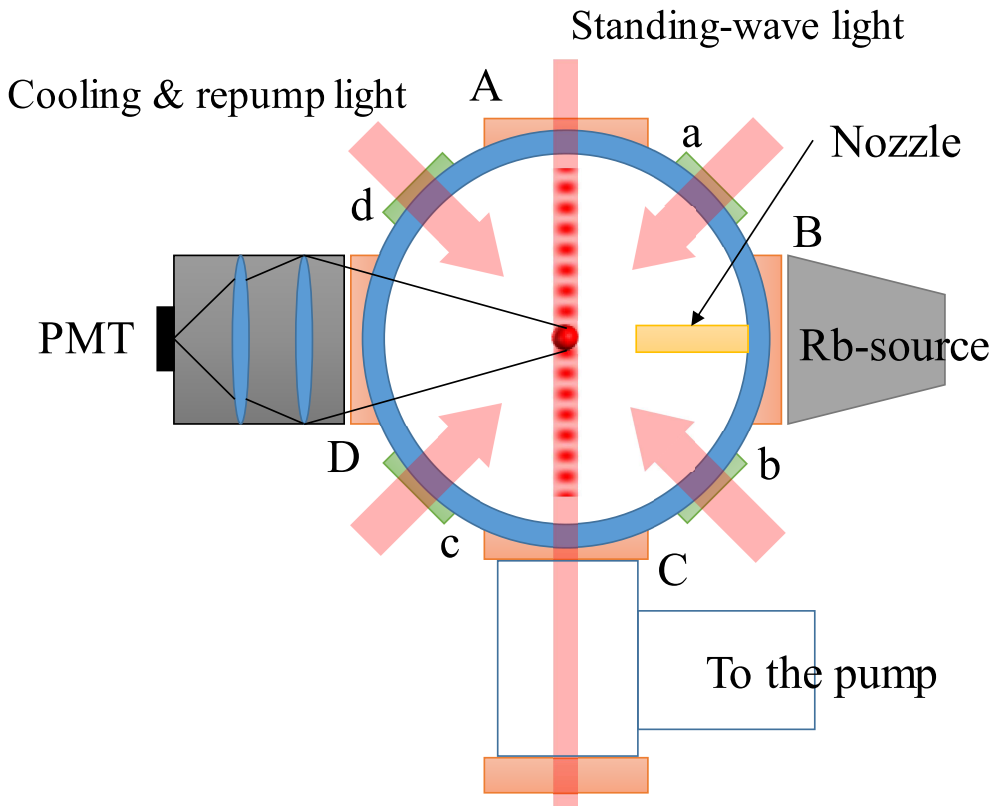

Figure 5.3: Schematic diagram of the main vacuum chamber and its accessories.

The vacuum chamber in our lab has a background vapor pressure of less than 2×10^{-11} Torr. Figure 5.3 shows the schematic diagram of the main chamber and essential accessories surrounding it.

The main chamber has two standard 8-inch ConFlat (CF) flanges [118] that are fitted with view-ports having a clear aperture of approximately 15 cm. It also has four 4.5-inch CF flanges labeled as A, B, C and D in Fig. 5.3. Two of them are used for mounting the atomic beam source, connecting the ion pump and Titanium sublimation pump through a tee. The remaining two flanges are fitted with view-ports for collecting fluorescence signal from the atoms and feeding through the vertical standing-wave light beam, respectively.

Additionally, it has four 2.75-inch CF flanges (marked as a, b, c and d in Fig. 5.3) that are fitted with view-ports having a clear aperture of 4 cm. These view-ports allow for feeding cooling and repump light beams into the chamber. The detailed description can be found in the Ref. [86].

5.2.2 Quadrupole magnetic coils

During the MOT stage, the quadrupole magnetic coils clamped around the two 8-inch CF flanges in Fig. 5.3 are powered by a programmable Agilent-6553A DC power supply. It supplies 5.4 A through the coils that creates a magnetic field gradient of 6.8 G/cm along the axial-axis and 2.9 G/cm along radial-axis. The power dissipated in the coils is 45 W and is air cooled [86].

5.2.3 Compensation magnetic coils

In the experiment, we use three bias coil-pairs to compensate the background magnetic field at the center of the vacuum chamber. The possible sources for the unwanted background magnetic field include the earth's magnetic field, the stray magnetic field from the ion pump and other surrounding electronics. We use three Agilent-E3615 DC power supplies to power these coils.

We adjust the current through the compensation coils to minimize the temperature of the atomic cloud after PGC (see Section 4.3). Unlike the quadrupole coils, the bias coils are continuously on during the experiments. Additionally, these three coil-pairs are larger, which provides better homogeneity in the central part of the chamber.

5.2.4 Atomic source

In the experiment, we use an atom dispenser (SAES alkali metal dispenser) as the atom source [119, 120]. It emits natural Rubidium of which only the ^{85}Rb will be laser cooled and trapped in the MOT. As shown in Fig. 5.3, we use a nozzle to collimate the atomic

beam by removing high speed atoms transversely.

The dispenser emits atoms once its temperature exceeds the critical temperature. To release the atoms, we heat it by running electric current through it from an programmable Agilent-6553A DC power supply. We can also modulate the atomic flux by adjusting the current through the dispenser. Additionally, we use thick feed-through to connect the dispenser to the power supply, which can conduct the heat at a high rate. The flux of atoms therefore drops rapidly once we shut off the current.

5.2.5 Laser system

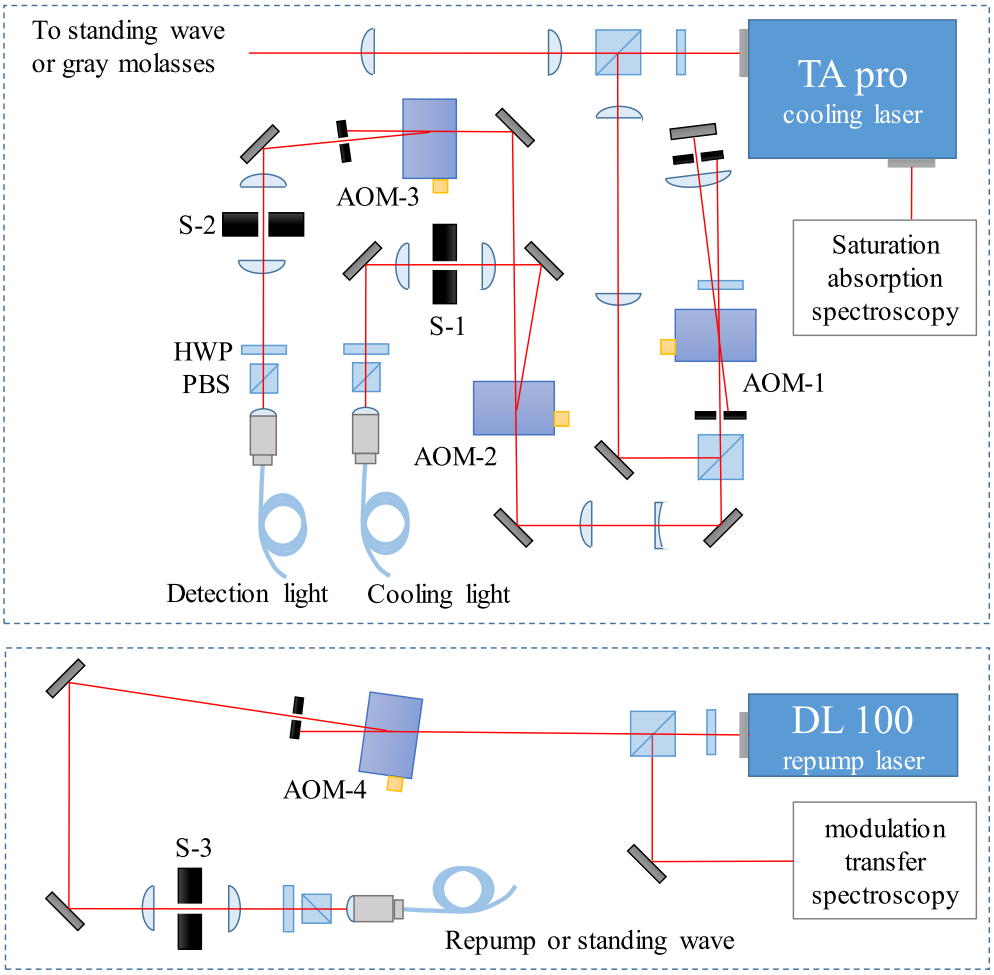

Figure 5.4: The schematic diagram of laser sources and frequency and amplitude control. Acronyms: S-1,2,3 the mechanical shutters, HWP half-wave-plate, PBS polarization beam splitter, AOM-1,2,3,4 acoustic-optical modulators.

To conduct the experiment, we need several different laser frequencies as indicated in Fig. 2.2. They are the cooling, sub-Doppler cooling (bright and gray molasses), repump, detection and standing-wave light. Figure 5.4 shows the schematic diagram of the laser system, where all the optical elements are on the optical table 1 (in Fig. 5.2). In the experiment, we use the acoustic-optical modulators (AOM-1, 2, 3 and 4) to control the

lights' intensities and their frequencies via the amplitude and frequency modulation. The cooling, sub-Doppler cooling and detection are from the same laser (Toptica: TA pro) that we in the following deem the "cooling laser". The repump light is from a separate laser (Toptica: DL100). The cooling laser light is locked to the F = 3 to F$'$ = 3, 4 crossover transition through the frequency modulated saturation absorption spectroscopy [96, 121]. While, the repump light is locked to the F = 2 to F$'$ = 2, 3 crossover transition through the modulation transfer spectroscopy [122].

When loading atoms during the MOT-stage in Fig. 5.1, the cooling light is tuned 17 MHz below the atomic transition from F = 3 to F$'$ = 4, and the light intensity of each beam is slightly above the saturation intensity $I_{\text{sat}} = 1.669$ mW/cm^2. The beam is expanded to have a beam diameter of 3 cm to increase the loading rate. The repump light is on-resonance of F = 2 to F$'$ = 3 transition (see Fig. 2.2) and with an intensity of 1 mW/cm^2. The repump light overlaps with one of three cooling beam pairs.

During the PGC process, the bright molasses cooling light is 37 MHz below the transition from F= 3 to F$'$ = 4. We achieve it by shifting the frequency of the driving radio-frequency (RF) for AOM-1. Additionally, we can also use gray molasses to perform sub-Doppler cooling [123–125]. In this case, we use the light labeled "To standing wave or gray molasses" in Fig. 5.4, and tune its frequency 25 MHz above the F = 3 to F$'$ = 3 transition on the D-2 line. We then couple the light to the same fiber that delivers cooling light. The optical molasses cooling light has only 1/3 of intensity during the MOT stage.

In addition to cool the atoms, the cooling and repump light are versatile. They individually act as state preparation and standing-wave light depending on which state is the initial state. For example in Chapters 6 and 8, when the F = 3 state is the initial state, the repump beam will be switched off 300 μs later than the cooling beam after PGC. In this manner, the repump light will effectively transfer all the atoms to the F = 3 state. The standing wave is derived from the cooling laser since it is near-resonant to the transition from F = 3 to the excited states. Contrarily, when the F = 2 state is the initial state

(for example in Chapter 7), the standing wave light is derived from the repump laser. Meanwhile, the sub-Doppler cooling light is the state preparation light.

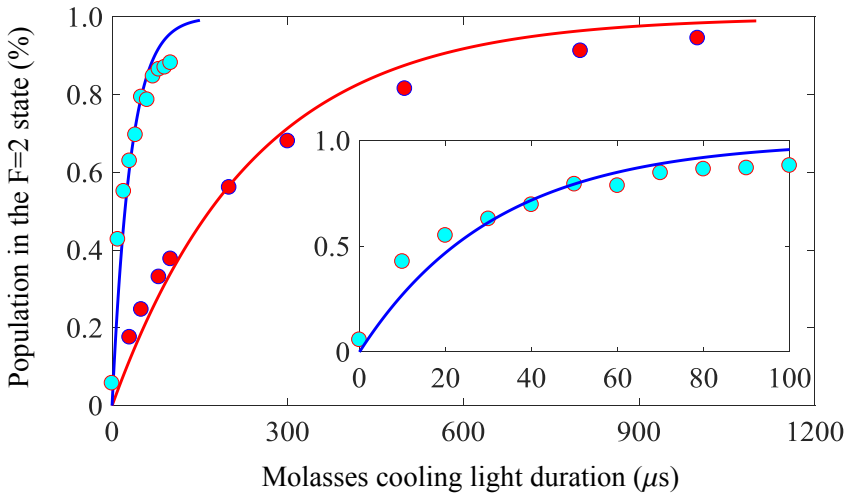

Figure 5.5: Measured (circles) normalized atomic population in the F = 2 ground state as a function of the molasses cooling light duration. The red (light blue) circles are the measurements using bright (gray) molasses cooling light. The inset is the magnified figure for the gray molasses.

To characterize the efficiency of transferring atoms from the F = 3 state to the F = 2 state by using bright and gray molasses cooling light, we initiate atoms in the F = 3 state and expose them to such cooling lights. Figure 5.5 displays the proportion of atoms that get transferred to the F = 2 state after a certain duration. The red (light blue) circles are the measurement using bright (gray) molasses, and the lines are the fitting curves:

$$f(x) = 1 - \exp(-\lambda x), \tag{5.1}$$

where the fitting parameter λ is the decay rate that is 4.2 (32) kHz for bright (gray) molasses light. We see the gray molasses optically pumps the atoms to the F = 2 state about 8 times faster than using bright molasses. This is because the atoms predominately scatter light from a closed-transition when using bright molasses light, while from an open-transition for gray molasses light. When the rapid transfer of the atoms to the F = 2 state is required in the experiment, we therefore use the gray molasses.

After the preparation of light sources, we use optical fibers to deliver stable beams with a nice Gaussian profile over significant propagation distances (see Fig. 5.2). Particularly, we use single mode polarization maintaining fibers (PM-fiber, Thorlabs: P3-780PM-FC). The core of a PM-fiber is birefringent and therefore has a fast and a slow polarization axis. By carefully matching the polarization of the linearly polarized incoming laser beam parallel to one of these axes, the output light remains linearly polarized. A half-wave plate (HWP) in combination with a polarization beam splitter (PBS) is used to adjust the polarization and optical power of the incoming laser (see Fig. 5.4). In practice, even though the fiber is supposedly polarization maintaining, mechanical vibration and thermal variation cause slight polarization pollution. To suppress this contamination, we lay the fibers inside a polyvinyl chloride (PVC) pipe to isolate them from the environment.

5.3 The implementation of the optical standing-wave pulse train

We now enter into the second stage of the experiment, when the atoms are exposed to the standing-wave light pulses. I would like to devote a whole section to describe the standing wave since it significantly impacts all results in the thesis. The present section will outline how to achieve high spatial stability and a good contrast standing wave (see Section 2.1). It will begin with the light pulse generation, and then give two standing-wave configurations. Subsequently, this section will describe how to calibrate the standing-wave light frequency and to check its quality.

5.3.1 Light pulse generation

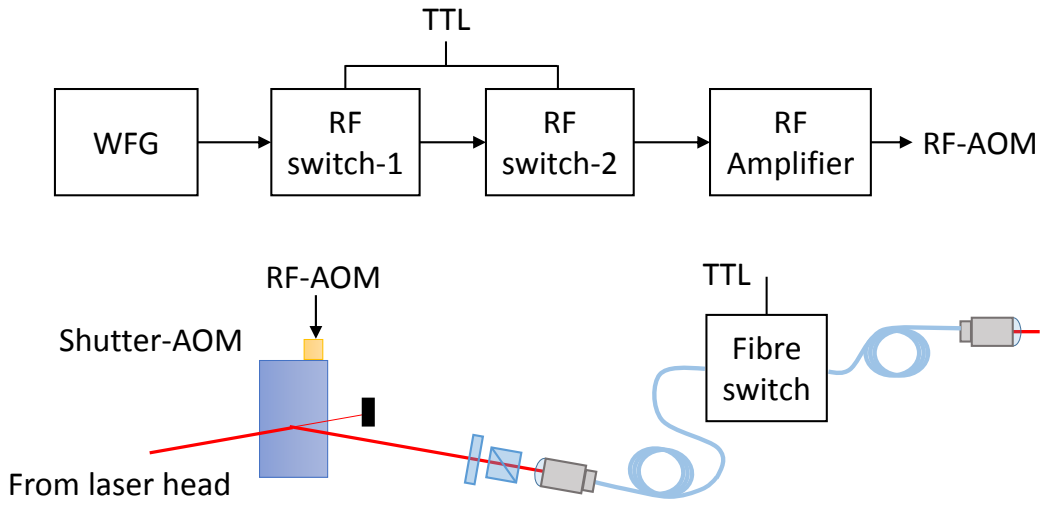

Figure 5.6: The standing-wave light pulse generation. Top: the generation of the RF-signal for driving the AOM; bottom: the light suppression through the AOM and fiber switch. WFG: wave-function generator (Stanford Research Systems: model SG382); RF: radio-frequency.

Immediately after the state preparation, we switch off the cooling and repump light by blocking them with mechanical shutters (shown in Fig. 5.4). We then expose the atoms to a standing-wave light pulse sequence shown in Fig. 5.1. To realize the pulse train, we use an AOM (Brimrose: TEM-200-13-.780) in combination with a fiber switch (Agiltron: NS 300 KHz) to turn on and off the light (see Fig. 5.6).

AOM cannot turn the light off when there has RF power leaking through it. To eliminate the leakage light through the AOM, we use two serially connected high extinction ratio RF-switches (Mini-Circuits: ZASWA-2-50DR+) to switch off the driving RF power (see Fig. 5.6). This leads to an attenuation of 164 dB to the RF-power. Additionally, the contamination of the optical surfaces (for example the surface roughness when dust burns on them) will lead light to scatter in random directions. The scattered light can

accidentally couple into the fiber, which can not be shifted off by AOMs. We therefore need a separate mean to reduce this light. In the experiment, we use a fiber switch with 20 dB attenuation to further suppress the leakage. The combination of AOM and fiber switch results in a non-detectable optical power when the TTL is at low-level.

5.3.2 Arrangements of the Standing-wave light beam

This sub-section provides two configurations of how to arrange the standing wave. One is a horizontally arranged stationary standing wave (see Eq. 2.4); the other is a vertically aligned accelerating standing wave that accelerates along the gravitational axis (see Eq. 2.8).

A. Horizontally arranged stationary standing wave

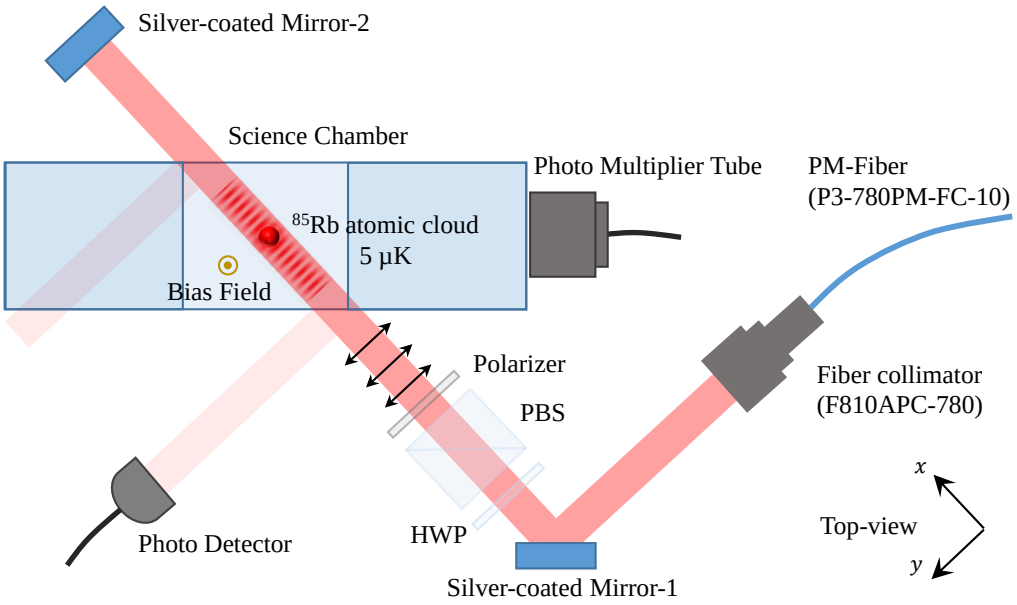

Figure 5.7: The top view of the standing-wave beam configuration in the horizontal plane (not to the scale). The standing wave is propagating along the x-axis. HWP is the half-wave-plate and PBS stands for polarization-beam-splitter (Thorlabs: PBS252). The polarizer is a high-extinction ratio one (Thorlabs: LPVIS100-MP2). The standing-wave beam propagates to a vacuum chamber with an angle of $\sim 45°$ to avoid the reflection light overlap with the injection light. A photo-multiplier-tube locating 20 cm away from the center of the chamber collects the signal from the atomic ensemble.

We first demonstrate how to construct a stationary standing wave in the horizontal plane (x-y plane) (see Fig. 5.7). Continue from the output of the fiber switch in Fig. 5.6, a 10-meter PM-fiber delivers the light from the laser table to the front of the vacuum chamber. We use the fiber collimator (Thorlabs: F810APC-780) to shape the light beam to have a Gaussian profile with a diameter ($1/e^2$) of 7.5 mm. This is sufficiently large to cover the atomic cloud that is typically 1 mm in our lab, which allows us to ignore the transverse profile of the light beam (see Eq. 2.1). The silver-coated mirror-1 (M-1) directs the light beam towards the atoms in the center of the vacuum chamber. We then retro-reflect the

light beam by carefully tuning mirror-2 (M-2) to couple the light back to the fiber. A high back-coupling efficiency indicates good collimation of the light beam and a counter-propagating geometry between the two waves. It is thereby a criterion for checking the quality of the standing wave.

As discussed before, when the F = 3 state is the initial state, there are dark states in this manifold, which will not interact with the standing-wave light. To quench these dark states, we use polarizers to ensure that the laser polarization (black arrows) is perpendicular to the bias magnetic field (shown as the yellow dot arrow perpendicular to x-y plane).

An essential feature in Fig. 5.7 is that the standing-wave light beam has an angle of $\sim 45^\circ$ with respect to the view-port's surface. This is to avoid the reflected light (due to the view-ports) to overlap with the standing wave, which would lead to interference patterns. Additionally, the reflection from the front view-port is picked up by a photo detector and used to monitor the power fluctuation during the experiments.

B. Vertically arranged accelerating standing wave

To measure the local gravitational field, we need to align the standing-wave light beam vertically and be able to accelerate it to match the gravitational acceleration. Recall Eq. 2.8 in Chapter 2, the standing-wave interference pattern accelerates when the frequency difference between the two light beams is linearly swept. This means that to precisely control the standing wave acceleration, we need to counter-propagate two light waves that have a well defined frequency difference between them. This part describes how to construct a vertical standing wave that can accelerate with a controllable rate.

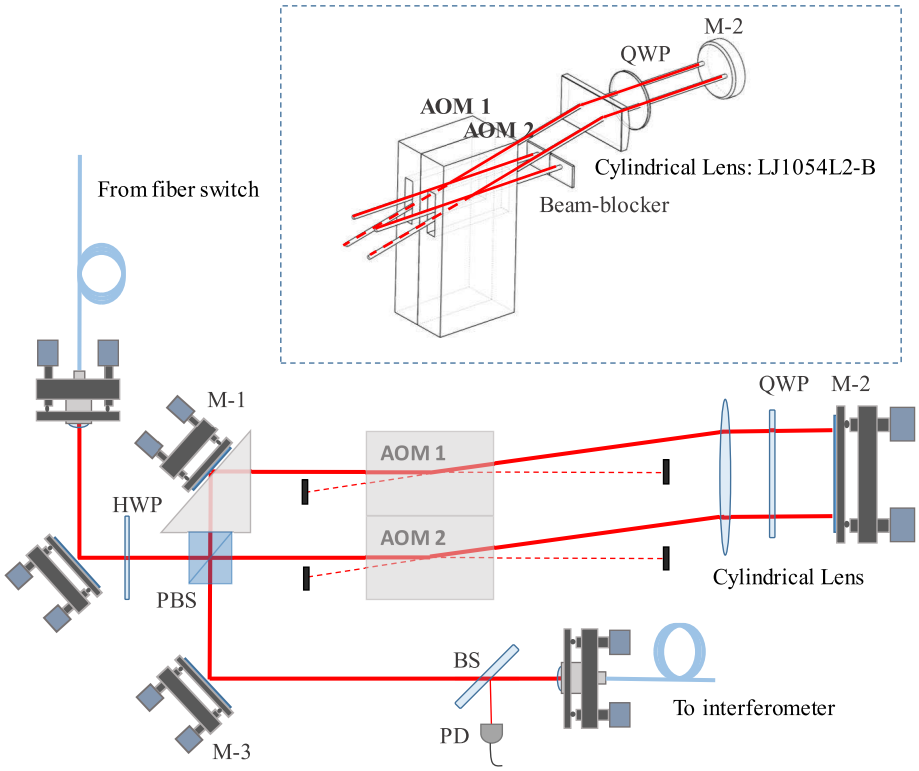

Figure 5.8: The frequency control between the two laser beams. HWP: half-wave-plate; PBS: polarization beam splitter; M-1,2,3: sliver coated mirrors; QWP: quarter-wave-plate; Interferometry fiber: 10-meter polarization-maintaining fiber (PM-fiber) (Thorlabs: P3-780PM-FC-10); BS: beam-splitter (transmission-reflection ratio 90/10); PD: photon detector. Light with different frequencies ω_1 and ω_2 are coupled through two orthogonal polarization axes through the interferometry fiber. The figure inside dashed-line block is a 3-D diagram showing the layout of the AOMs.

To suppress the relative phase noise between the two light waves are crucial, since there are two waves involved. We overcome this problem by deriving them from the same laser beam, letting them to share the same optics as much as they can, and minimizing the uncommon optical path between them. The following part will use the diagram shown in Fig. 5.8 to explain the method for generating two frequency controllable light waves at a low relative phase noise level.

This paragraph describes how to generate two light beams with tunable frequencies.

The left-top fiber labeled “From the fiber switch” (in Fig. 5.8) connects to the output of the fiber switch (in Fig. 5.6). We split the laser beam into two arms using the PBS. Rotating the half-wave plate (HWP) changes the polarization of the incoming beam, and therefore can adjust the intensity ratio between the two output light beams after the PBS. We frequency modulate the two beams by double passing them through two AOMs. This ensures the alignment of the laser beams to the output fiber (labeled as “To interferometer”) to maintain when sweeping the driving RF frequencies. Double passing through the quarter-wave plate (QWP) flips the polarizations of the beams with 90°, which ensures the diffracted light beams are coupled out through the PBS. The output of these two light components has different frequencies (if the driving RF frequencies of the two AOMs differ) with orthogonal polarizations.

We now give the method to achieve a stringent rejection of the relative phase noise. As shown in Fig. 5.8, the PBS bounds with M-1 using a triangle aluminum block, meanwhile the two AOMs are jointed together. The two light beams share the same lens, quarter-wave plate and retro-mirror M-2. Furthermore, a box covering the entire optics (in Fig. 5.8) suppresses the air turbulence induced variation of the relative optical path length. Furthermore, the noise of the driving RF frequency can lead the diffracted light frequency to jitter, which means that any relative frequency noise between the two driving RF can be problematic. We suppress this noise by using Agilent-33600A double-channel wave function generator, where the two channels share the same clock with an accuracy of 0.1 ppm of the setting. After the recombination of the two light beams, we couple them into the same fiber with respect to the fast and slow axes, respectively.

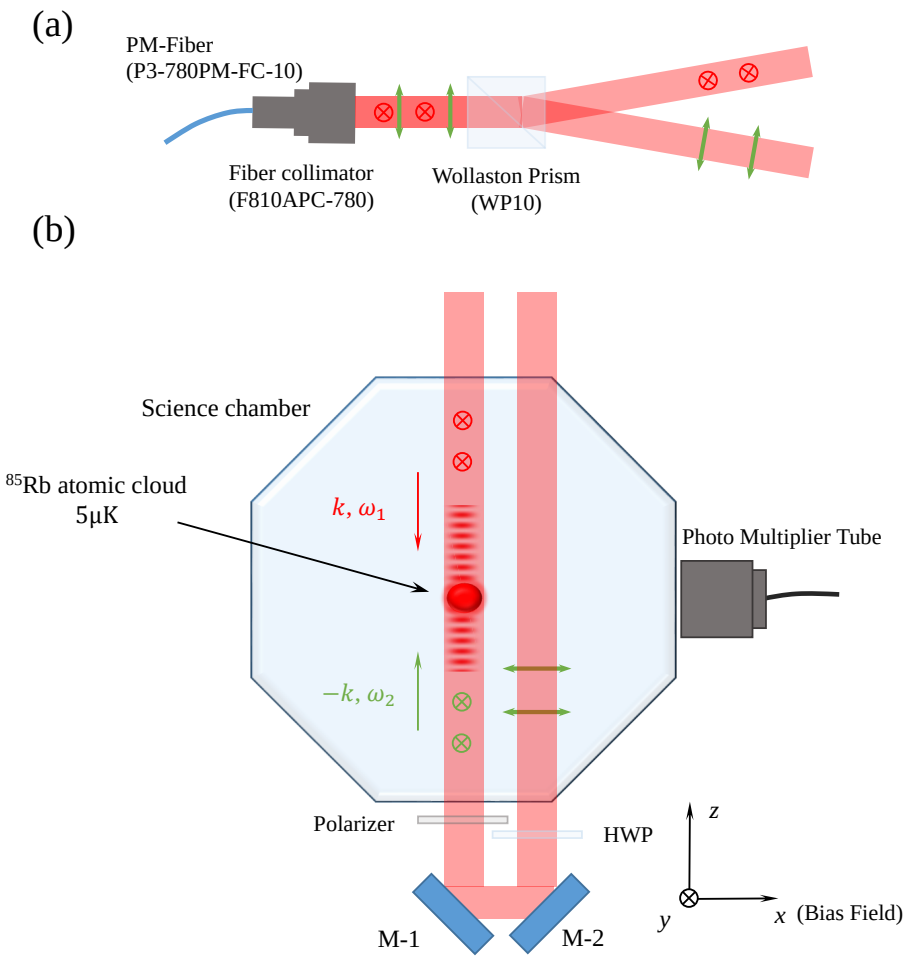

Figure 5.9: The diagram of a vertically arranged standing-wave light. (a) The splitting of the two frequencies according to their polarizations. (b) The formation of the vertical standing-wave beam.

We then demonstrate how to construct a vertically accelerating standing wave using the two tunable light beams in Fig. 5.9 . The fiber labeled "To interferometer" in Fig. 5.8 connects to the fiber collimator (F810APC-780) in Fig. 5.9(a), which collimates the output laser beam to have a Gaussian profile and a diameter of 7.5 mm ($1/e^2$). A high extinction ratio Wollaston prism then splits the light into two arms that are the two components with orthogonal polarizations and different frequencies [shown in Fig. 5.9(a)].

To form the standing wave, we need to counter-propagate the two light waves in the vacuum chamber. As shown in Fig. 5.9(b), beam 1 with frequency ω_1 and polarization along y-axis is aligned vertically and centered at the atomic ensemble. The other beam with frequency ω_2 initially propagates parallel to beam-1 and is then reflected by two mirrors (M-1 and M-2) such that it counter-propagates beam-1 at the position of atoms. Its polarization is rotated 90° by the half-wave plate (HWP) and further cleaned by a polarizer. This ensures that the two beams have the same linear polarization and therefore a high contrast interference of the standing wave. By linearly ramping the frequency difference between the two beams, the standing-wave interference pattern can move with a constant acceleration a along the vertical z-axis (see Eq. 2.8).

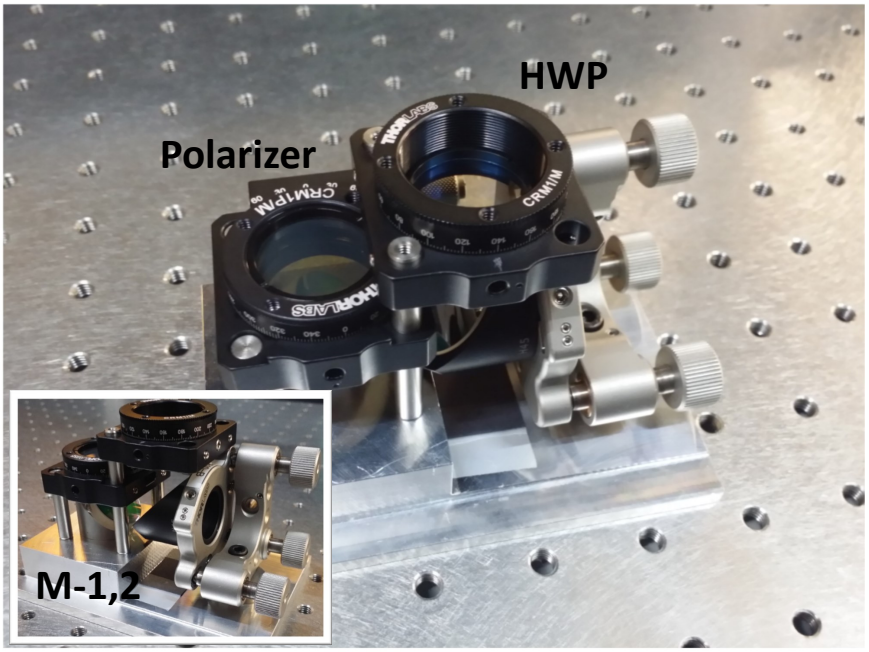

Figure 5.10: The photo of the lower part of the vertical standing-wave beam. The two mirrors are mounted on the same block of aluminum. The half-wave plate and polarizer are mounted in cage-system rotation mounts. The whole block is clapped on the optical table right below the science chamber.

Because the two light waves are separated (see Fig. 5.9), we again encounter the problem of gaining relative phase noise between the two waves. The noise is predominately from

vibrations of the lower part that reflects and overlaps the light beams [see Fig. 5.9(b)]. To suppress the vibration of this part, we bound the optical elements rigidly. There is a base-block milled from one single piece of aluminum. We directly glue M-1 on this base. M-2 is fitted in a mirror-mount to allow for adjusting beam-2 to overlap it counter-propagating with beam-1. The half-wave plate and polarizer are in a cage system to control the standing wave polarization. The whole base is then clamped on the optical table below the science chamber.

5.3.3 Standing-wave frequency

In the experiment, the lasers are frequency stabilized to a known atomic transition, but the lock point can be off by up to 1 MHz. This is not neglectable compared to the hyperfine splitting in the excited states of ^{85}Rb atoms. For near-resonance light, being of by 1 MHz can significantly change the atom-light interaction. It is therefore essential to know the standing-wave frequency significantly better than 1 MHz. To this end, we will outline how to calibrate the frequency in this sub-section.

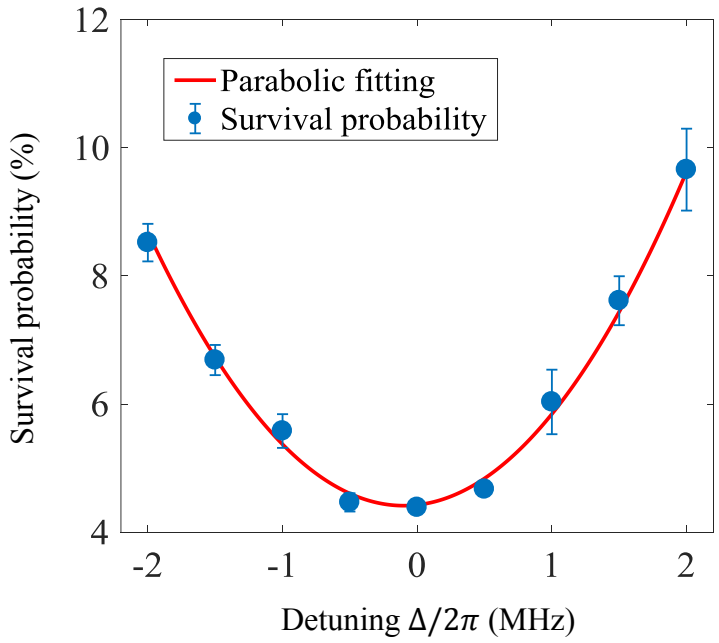

Figure 5.11: The survival probability of the atoms remaining in the F = 3 ground state as a function of the traveling-wave frequency. The blue circles are the average of 10 experimental runs and the error-bars are the standard deviation of the mean. The red line is a parabolic fit. The position of the minimum point corresponds to the on-resonance laser frequency from F = 3 to F′ = 3 transition.

To precisely determine the standing-wave light frequency, we measure the survival probability as a function of it. The atoms are exposed to a pulsed traveling-wave light with a duration of 1 μs and the optical intensity of 10 mW/cm^2.

When the F = 3 state is the initial state, we scan the standing-wave light frequency around the F = 3 to F′=3 atomic transition. The markers in Fig. 5.11 are the measured survival probability as a function of it and the line is a parabolic fit to the measurement [1]. From the fit, we can find the on-resonant frequency that corresponds to the minimum

[1]The survival probability is affected by laser light intensity, detuning and pulse duration. For suitable light intensity and duration, it is inversely proportional to the scattering rate given in Eq. 4.2, which is a function of Δ^2. We therefore use a parabolic function to fit the data in Fig. 5.11.

atomic survival. Similarly, when the F = 2 state is the desired state, the standing-wave light is derived from the repump laser. We calibrate its frequency by scanning it around the F = 2 to F′ = 3 transition (see Fig. 2.2). After we find the on-resonant frequency, it will be used as the reference to adjust the standing-wave light detuning in the experiments shown in the following Chapters.

5.3.4 Evaluation of the standing wave

We have so far demonstrated how to generate a standing-wave light and to shape it to a series of pulses. This sub-section will provide a method for evaluating the standing wave alignment.

The standing wave is essentially an optical interference pattern with the dark and bright regions interchanging along its propagation direction. When exposing the atoms to the standing-wave light beam, the atoms will survive in the vicinity of the nodes. While, the traveling-wave light beam will remove atoms to the dark state regardless their position. We can therefore evaluate the alignment of the standing wave through comparing the survival probabilities when using standing-wave and traveling-wave light. Such measurement expects a higher atomic survival for the standing wave. Furthermore, the ratio of the atomic survival between the standing wave and traveling wave indicates how dark it gets in the vicinity of the nodes, which is the contrast of the standing wave.

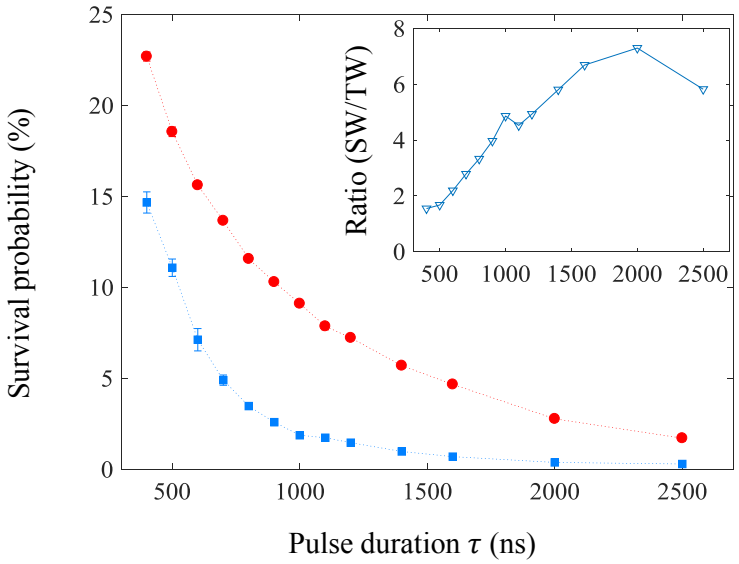

Figure 5.12: The survival probability as a function of the pulse duration τ with a single standing-wave (red circles) or traveling-wave (blue squares) laser pulse. The laser frequency is on-resonance of the F = 3 to F′ = 3 transition on the D2-line. The optical power of the traveling wave is 5 mW. The standing-wave light is formed by retro-reflecting the traveling beam. Each point is the average of 10 experimental runs and the error-bars show the standard deviation of the mean. The inset shows the ratio of the survival between the standing-wave and traveling-wave.

Figure 5.12 shows the measured survival probability as a function of the pulse duration τ, with standing wave (red circles) and traveling wave (blue squares) respectively. The atomic survival is the atoms remaining in the F = 3 ground state after one single laser pulse. It displays a monotonically decline trend for both standing-wave and traveling-wave light pulse. This is not surprising since a longer pulse causes atoms to scatter more photons and decay to the dark state. The survival probability for the standing wave is overall higher than it is for the traveling wave as expected. In the experiments, we reach a ratio of the survival probability between the standing wave and the traveling wave of more than 7, which represents a good standing-wave beam alignment.

5.4 Detection: data acquisition and analysis

After the standing-wave pulse sequence, we measure the atomic survival probability, which is the Stage-3 in Fig. 5.1. The survival probability is the fraction of the atoms that can survive the pulse sequence, which we measure with through a normalized state detection. To this end, we have to count the surviving and total atom number, and the survival probability is the ratio between the surviving number and the total number. This can avoid the shot-to-shot noise resulting from the atom number fluctuation for each experimental run.

As shown in Fig. 2.2, the detection light is on-resonant of $\mathrm{F} = 3$ to $\mathrm{F}' = 4$ atomic transition, which can therefore only interact with the atoms in the $\mathrm{F} = 3$ state. As for the optical intensity, we adjust it to the saturation intensity I_{sat} [94], where it can excite a significant fluorescence signal within a short period. The detection light beam is overlapped with one pair of the cooling light beam.

As shown in Fig. 5.3, two convex lenses are used to collect about 1.3% of the solid angle of the fluorescence from the atoms at the center of the chamber. A photo-multiplier tube (PMT) (Hamamatsu: H9858-20) detects the fluorescence signal. The output of PMT is sent to a low-noise current preamplifier (Stanford Research Systems: Model SR570) and converted to a voltage signal. This voltage signal displays on the oscilloscope (Tektronix: TDS 3054B).

This section will describe two different state detection methods, depending on which state is chosen as the initial state.

5.4.1 The F = 3 state detection

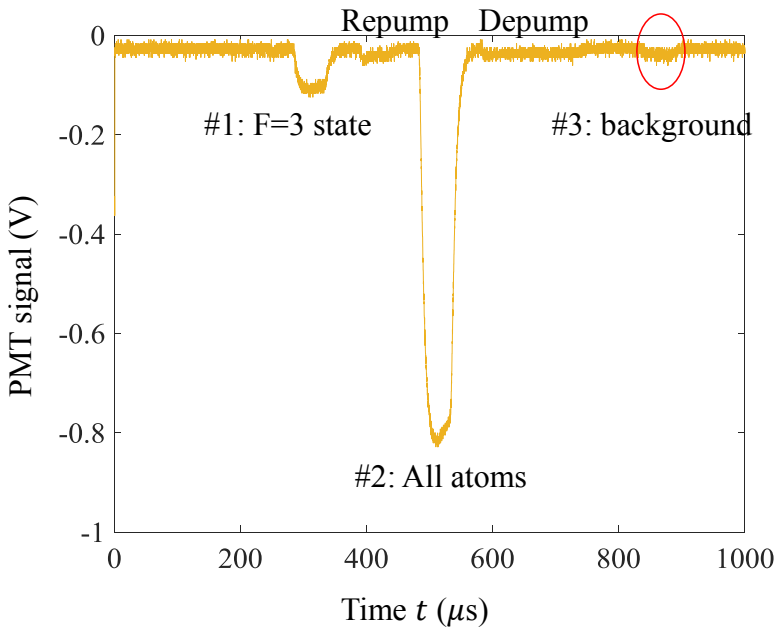

Figure 5.13: The fluorescence signal read out from the PMT during the detection stage of the experiment. The signal shown in this figure is used to measure the survival probability in the F = 3 ground state. Three peaks are: the first one is the atomic population in F = 3 ground state and the second peak is the signal for F = 2 and 3 ground states. The last peak is for the background signal. Each peak is excited through a 50 μs detection pulse that are on-resonance of the F = 3 to F$'$ = 4 closed transition on the D2-line.

When the F = 3 state is the initial state, the detection light has a standing-wave arrangement. A typical detection sequence is shown as the PMT trace in Fig. 5.13. It contains three peaks that correspond to three detection light pulses whose duration is 50 μs. The area of the first peak is the surviving atom number, denoted as $N_{\mathrm{F=3}}$. To measure the total atom number, we apply a repump light pulse for 50 μs to transfer the atoms in the F = 2 state to the F = 3 state. The second detection light pulse therefore gives the total atom number and symboled as N_{total}. To subtract the background signal that could arise from the background vapor scattered light, we apply the third detection light pulse

to record the background signal (N_{bg}). Before this, we optically pump the atoms to the F = 2 dark state by using a 150 μs-long standing-wave pulse. The survival probability of atoms remaining in the F = 3 state is then given by:

$$\mathbb{P}_{\mathrm{F=3}} = \frac{N_{\mathrm{F=3}} - N_{\mathrm{bg}}}{N_{\mathrm{total}} - N_{\mathrm{bg}}}. \tag{5.2}$$

5.4.2 The F = 2 state detection

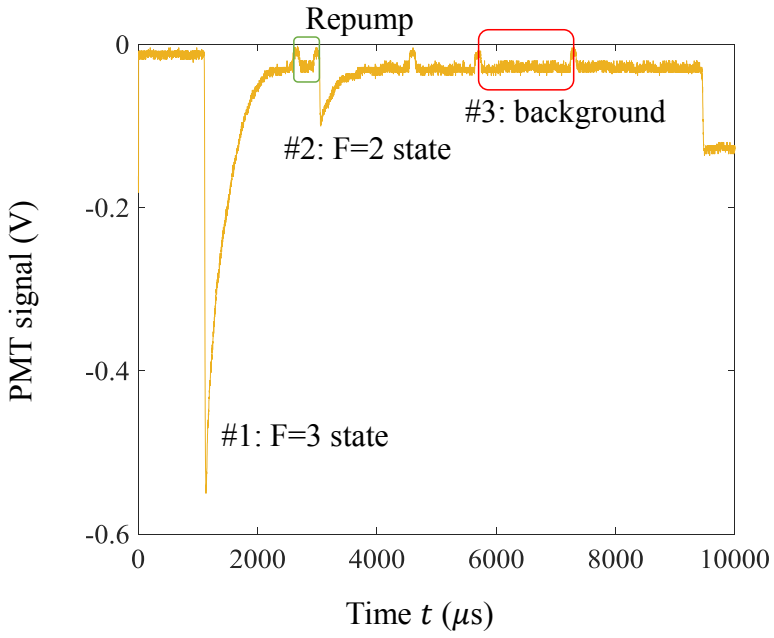

Figure 5.14: The detection sequence for measuring the survival probability of the atoms in the F = 2 ground state. The trace is the signal from the PMT. Three peaks of the florescence signals are recorded, the first of which is the atomic population in F = 3 ground state and the second is the signal for F = 2 ground state. The last peak is for the background.

We now study how to measure the survival probability when the F = 2 state is the initial state. Contrary to the detection method discussed above, we expose the atoms to a circularly polarized detection light beam with a traveling wave arrangement. A 1.5 ms detection light pulse can simultaneously excite and push the atoms in the F = 3 state out of the detection region, while keeping the atoms in the F = 2 state unchanged. Repumping

the atoms left behind in the F = 2 state to the F = 3 state and applying a second detection pulse allows us to subsequently count the number of atoms in the F = 2 state. We can therefore measure the atom number of the F = 2 and F = 3 state separately.

As Fig. 5.14 shows, we apply three detection light pulses. The area of the first peak denotes the atom number in the F = 3 state, which is labeled as $N_{\mathrm{F}=3}$. We then apply a repump light pulse to optically pump the atoms in the F = 2 state to the F = 3 state. The second peak therefore represents the atoms that survive the standing-wave pulse sequence and is denoted as $N_{\mathrm{F}=2}$. The third peak represents the background signal N_{bg}. The survival probability in F = 2 state $\mathbb{P}_{\mathrm{F}=2}$ is given by:

$$\mathbb{P}_{\mathrm{F}=2} = \frac{N_{\mathrm{F}=2} - N_{\mathrm{bg}}}{N_{\mathrm{F}=2} + N_{\mathrm{F}=3} - 2N_{\mathrm{bg}}}. \tag{5.3}$$

We can therefore measure the survival probability of the atoms using Eqs. 5.2 and 5.3 depending on which state is the initial state. Furthermore, to suppress the random noise, each measurement is the average over a number of experimental runs, with the error-bar showing the standard deviation of the mean.

Part II

Results and Discussion

Chapter 6

The survival resonances

We have so far studied the survival resonances theoretically in Chapter 3 and presented the experimental apparatus in Chapter 5. This chapter will experimentally investigate the resonance phenomenon by exposing atoms to a sequence of near-resonant standing-wave light pulses. The work presented here is extensively based on the paper [50].

This chapter begins with the measurements and calculations of the atomic survival probability as a function of the pulse period. Subsequently, it describes the micro-lensing effect arising from the phase modulation on the atomic wave function. The four-level model given in Chapters 2 and 3 agrees well with the experiments. Additionally, the resonance peaks' width shows a sub-Fourier behavior with an increasing number of pulses. The last section provides conclusions.

6.1 Survival resonances effectively without the gravitational field

This chapter studies the system in the absence of the local gravitational field. We can realize this configuration by using a horizontal standing wave (see Fig. 5.7), or using a vertical standing-wave arrangement (see Fig. 5.9) and setting $a = g$, where a is the

acceleration of the standing wave and g is the local gravitational acceleration (see Eq. 3.23).

Here, I will give the generic experimental parameters used in the present chapter, and give the varied ones in the figures' captions. We use ^{85}Rb atoms and their F = 3 hyperfine ground state as the initial ground state and F = 2 hyperfine ground state as the dark state. The standing-wave light frequency is 10 MHz red detuned to the open atomic transitions from the F = 3 state to the F$'$ = 3 state. The pulse number is $N = 7$, and pulse duration is $\tau = 300$ ns. The intensity of the light is 30 mW/cm^2.

6.1.1 Resonant pulse periods

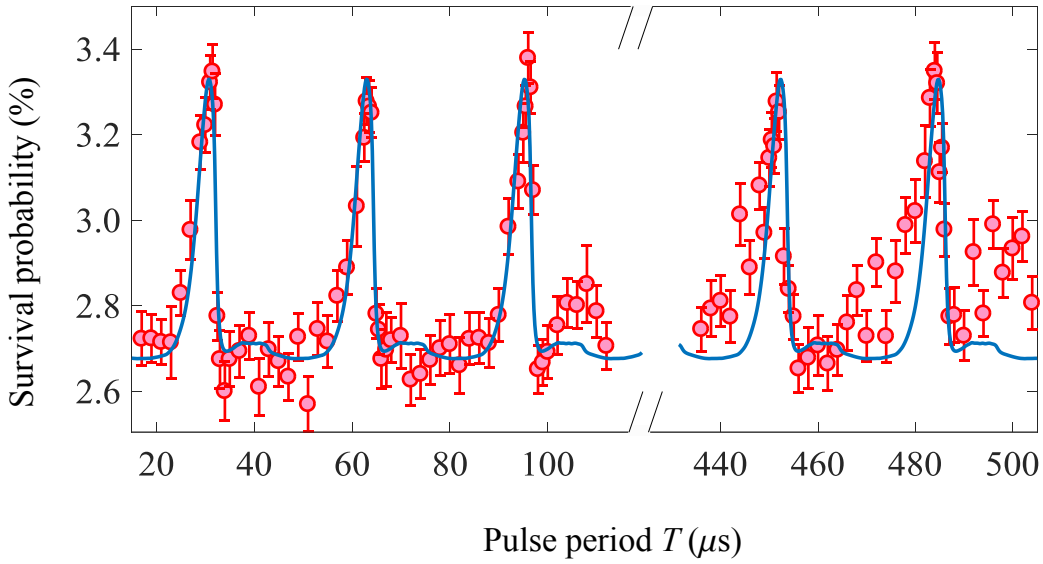

Figure 6.1: The survival probability as a function of the pulse period T. The standing-wave light is formed by retro-reflecting a horizontal laser beam. The red circles with error-bars (blue lines) are the measured (calculated) data with 90 experimental runs. The calculation is based on Eq. 3.18 by using the four-level model.

Figure 6.1 displays the measured (markers with error-bars) and calculated (lines) survival probability as a function of the pulse period T after a $N = 7$ pulse train, where we use a horizontal arrangement of the standing wave. It shows that a series of survival resonances

occur for specific values of T, which are at the integer multiples of half the Talbot time $nT_{\mathrm{T}}/2$ (with $n \in \mathbb{N}$) [50, 51]. The first three of which are for $n = 1$, 2 and 3, while the last two are for $n = 14$ and 15. These repeated peaks arise as a result of the matter-wave Talbot-Lau effect as expected in Chapter 3.

The blue lines are the numerical calculation based on the four-level model, where we account for the imbalance of the standing-wave light intensity using the measured losses from the view-ports and retro-mirror (see Fig. 5.7). Additionally, we add an incoherent offset to the calculation to compensate the unwanted background due to the spontaneous decay back to the F = 3 initial ground state. The four-level model agrees with the measurements without any fitted parameters, except the added offset.

6.1.2 Long pulse periods

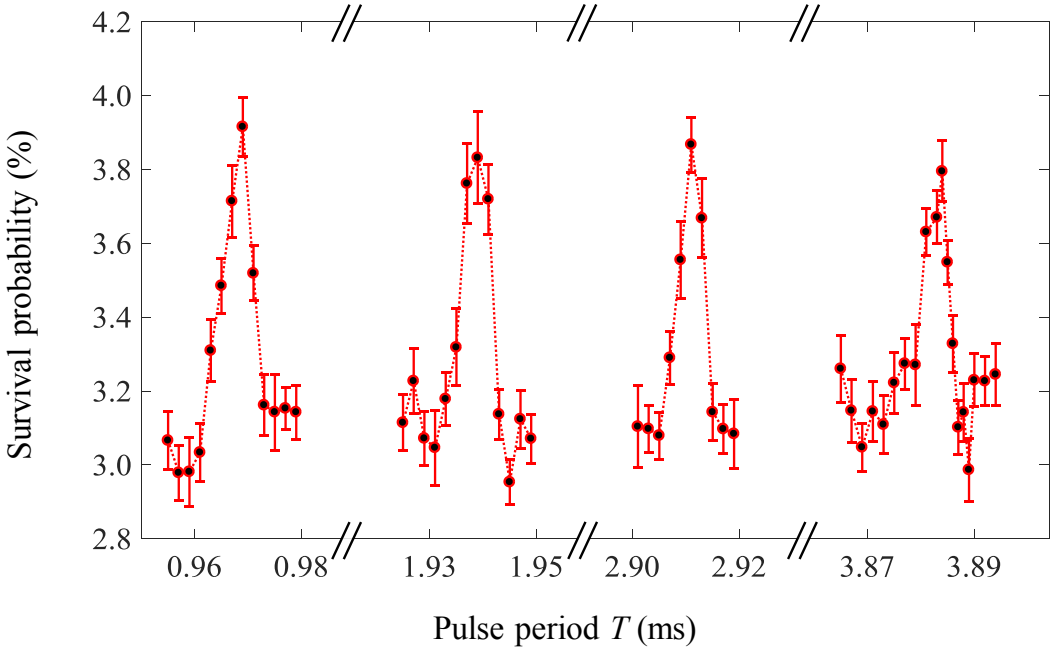

Figure 6.2: The survival resonances with a vertically arranged standing-wave light beam by setting $\boldsymbol{a} = \boldsymbol{g}$. Four resonant peaks are at the $n = 30$, 60, 90 and 120, respectively. The resonant peaks are measured with a $N = 5, \tau = 400$ ns pulse train. The standing-wave light frequency is tuned 10 MHz below the F = 3 to F$'$ = 2 transition on the D-2 line. The two beams' light intensities are 15 mW/cm^2. The circles are the average of 20 experimental runs and the error-bars show the standard deviation of the mean.

As an extension of Fig. 6.1, we keep increasing the pulse period T by using a vertical arrangement of the standing wave and setting $a = g$. Figure 6.2 demonstrates four survival resonance peaks that are for $n = 30$, 60, 90 and 120, which manifests this matter-wave interferometric phenomenon persists for long pulse periods. For the pulse period longer than 4 ms, the atoms drop out of the detection region of the PMT (see Fig. 5.9).

In Fig. 6.2, we see the peak height around 3.88 ms is smaller than the peak height at earlier time. The decaying of the peak height along the increase of the pulse period

is not captured by the model, where the model predicts the peak height is independent of the pulse period. The experimental effects that are not included in the model which could contribute to this may consist of: low-frequency phase noise of the standing-wave light due to the vibrations of the retro-mirror; transverse thermal motion of the atoms in the standing-wave beam that could contain phase distortions; and small residual forces on the atoms, for example, due to stray magnetic field gradients. Finally, the atoms split to higher diffraction orders will leave the detection area faster than the atoms that rapidly go to the dark state, which will also yield a monotonic decay of the signal size when increasing the pulse period.

In the experiment, selecting the right intensity for the standing-wave beam is crucial since a clear resonant peak occurs as a trade-off between two effects. If the intensity is too low, one sees high survivals for all pulse periods. On the other hand, when the intensity is too high, the height of the resonant peak becomes too small to resolve.

6.2 Micro-lensing

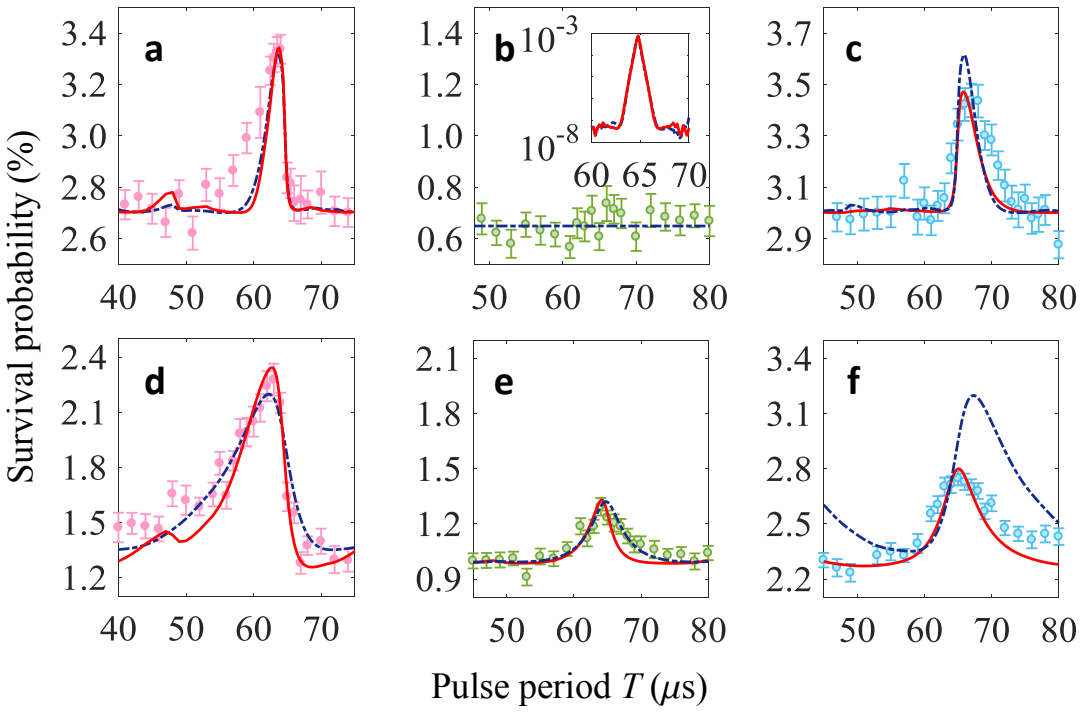

Figure 6.3: The measurements (markers with error-bars) and calculations (lines) of the survival resonances at the first Talbot time, with a horizontal arrangement of the standing wave. Each point is the mean of 20 experimental runs and the error-bars show the standard deviation of the mean. The red solid (blue dot-dashed) lines are calculations based on the four-level (two-level) model. The standing wave is formed by retro-reflecting a laser beam with the light intensities of 9 mW/cm^2 for (d-e). (a-c) The standing-wave light frequency is shifted by $\Delta/2\pi = -10$ MHz (red-detuned), 0 MHz (resonant) and 10 MHz (blue-detuned) with respect to the F = 3 to F$'$ = 3 transition. The inset of (b) shows the survival resonance calculated with two models in a logarithmic scale. (d-f) The standing wave light is tuned $\Delta/2\pi = -3$ MHz (red-detuned), 0 MHz (on resonance) and 3 MHz (blue-detuned) close to the F = 3 to F$'$ = 2 transition.

As discussed in Chapter 2, the standing-wave light pulses act as a hybrid of amplitude and phase grating. This section investigates how to change the relative strength between these two effects by varying the light frequency.

Figure 6.3 displays the survival resonances at the Talbot time T_{T} by using different light frequencies with a $N = 7, \tau = 300$ ns pulse sequence, where we use a horizontal standing-wave arrangement (similar to Fig. 6.1). For Fig. 6.3(a, b and c), the standing-wave light frequencies are 10 MHz below, on-resonant and 10 MHz above the atomic transition from $\mathrm{F} = 3$ to $\mathrm{F}' = 3$ on the D-2 line, respectively. While for Fig. 6.3(d, e and f), we scan the light frequency around the $\mathrm{F} = 3$ to $\mathrm{F}' = 2$ transition on the D-2 line, that are 3 MHz below, on-resonant and 3 MHz above, respectively. The markers with error-bars are the measurement.

The lines in Fig. 6.3 are the numerical calculations based on Eq. 3.19, with the blue dot-dashed lines for a two-level model and red lines for the four-level model (see Chapter 2). The latter agrees with the measurements without any fitted parameters. Treating the atom as a two-level system by only including the closest excited state also gives reasonable agreements when the standing-wave light intensity is a fitting parameter. The fitted intensity agrees with the measurement within 25%. However, we see that the two-level model fails to capture the asymmetry in the peak height for red and blue detuning that is visible in the experimental data. The asymmetry arises because the other excited hyperfine states will alter the phase and amplitude modulations differently on opposite sides of the resonance. To better capture the dynamics, we carry out the calculations by using the four-level model without any fitting parameters throughout the remaining of the thesis.

When using a detuned standing wave rather than an on-resonant one, Fig. 6.3 shows three distinct features that are:

1. the peak has an asymmetric shape with a sharp edge on one side and a smooth one on the other;

2. the peak survival is slightly shifted below or above the exact Talbot time for the red or blue-detuned laser;

3. the height of the survival resonance peaks increase dramatically.

The three features are a result of the phase modulation on the atomic wave function.

When the light is detuned from the exact atomic resonances, the standing-wave light pulse will imprint a spatially periodic phase onto the atomic wave function in addition to the amplitude modulation from the spontaneous photon scattering (see Eq. 2.38). This phase pattern acts as an array of lenses so that their effect is deemed "micro-lensing" [50, 126].

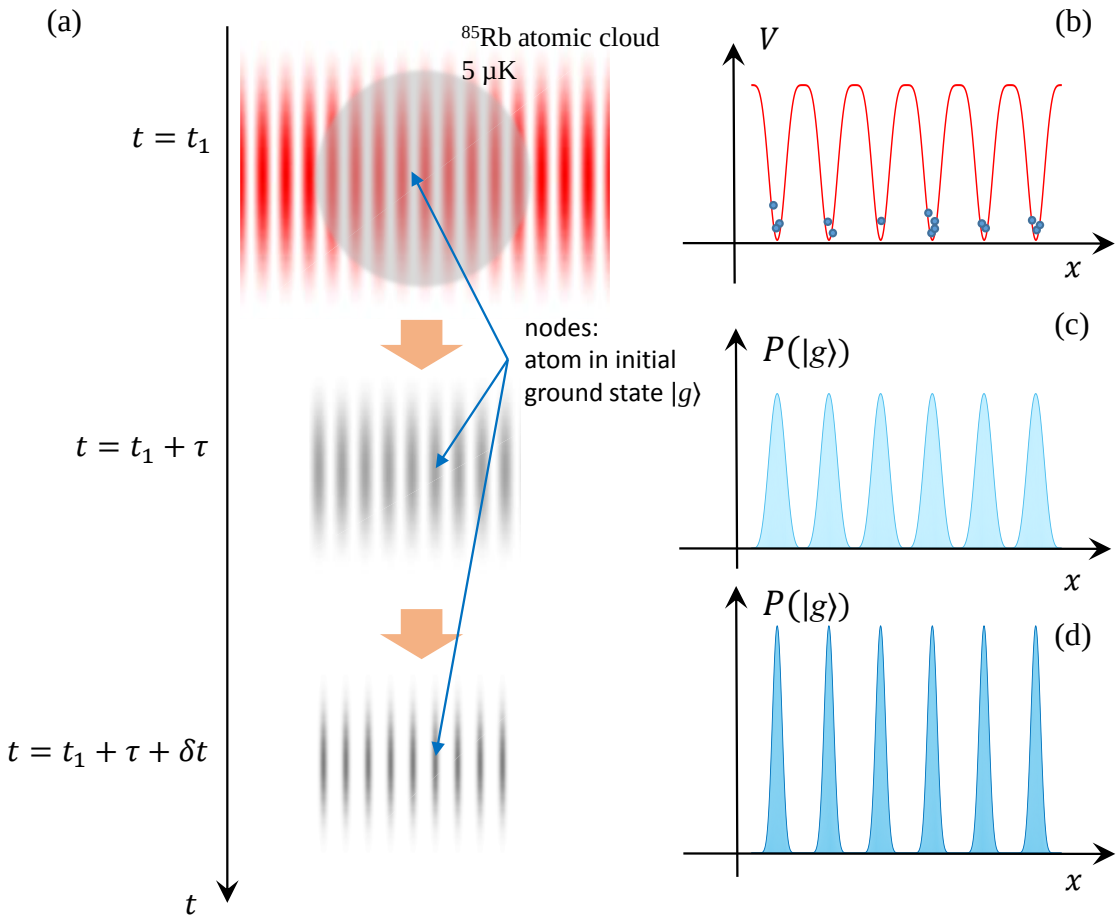

Figure 6.4: The micro-lensing effect. The effect of exposing the atomic cloud to a blue-detuned standing-wave light pulse.

(a) The standing-wave light field acts as an abortive grating that removes atoms from their initial ground state to the dark state everywhere except in the vicinity of the nodes [see (b)], similar to Fig. 2.3(b). After the pulse, the atomic density forms a comb-like distribution [see (c)]. At time δt after the pulse, the atoms forms a even narrower distribution due to the lensing effect cause by the still present detuning of the light [see (d)].

Depending on the detuning, the lens array could defocus or focus the atoms to the nodes of the standing wave. Figure 6.4 use the blue-detuned standing wave as an example to address the micro-lensing effect. As shown in Fig. 6.4(a), the standing wave forms a spatially periodic potential [see Fig. 6.4(b)]. When exposed to such a light pulse from time t_1 for a duration τ, the atoms go to the dark state everywhere except in the vicinity of the nodes. The atoms remaining in their initial ground state therefore form a comb-like distribution after the pulse [see Fig. 6.4(c)]. Since the optical dipole force arising from the blue-detuned standing wave directs atoms towards the low-intensity regions (the standing-wave nodes), the surviving atoms will form tight foci at time δt after the pulse [see Fig. 6.4(d)]. This means one can measure an enhanced survival probability when the pulse period is above T_{T} [see Fig. 6.3(c and f)].

For a red-detuned standing-wave light field, the dipole force directs atoms to the high-intensity region, and an enhanced survival resonance is shifted oppositely [see Fig. 6.3(a and d)]. When the light is on-resonant, we expect to obtain a symmetric peak centered at the Talbot time [see Fig. 6.3(b and e)]. The theory predicts a resonant peak for (b). However, the noise level of the measurement is above the signal size.

A useful feature in Fig. 6.3 is that the survival resonances provide a steep edge when the standing wave is not resonant. This allows for the precision measurement of the period of the signal, which is the Talbot time. It can be used to determine the ratio between the Planck's constant and the mass of the atom h/M:

$$\frac{h}{M} = \frac{2\pi^2}{k_L^2}\frac{1}{T_{\mathrm{T}}}, \tag{6.1}$$

through measuring k_L and T_{T}. It is an interesting measurement since h/M is the least determined quantity in the precision measurement of the fine structure constant α [38,39]:

$$\alpha^2 = \frac{2\mathrm{R}_\infty}{c}\frac{M}{M_{\mathrm{e}^-}}\frac{h}{M}, \tag{6.2}$$

where the Rydberg constant R_∞ is known to 0.006-ppb accuracy, and the atom-to-electron mass ratio M/M_{e^-} is known to better than 0.1 ppb, and c is the speed of light in vacuum.

6.3 Pulse number evolution

To further understand the dynamics of the system, this section studies how the survival resonances evolve as a function of the pulse number N. To extract the peak height H and width σ of the resonant peaks, we fit a two-piece normal distribution to the data. The fitting curve is:

$$f(x) = \begin{cases} a\exp\left(-\frac{(x-b)^2}{2c_1^2}\right) + d, & \text{for } x < b \\ a\exp\left(-\frac{(x-b)^2}{2c_2^2}\right) + d, & \text{for } x \geq b \end{cases}, \tag{6.3}$$

where the fitting parameters are: a the peak amplitude; b the peak position; d the offset and c_1 and c_2 the peak width for the left and right side respectively. Equation 6.3 is a combination of two Gaussian profiles with different widths but the same amplitude, center and offset. This is a good model for capturing the asymmetry of the resonant peak.

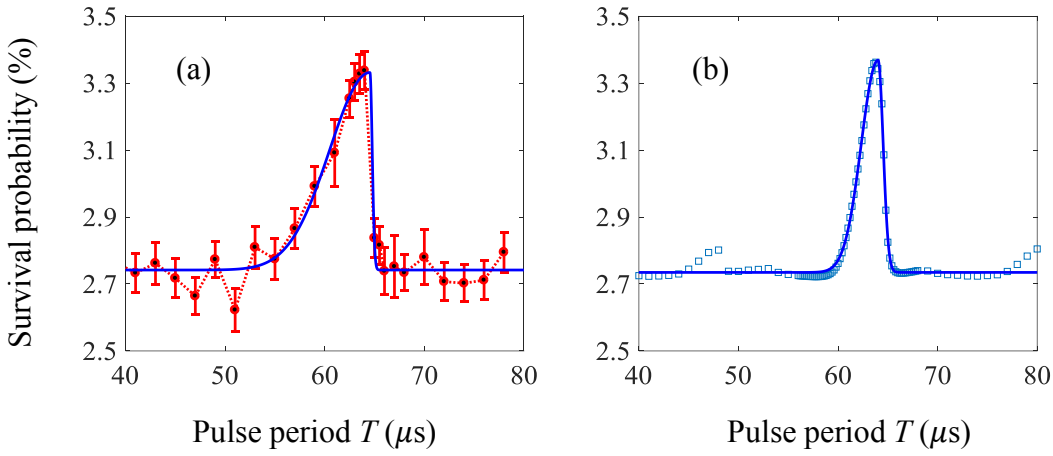

Figure 6.5: The two-piece normal distribution fit to the measured (a) and calculated (b) survival resonance peaks. (a) The red circles are the average of 90 experimental runs with the error-bars showing the standard deviation of the mean. (b) The light-blue squares are the calculation based on the Eq. 3.12 with the four-level mode. The blue lines are the two-piece normal distribution fit based on Eq. 6.3.

Figure 6.5 displays two typical fitted curves to the measurement (a) and calculation

(b), where we extract the amplitude a as the peak height H, and right-side width c_2 as the steep-side width σ. The measured and calculated survival resonances in Fig. 6.5 are the same as the resonant peak shown in Fig. 6.1 at $T = T_{\mathrm{T}}$.

6.3.1 Peak height H

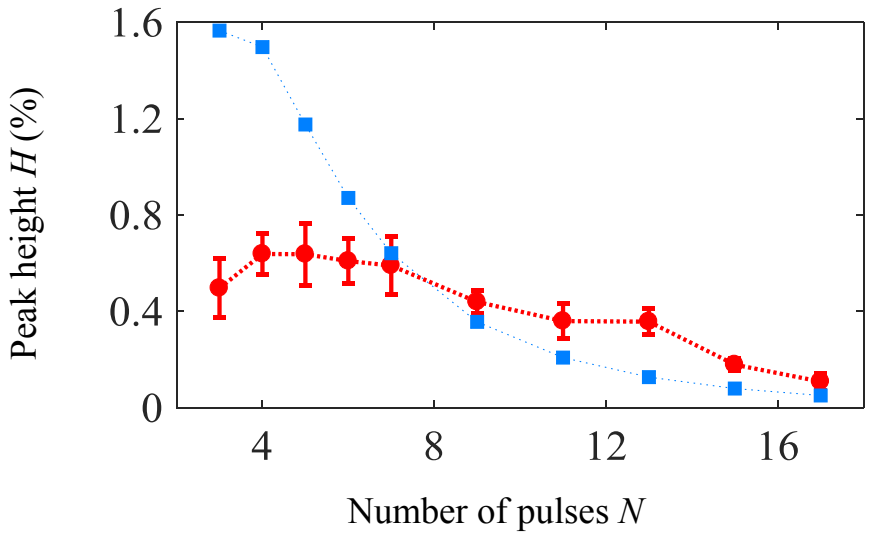

Figure 6.6: The peak height H of the survival resonances as a function of the pulse number N. The red circles are the experiments and the blue squares are the calculation. Error bars denote the confidence interval for one standard deviation for the two-piece normal distribution fitting that is given in Eq. 6.3.

Figure 6.6 displays the peak height H as a function of the pulse number N. Both the measured (red) and calculated (blue) data show a declining trend with the increasing N, since each standing-wave light pulse continuously removes the atoms from their initial ground state to the dark state.

In Fig. 6.6, there is a significant discrepancy between the calculations and measurements for small N-values ($N < 6$). This difference could potentially come as a result of the imperfection of the model that ignores the spontaneous decay back to their initial ground state. On the D-2 line transition of ^{85}Rb atoms (see Fig. 2.2), there are two channels for the

atoms in the $F' = 3$ excited state can decay to, which are the $F = 2$ dark ground state (desirable channel) and the $F = 3$ initial ground state (unwanted channel). The spontaneous emission branching ratio between these two channels is $\Gamma_{3' \to 3}/\Gamma_{3' \to 2} = 5/4$ [91, 110]. The average rate for going to the $F = 2$ state is therefore $4/9$. The lower boundary of the time that requires for pumping the atom from $F = 3$ state to $F = 2$ state is $(9/4)2\tau_{\text{life}} = 122$ ns, where $\tau_{\text{life}} = 26$ ns is the lifetime of the $F' = 3$ excited state [91]. This requires that the overall duration for the standing wave should be long enough to pump the atoms out of the initial state. This can be seen from that the survival resonance has a significant offset for small N values, e.g. 16% for $N = 3$. Furthermore, for small N, the resonance peak also shows a more complex structure than clearly separated peaks. However, we do not expect this to cause the discrepancy since the height evaluation method is the same for the measurements and calculations. For $N > 6$, it shows a better agreement between the measured and calculated data.

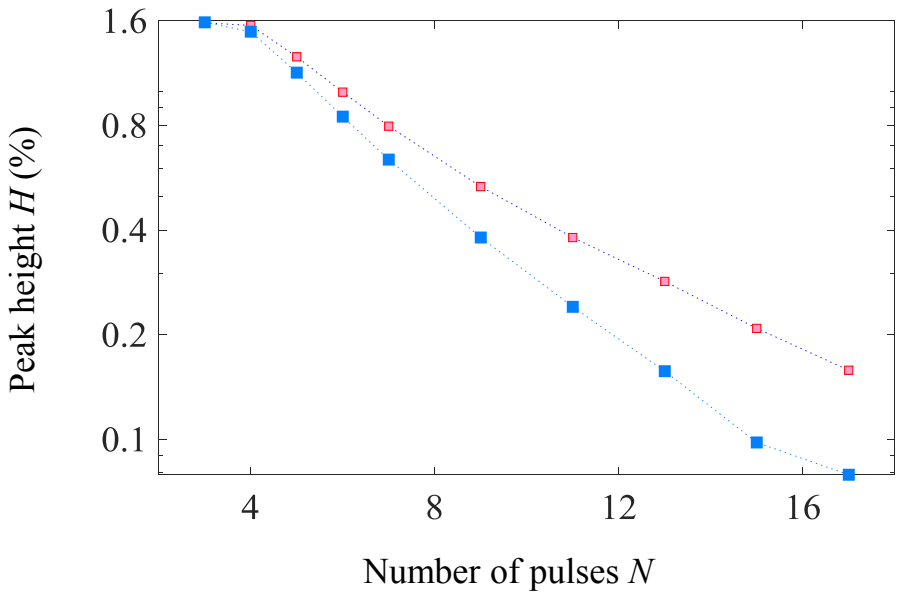

Figure 6.7: The calculated peak height H of survival resonances as a function of the pulse number N (in a semi-logarithm scale). The blue squares are the peak height calculated using imbalanced standing wave (accounting for the power loss due to the view-ports and retro-mirror) while the red squares are with a perfectly balanced one (see Eq. 2.5). The rest of the parameters are the same as in Fig. 6.6.

Figure 6.7 shows the calculated peak height as a function of the pulse number for balanced (red) and imbalanced (blue) standing waves. It shows a higher height when using a balanced standing wave rather than an imbalanced one. This is not surprising since the nodes of the imbalanced standing wave are not completely dark. It means that even the atoms are at the nodes, they still can scatter light and go to the dark state, which gives rise to a lower atomic survival. While, for a standing wave having perfect dark nodes, the atoms can survive and contribute to the peak.

Even though we use a balanced standing wave, Fig. 6.7 still shows a decaying peak height (red). This is because the atomic distributions inevitably have a finite width around the nodes and therefore will remain scattering light and going to the dark state.

6.3.2 Peak width σ

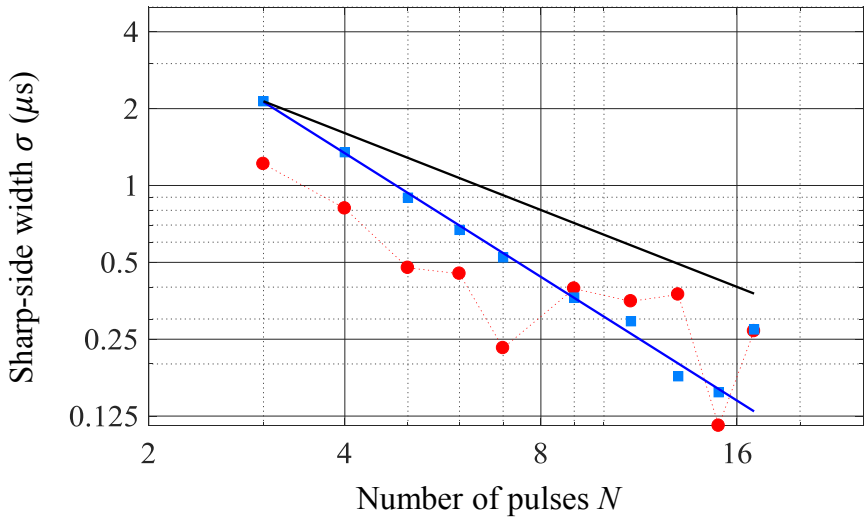

Figure 6.8: The peak width σ from the sharp side of the survival resonance peaks as a function of N in a logarithm scale. The red circles are the experimental data and the blue squares are the calculated data. The blue line is the power law fitting to the calculation with a power of -1.66, while the black line is a curve proportional to $1/N$ for comparison.

We now study the evolution of the peak width as a function of N. Figure 6.8 displays the measured (red circles) and calculated (blue squares) peak width σ when varying the pulse number, where σ is from the sharp-side of the survival resonance peaks (see Fig. 6.5). It shows a monotonically decreasing tendency with an increasing N. This is because an increasing number of pulses leads the atomic waves to be split into higher diffraction orders that accumulate phases at a higher rate during the free evolution (see Eq. 3.2). This results in a more stringent requirement on the free evolution time T to guarantee that the different diffraction orders are in phase to produce sharp coherent echoes at the time of the subsequent pulses.

Sub-Fourier behavior

The Fourier limit states that the time required to distinguish two frequencies is inversely proportional to the frequency difference $\Delta\omega$. This gives the relation that the time for discriminating the periods of two signals is also inversely proportional to their difference [127]. For example, if we double the frequencies of the two component, the frequency difference doubles, which requires a less time to distinguish them. Figure 6.8 shows the calculated data is well fitted by a power-law (blue line) with the power of -1.66. This is not the power of N^{-1} as expected from the Fourier relation (black line). This super-resolution originates from that the atoms gain a momentum transfer of more than $2\hbar k_L$ from each pulse [127]. The atoms with higher momentum evolve at a higher frequency compared to the atoms evolving with the fundamental frequency (recoil frequency $\omega_r = \pi/2T_{\mathrm{T}}$). This gives rise to a better sensitivity when comparing them for a given time duration. The system therefore shows a sub-Fourier behavior, which has also been seen with the standard AOKDR [80, 81]. We see a similar power-relation for the experiments for small N, until the width gets too small that the signal-to-noise ratio is reduced.

The sub-Fourier behavior is desirable since a sharper peak can increase the sensitivity when determining the separation between peaks. Since a steep peak means that even a small deviation in time can cause a significant variation in the survival probability, we can obtain a good measurement sensitivity in this region.

6.4 Summary

In this chapter, we have experimentally investigated the survival resonances and compared the results to the theory described in Chapter 3. The system displays a comb of narrow resonance peaks separated by half the Talbot time $T_{\mathrm{T}}/2$ when scanning the pulse period. The survival resonances are a consequence of the matter-wave Talbot-Lau effect and can be observed using an incoherent ensemble of particles (a thermal atomic cloud in the thesis).

Furthermore, the phase modulation results in a micro-lensing effect that can enhance the signal size of the resonant peaks. The four-level model agrees well with the experiments for short pulse period. The width of the survival resonances displays a sub-Fourier behavior with an increasing number of pulses.

Part III

Applications using Survival Resonances

Chapter 7

Feedback enhanced survival resonances

In previous chapters, we investigated survival resonances in an atom-optics system driven by the temporally and spatially periodic dissipation (see Chapter 6). This chapter will investigate how to enhance these resonances by actively feeding the lost atoms back to the system. The method uses survival resonances to select atomic waves with particular spatial and momentum distributions, which we deem "long surviving modes". The atoms in such modes have a higher chance to survive the pulse sequence. Otherwise, the atoms are lost to a "reservoir", which is the dark state. Feedback of the lost atoms from the reservoir to the system gives them a second chance to be in a long surviving mode and contribute to the atomic survival. This feedback mechanism thereby results in an enhancement of the survival resonances.

The present chapter begins with a brief description of the experimental procedure. It then studies the long surviving modes and the feedback mechanism with a numerical model. Subsequently, it shows the enhancement of survival resonances due to the feedback state preparation, and gives the evolution of the peak height with different experimental parameters. The last section provides the discussion and conclusion.

7.1 The experimental procedure

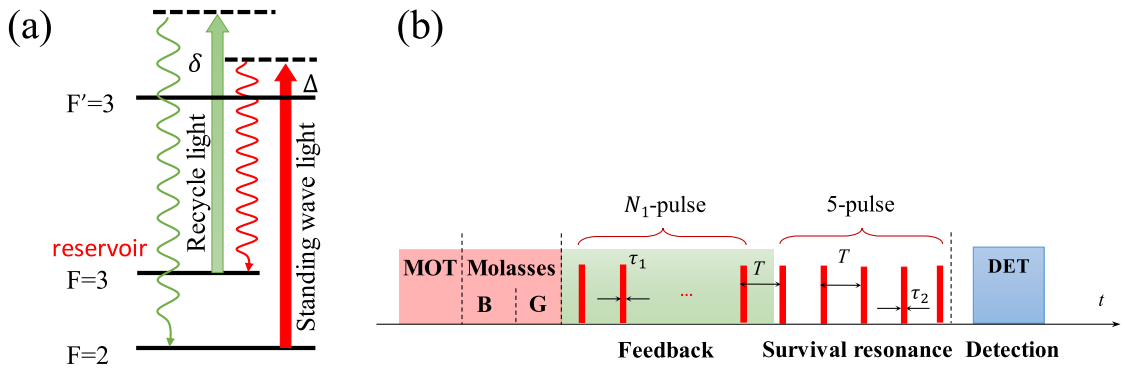

Figure 7.1: (a) Simplified energy level diagram (not to scale). ^{85}Rb atom D2-line transition: the F = 2 hyperfine ground state is the initial ground state $|g\rangle$, and the F = 3 state is the dark ground state $|g_{\mathrm{D}}\rangle$. The standing-wave light (red arrow) is tuned $\Delta/2\pi = 5$ MHz above the open atomic transition from F = 2 to F$'$ = 3. The recycling light (green arrow: gray-molasses cooling light) is shifted $\delta/2\pi = 25$ MHz above the transition from F = 3 to F$'$ = 3. (b) Time sequence of the experiment (not to scale). Acronyms: MOT magneto-optical trap, B bright molasses, G gray molasses, DET atomic state detection. T is scanned at the first Talbot time T_{T} and τ_2 is 400 ns. Green shade represents recycle light that is switched off 40 μs after the last pulse in N_1-pulse train. Red rectangles denote standing-wave light pulses.

Contrary to the previous chapter, we now use the F = 2 hyperfine ground state of the ^{85}Rb atoms as the initial state, and the F = 3 hyperfine ground state as the dark state [see Fig. 7.1(a)]. The standing wave is formed by retro-reflecting a horizontal laser beam with an intensity of 5.2 mW/cm^2, and its frequency is tuned 5 MHz above the open atomic transition from F = 2 to F$'$ = 3 (the hyperfine excited state on the D2-line).

When exposed to standing wave pulses, the atoms will scatter photons and decay to the dark state. Those atoms falling into the dark state form a reservoir [see Fig. 7.1(a)]. To transfer atoms from the reservoir back to the initial state, we need to apply optical pumping light, which is deemed "recycle light" (green arrow). To achieve this goal, we

use molasses cooling light to optically pump the atoms from F = 3 to F = 2. Particularly, we use gray molasses cooling light rather than bright molasses light to feed back the lost atoms efficiently, since the gray molasses can rapidly transfer the atoms (see Fig. 5.5). Furthermore, the gray molasses cooling light can simultaneously cool the atoms in the reservoir, which helps to prevent the atoms from heating up due to the photon scattering from the standing wave.

To investigate how the feedback process works, we conduct experiments using the time sequence shown in Fig. 7.1(b). We initiate the atoms in the F = 2 state at a temperature of 5 μK. Subsequently, we expose them to a train of standing wave pulses, which is divided into two segments. In the first part, N_1 pulses (with duration τ_1) are applied when the recycle light is simultaneously on. During this process, the standing wave pulse sequence modulates the atomic wave function, which can lead to a peak survival when the pulse period is any integer multiple of half the Talbot time (see Chapter 6). The recycle light rapidly feeds the atoms back to their initial state and gives them another chance to contribute to the atomic survival, which may leads to a higher survival probability. We deem this part as the feedback stage. In the second part, 5 pulses (with duration $\tau_2 = 400$ ns) are applied after switching off the recycle light, which is used to analyze the atomic distribution after the feedback stage. After the pulse sequence, we measure the survival probability using the method given in Section 5.4 (see Fig. 5.14).

7.2 Long surviving modes

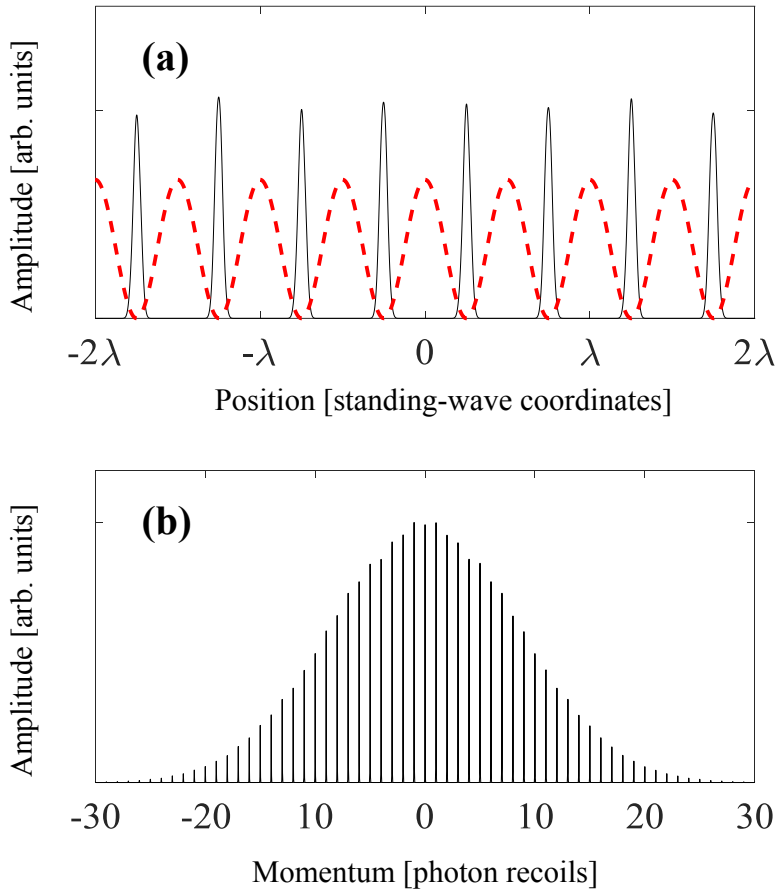

Figure 7.2: Theoretical position (a) and momentum (b) distribution of the atoms that survive a 5-pulse train of the standing wave. The pulse period is $T = T_{\mathrm{T}}$. The momentum distribution consists of a comb of peaks separated by one photon recoil. The wave function of the atoms remaining in F = 2 state are spatially localized around the nodes of the standing wave when the self-image forms. The red-dashed line in (a) shows the position of the standing wave light.

To demonstrate the long surviving modes, we examine the atomic density distribution of the atomic waves after exposing them to a standing-wave pulse sequence. The black lines in Fig. 7.2 show such distributions in position (a) and momentum (b) space, which are calculated as following. We initiate a set of atomic wave packets (see Fig. 3.5) that

cover one period of the standing wave homogeneously. We then propagate each of them through 5 on-resonant standing wave pulses with the pulse period $T = T_{\mathrm{T}}$. After the pulse sequence, each wave packet will be coherently split into a number of diffraction orders. Finally, incoherently summing over all the resulting probability distributions from different initial wave packets at time T after the last pulse yields the plots in Fig. 7.2.

In Fig. 7.2(a), we see that the atoms surviving all 5 pulses form a certain distribution, where the atoms are near the nodes of the standing wave. This distribution ensures the atoms to have a longer lifetime during the standing wave pulse sequence, since the atom-light interaction is weak in these low intensity regions. We deem the atomic distributions shown in Fig. 7.2(a) the "long surviving modes".

As can be seen in Fig. 7.2(b), the momentum state probability density distribution of the long surviving mode resembles a comb with a tooth spacing of $\hbar k_L$. This can be understood through the matter-wave Talbot-Lau effect. We consider an atomic plane wave $\exp(ik_0x)$ (with $k_0 = p_0/\hbar$ and p_0 the initial momentum) is exposed to two standing wave pulses that are separated by a period T. For simplicity, we apply the first pulse at $t = 0$ and the second pulse at $t = T$. Each pulse will split the atomic waves into a number of diffraction orders that differ by $2\hbar k_L$. We use the index number n and m to denote the diffraction orders for the first and second pulse, where $n, m \in \mathbb{Z}$. The atomic wave function after the second pulse at time $t = 2T$ has the form (see Chapter 3):

$$\psi_{k_0}(x, 2T) = \sum_m \sum_n c_m c_n \exp\left[-i\frac{\hbar T}{2M}\left((m^2 + 2n^2 + 2mn)4k_L^2 + (m + 2n)4k_0k_L\right)\right] \times \exp[i(m + n)2k_Lx + ik_0x], \tag{7.1}$$

where we have ignored the global phase $\exp\left[-i\left(\hbar k_0^2 T/M\right)\right]$ (with M the mass of atom). Now let's turn our attention to the phase term related to n and m:

$$\phi_{n,m}(2T) = \frac{\hbar T}{2M}\left((m^2 + 2n^2 + 2mn)4k_L^2 + (m + 2n)4k_0k_L\right). \tag{7.2}$$

The pulse period is set to be $T = \alpha T_{\mathrm{T}}$ (with $T_{\mathrm{T}} = \pi M/\hbar k_L^2$ and $\alpha \in \{1/2, 1, 3/2, 2, 5/2, \cdots\}$) that allows for the observation of the survival resonances (see Chapter 6). Eq. 7.2 then

becomes:

$$\begin{aligned}\phi_{n,m}(2\alpha T_{\mathrm{T}}) &= \frac{\hbar}{2M}\alpha\frac{\pi M}{\hbar k_L^2}4k_L^2\left((m^2+2n^2+2mn)+(m+2n)\frac{k_0}{k_L}\right)\\ &= 2\pi\alpha\left((m^2+2n^2+2mn)+(m+2n)\frac{k_0}{k_L}\right)\\ &= 2\pi\left(\alpha m^2+(m+2n)\frac{k_0}{\alpha^{-1}k_L}\right),\end{aligned} \tag{7.3}$$

where we have neglected the term $(2n^2+2mn)$, which only adds a phase that is the integer multiples of 2π and has no physical significance.

We now search for the k_0-components that contribute to the long surviving modes. This is to find the condition that ensures the wave function to revive after the free evolution between pulses, which requires the phase factor in Eq. 7.1 equal to 1. We search for k_0 in two separated cases, one is for $\alpha \in \mathbb{N}$ and the other is for $\alpha = q + \frac{1}{2}$ where $q \in \mathbb{N}$.

CASE-I: When α is an integer, $\phi_{n,m}(2\alpha T_{\mathrm{T}})$ in Eq. 7.3 is an integer multiples of 2π for all m and n if we have $k_0 = \alpha^{-1}\ell k_L$ (with $\ell \in \mathbb{Z}$). When $k_0 \neq \alpha^{-1}\ell k_L$, $\left(\alpha m^2 + (m+2n)\frac{k_0}{\alpha^{-1}k_L}\right)$ will not always be an integer for all m and n. Taking $m = 1$ and $n = 0$ as an example, the bracket term in Eq. 7.3 reduces to $(\frac{k_0}{\alpha^{-1}k_L} + \alpha)$, which is a fractional number. We can therefore conclude that the phase term $\phi_{n,m}(2\alpha T_{\mathrm{T}})$ in Eq. 7.3 is an integer multiple of 2π if and only if $k_0 = \alpha^{-1}\ell k_L$.

CASE-II: When $\alpha = q + 1/2$ (with $q \in \mathbb{N}$), we can rearrange Eq. 7.3 as:

$$\begin{aligned}\phi_{n,m}(2\alpha T_{\mathrm{T}}) &= 2\pi\left[\left(q+\frac{1}{2}\right)m^2+(m+2n)\left(q+\frac{1}{2}\right)\frac{k_0}{k_L}\right]\\ &= 2\pi\left[\frac{1}{2}m^2+(m+2n)\left(q+\frac{1}{2}\right)\frac{k_0}{k_L}\right],\end{aligned} \tag{7.4}$$

where we have omitted the qm^2 term since it is an integer. We would like to find the k_0 value that leads $\phi_{n,m}(2\alpha T_{\mathrm{T}})$ to be an integer multiple of 2π for all m and n. Since we require $\left[\frac{1}{2}m^2 + (m+2n)\left(q+\frac{1}{2}\right)\frac{k_0}{k_L}\right]$ to be integer for all m and n, it needs to be an integer for $n = 0$ and $m = 1$:

$$\begin{aligned}\phi_{n,m}(2\alpha T_{\mathrm{T}}) &= 2\pi\left[\frac{1}{2}+\left(q+\frac{1}{2}\right)\frac{k_0}{k_L}\right]\\ &= 2\pi\left(\frac{1}{2}+\alpha\frac{k_0}{k_L}\right).\end{aligned} \tag{7.5}$$

We see that only k_0 fulfilling $k_0 = \alpha^{-1}\left(\ell - \frac{1}{2}\right)k_L$ will make $\phi_{n,m}(2\alpha T_{\mathrm{T}})$ in Eq. 7.5 be an integer multiples of 2π (with $\ell \in \mathbb{Z}$). We can therefore request these k_0 to make the square bracket term in Eq. 7.4 to be an integer for arbitrary m and n. Rewriting Eq. 7.4 by including $k_0 = \alpha^{-1}\left(\ell - \frac{1}{2}\right)k_L$ yields:

$$\begin{aligned}\phi_{n,m}(2\alpha T_{\mathrm{T}}) &= 2\pi\left[\frac{1}{2}m^2 + (m+2n)\alpha\frac{1}{k_L}\alpha^{-1}\left(\ell - \frac{1}{2}\right)k_L\right] \\ &= 2\pi\left[\frac{1}{2}m^2 + (m+2n)\left(\ell - \frac{1}{2}\right)\right] \\ &= 2\pi\left[\frac{1}{2}m\,(m-1)\right],\end{aligned} \tag{7.6}$$

where we ignore the term $[(m+2n)\ell - n]$ since it is an integer. We now pay a close attention to $\frac{1}{2}m(m-1)$ in Eq. 7.6, and find that the two neighbor integer numbers m and $m-1$ must be a combination of one even number and one odd number because of $m \in \mathbb{Z}$. $\frac{1}{2}m(m-1)$ is therefore an integer. This again leads the phase $\phi_{n,m}(2\alpha T_{\mathrm{T}})$ in Eq. 7.3 to be an integer multiples of 2π.

The initial momentum p_0 of the atoms that contribute to long surviving modes are therefore given by:

$$p_0 = \hbar k_0 = \alpha^{-1}\ell\hbar k_L + \begin{cases} 0 & \alpha \in 1, 2, 3, \cdots \\ \frac{1}{2}\alpha^{-1}\hbar k_L & \alpha \in \frac{1}{2}, \frac{3}{2}, \frac{5}{2}, \cdots \end{cases} \tag{7.7}$$

For $\alpha = 1$ used in Fig. 7.2, we observe a tooth spacing of $\hbar k_L$. These particular states of atoms given in Eq. 7.7 are forming the long surviving modes.

The atoms that are not in long surviving modes scatter light from the standing wave and go to the reservoir. However, applying the recycle light can transfer atoms in the reservoir back to the system. During the transferring process, the recycle light initiates the atoms to a temperature of 5 μK, which leads the atoms to form the same momentum distribution as just after the state preparation stage. This gives the atoms another chance to be populated at those particular momentum states (see Eq. 7.7) that have a higher surviving chance. It will lead the atomic population to build up in the long surviving

modes, and therefore enhance the signal size of the survival resonances. The atoms in long surviving modes are off-resonance to the recycle light, which leaves them unchanged during the experiment. In this process, tailored dissipative dynamics continuously corrects the atomic state of the atoms in F = 2 by coupling the internal degrees of freedom of atoms to an environment that is subjected to a cooling mode [128].

To summarize, the feedback enhanced survival resonances come as a result of the momentum state preparation, which we can view as a laser "cooling" process. In the system, the atoms in F = 2 are not chilled to the lowest energy state as in an ordinary cooling procedure. Contrarily, they dissipate towards a superposition of momentum states, which is ideal for the subsequent interferometry experiments since they result in a higher atomic survival and therefore a better signal-to-noise ratio. This process bears the similarity of the velocity-selective coherent population trapping, where the cooled atoms decouple from the laser field and dissipate to a coherent superposition of momentum states with $\pm\hbar k_L$ [129]. In this sense, it is parallel to use the engineered dissipation to generate entangled states that are ideal for the calculation in quantum computers. These entangled states are dark to the dissipations [130–134].

7.3 Numerical calculation

We now give the method that allows for simulating the system subjected to a feedback sequence based on the present simulation (used for calculating the survival probability given in Chapter 3). We consider a standing wave pulse train with N pulses that form the probe sequence, and N_1 pulses are overlapped with the recycle light (forming the feedback stage).

We denote the probability of the atoms surviving κ consecutive pulses s_κ, where $\kappa \leq N_1 + N$. We can directly compute s_κ by evolving the wave function using time evolution in Eq. 3.24. For those atoms that are removed from the initial state to the dark state,

they will be transferred back to the initial state before the next pulse with an efficiency γ. When using the gray molasses cooling light to feed back atoms (see Fig. 5.5), γ is a time-dependent term that has the form of Eq. 5.1, where $\gamma(T) = 1 - e^{(-3.2\times10^4 \mathrm{s}^{-1}T)}$, with T the pulse period. After each pulse-recycle loop, the internal states of the atomic cloud is in a mixture of the F = 2 initial state and the F = 3 dark state. The probabilities for the atoms being in these two states can be calculated in an iterative way.

We use $P_{\chi,-}(D)$ (and $P_{\chi,+}(D)$) to represent the probability for the atoms in the dark state just before (and after) the χ-th pulse, where $\chi \leq N_1$ and the letter D denotes the dark state. Define d_χ to be the "death probability" at the χ-th pulse, that is the atoms being removed from the initial state to the dark state by the χ-th standing wave pulse. The probability for the atoms in the dark state just after the χ-the pulse is therefore given by:

$$P_{\chi,+}(D) = P_{\chi,-}(D) + d_\chi. \tag{7.8}$$

Due to the presence of the recycle light, the atoms in the dark state will be transferred back to the initial state with a feedback efficiency $\gamma(T)$. The probability for the atoms remaining in the dark state just before the next $(\chi+1)$-th pulse is:

$$\begin{aligned} P_{(\chi+1),-}(D) &= [1-\gamma(T)]\, P_{\chi,+}(D) \\ &= [1-\gamma(T)]\, [P_{\chi,-}(D) + d_\chi]\,. \end{aligned} \tag{7.9}$$

We can therefore calculate $P_{\chi,\pm}(D)$ for all χ iteratively if we know d_χ.

Now we turn the attention to the death probability d_χ, which denotes the probability for removing atoms to the dark state at the χ-th pulse. They come from two parts. One is from those atoms that survive all the previous $(\chi-1)$ pulses but not the last χ-th pulse. These atoms do not experience any feedback process. The other part is from the atoms that undergo the feedback producers and are eventually removed by the χ-th pulse. We consider the second case as follows.

For a pulse train containing χ pulses, we consider the atoms are removed to the dark

state at the $(\chi - i)$-th pulse (labeled as $d_{\chi-i}$), where $i < \chi$. Together with the atoms remaining in the dark state before the $(\chi-i)$-th pulse [labeled as $P_{(\chi-i),-}(D)$], the recycle light transfers them back to the initial state with an efficiency $\gamma(T)$ before the $(\chi-i+1)$-th pulse (denoted $\gamma(T)\left[d_{\chi-i} + P_{\chi-i,-}(D)\right]$). After being fed back, they survive the remaining $(i-1)$ pulses and are then depumped to the dark state by the i-th pulse, which is also the last pulse during the χ-pulse train. The probability for the atoms going through this path is given by $\gamma(T)\left[d_{\chi-i} + P_{\chi-i,-}(D)\right]\left[s_{(i-1)} - s_{(i)}\right]$. Summing this probability over i from 1 to $(\chi - 1)$ gives the proportion for the atoms experiencing a "death-feedback-death" process. The death probability at the χ-th pulse d_χ is therefore given by:

$$d_\chi = \left[s_{(\chi-1)} - s_{(\chi)}\right] + \sum_{i=1}^{\chi-1} \gamma(T)\left[d_{\chi-i} + P_{\chi-i,-}(D)\right]\left[s_{(i-1)} - s_{(i)}\right], \tag{7.10}$$

where $d_1 = (1 - s_1)$ since all the atoms start from the F = 2 state before the first pulse. The first term $\left[s_{(\chi-1)} - s_{(\chi)}\right]$ originates from the atoms survive all $(\chi - 1)$ pulses but not the χ-th one as discussed above. From Eq. 7.10, we once again see that we can compute d_χ for all χ by applying Eqs. 7.9 and 7.10 in an iterative way.

Based on the results given above, we can now conduct the calculation for the survival probability of the atoms $\mathbb{S}$ after a $(N_1 + N)$-pulse train. Here N_1 pulses are overlapped with the recycle light and N pulses are applied as the probe sequence. The atoms that can survive the probe sequence are also from two cases. The first situation is for the atoms surviving all the $(N_1 + N)$ pulses, which is directly given by $s_{(N_1+N)}$. In the second case, the atoms will experience a "death-survival" process. They will first be removed to the dark state, and then survive the remaining pulses after being transferred back to the initial state.

For the $(N_1 + N)$-pulse train configuration, the recycle light will re-initiate the atoms being removed to the dark state at the χ-th pulse (labeled as d_χ) and remaining in the dark state just before the χ-th pulse (labeled as $P_{\chi,-}(D)$) with an efficiency $\gamma(T)$ (for $\chi \leq N_1$). The proportion for the atoms that are fed back by the recycle light before

the next $(\chi+1)$-th pulse is therefore $\gamma(T)\left[d_\chi + P_{\chi,-}(D)\right]$. They then survive the left $(N_1+N-\chi)$ pulses with a survival probability $s_{(N_1+N-\chi)}$. The probability for the atoms participating in a "death-survival" process is a sum of $\gamma(T)\left[d_\chi + P_{\chi,-}(D)\right] s_{(N+N_1-\chi)}$ over χ from 1 to N_1. The total survival probability $\mathbb{S}$ is therefore given by:

$$\mathbb{S} = s_{(N+N_1)} + \sum_{\chi=1}^{N_1} \gamma(T)\left[d_\chi + P_{\chi,-}(D)\right] s_{(N+N_1-\chi)}, \tag{7.11}$$

where the first term arises from the atoms surviving all the pulses, while the second sum term accounts for the atoms experiencing a "death-survival" procedure.

For the maximum feedback efficiency $\gamma = 1$, $P_{\chi,-}(D)$ in Eqs. from 7.8 to 7.11 is 0. Eqs. 7.10 and 7.11 therefore simplify to:

$$\begin{aligned} d_\chi &= \left[s_{(\chi-1)} - s_{(\chi)}\right] + \sum_{i=1}^{\chi-1} d_{(\chi-i)}\left[s_{(i-1)} - s_{(i)}\right], \\ \mathbb{S} &= s_{(N+N_1)} + \sum_{\chi=1}^{N_1} d_\chi s_{(N+N_1-\chi)}. \end{aligned} \tag{7.12}$$

The computation presented here inherits the defect of the model in Chapter 3, where we ignore the spontaneous decay back to the initial ground state. The model therefore fails to capture the offset of the measurement, and we again manually add an incoherent shift to the calculation for compensating the difference.

7.4 Results

To explore the feedback mechanism, we measure the survival probability while varying experimental parameters.

7.4.1 Enhanced resonance peak

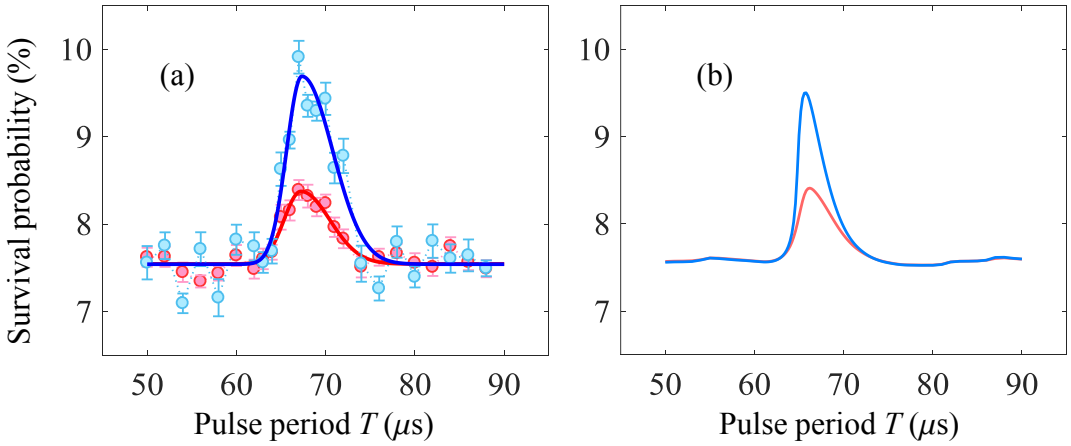

Figure 7.3: (a) The measured survival resonances without (red markers with error-bars) and with (blue markers with error-bars) the feedback sequence. The markers are the average of 20 experimental runs. The red and blue lines are the two-piece normal distribution fitting curves (see Eq. 6.3). (b) The calculated survival resonance (red line) and feedback enhanced resonance peak (blue line).

We first investigate the survival resonances with and without the feedback stage. Figure 7.3 displays the measured (a) and calculated (b) survival resonances at the first Talbot time. The probe sequence containing 5 standing wave pulses is used to analyze the survival probability after the feedback stage. It shows two sets of resonance peaks. One is the conventional resonance peak without feedback sequence, where $N_1 = 0$ [shown with the red-markers in (a) and red line in (b)]. The other is an enhanced survival resonance with the feedback process, where $N_1 = 6, \tau_1 = 400$ ns [shown with the blue-markers in (a) and blue line in (b)]. We immediately see that having 6 preparation pulses increases the peak height significantly.

To evaluate the peak height, we fit a two-piece normal distribution to the data using Eq. 6.3 [the lines in Fig. 7.3(a)]. From the fit, we see an enhancement with the factor of 2.6 of the peak height between these two cases, which is also captured by the calculation [see Fig. 7.3(b)].

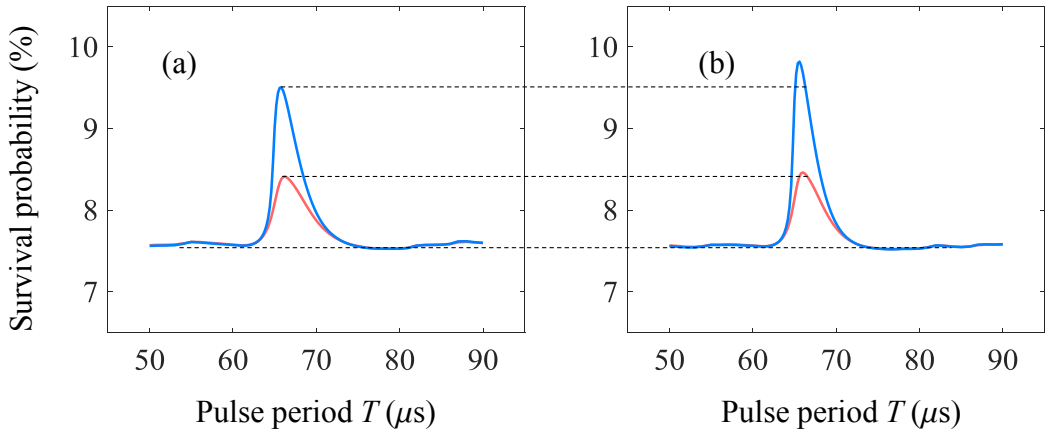

Figure 7.4: The numerical calculation of the survival resonances with (blue lines) and without (red lines) the feedback processes. (a) The nodes has a finite intensity due to the imbalance of the two light beams. (b) The standing wave is perfectly balanced with dark nodes. The black dashed lines are the eye-guide for comparing the peak height.

In the experiment, the nodes of the standing wave formed by retro-reflecting a laser beam are not completely dark due to the intensity loss of the retro-beam. This may lead to a lower survival since the atom will have a finite chance to scatter photons and decay to the dark state. It is therefore interesting to investigate the performance when having perfectly dark nodes. Due to the experimental limitation, we check the effect of using balanced standing wave theoretically.

The blue lines in Fig. 7.4 show the feedback enhanced survival resonance with imbalanced (a) and balanced (b) standing wave, where the red lines are the resonance peaks

without feedback sequence for comparison. We observe a 20% growth of the peak height when using a balanced standing wave, which is a marginal improvement. It therefore means that the imbalance of the standing wave is not the main limitation for the peak height in the present experiment.

7.4.2 Evolution with τ_1

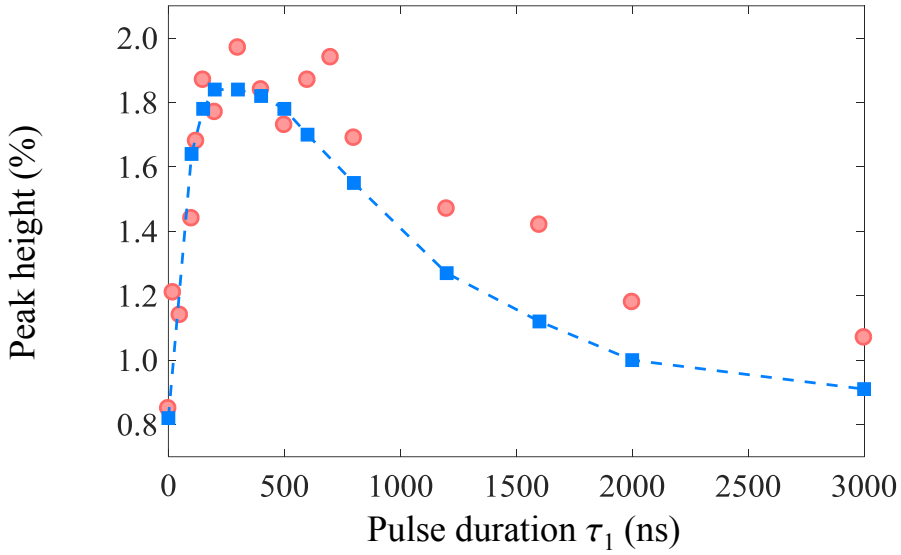

Figure 7.5: Feedback enhanced peak height as a function of the pulse duration τ_1. Red circles and blue squares are the measured and calculated peak height, respectively. The blue dashed line is an eye-guide connection line. The survival resonances are acquired at the first Talbot time with $N_1 = 5$ pulses.

For a given probe sequence, a natural question to ask is what is the ideal pulse duration (of the standing wave pulses during the feedback procedure) that allows for a maximum survival enhancement. To understand the relation between the peak height of the enhanced resonances and the pulse duration τ_1, we measure the survival probability while varying τ_1 after an experimental sequence shown in Fig. 7.1(b), with $N_1 = 5$.

Figure 7.5 displays the peak height as a function of τ_1, where the height is obtained from the two-piece normal distribution fitting curve. It shows that the peak height increases

when $\tau_1 < 300$ ns and decreases for $\tau_1 > 300$. The calculation (blue squares) shows a good agreement to the measurements (red circles).

The trend shown in Fig. 7.5 is not surprising since the maximum survival results from a trade-off between two competing effects. One is preserving atoms that are in the long surviving modes; the other is to remove atoms that are not in the long surviving modes to the reservoir such that they get a second chance to populate a long surviving mode. When τ_1 is small, the modulation depth due to the standing-wave pulse is low and the atoms survive regardless of being in long surviving modes or not. The standing-wave pulse fails to remove atoms not in the long surviving modes, which eliminates the chance for the atoms to get a second opportunity to be in a long surviving mode. We thereby see a low peak for small τ_1. On the other hand, when τ_1 is large, the atoms cannot survive the pulses regardless their states, since the modulation depth of the standing-wave pulse is too high. Each pulse therefore removes all the atoms to the reservoir and initiates the process entirely, where no atoms are stored in long surviving modes. We therefore see a small peak for large τ_1 as well.

The maximum peak height therefore occurs as a compromise between these two effects, which is $\tau_1 = 300$ ns for the current parameter combination (see Fig. 7.5).

7.4.3 Evolution with N_1

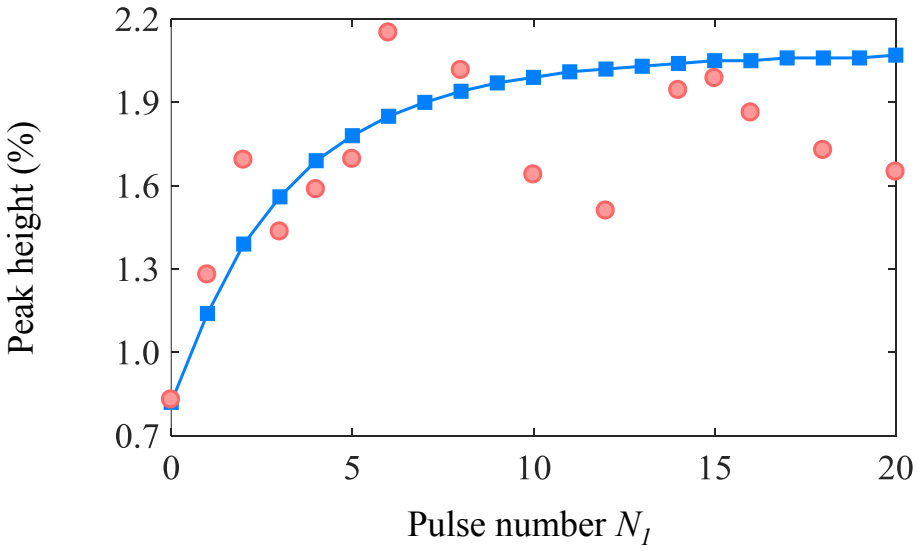

Figure 7.6: Feedback enhanced peak height as a function of the pulse number N_1. The red circles and blue squares are the measured and calculated peak height, respectively.

For the same probe sequence used in Fig. 7.5, we now study the dynamical behavior of the feedback procedure by varying the pulse number N_1, with $\tau_1 = 400$ ns and $T = T_{\mathrm{T}}$. Figure 7.6 displays the peak height as a function of N_1. The red circles and blue squares are the measured and calculated data, respectively. The peak height increases until N_1 is about 10. In Fig. 7.6, we see that the measured data is noisy. Nevertheless, the calculation still captures the trend of the measurements, and they show a reasonable agreement.

In Fig. 7.6, we see an initial increasing of the peak height for small N_1 values. This rising trend can be understood as follows. When N_1 is small, the atoms survive even if are not in the long surviving modes. They therefore do not have a chance to be corrected to such modes, and will be removed to the dark state by the probe sequence. We thereby see a small peak for lower N_1 values, which will increase along with N_1.

After many pulses during the feedback stage, the system reaches a steady state. The number of the atoms removed to the dark state by the standing wave pulse is same as the

number of the atoms transferred back to the initial state by the recycle light. Each cycle (formed by standing wave pulse and subsequent recycle light) leaves the atom number in the long surviving modes unchanged. Once the system reaches this point, the growth of the peak height becomes 0.

7.5 Discussions and conclusion

There is an advantage of using the F = 2 ground state as the initial state. When driving the F = 2 to F′ = 3 transition, there is no dark state in the F = 2 manifold and therefore no need for applying a magnetic quenching field. This leads to the suppression of unwanted magnetic noise caused by the quenching magnetic coils.

To conclude, we have studied the enhanced survival resonances when applying a feedback stage. During this process, the standing wave light pulses and recycle light continuously correct the atoms into the long surviving modes. The maximum improvement of the peak height comes as a trade-off between two competing effects, which are removing atoms out of the long surviving modes and preserving the atoms in such modes. The growth of the peak height ceases once the system reaches a steady state.

The enhanced resonances give sharper and higher peaks than the conventional survival signal. Moreover the improvement of the signal size reaches a saturation within half millisecond, which is neglectable compared to the entire experimental sequence. The method for feeding atoms to the long surviving modes can therefore improve the sensitivity of the measurement, which provides a tool for increasing the measurement precision based on the method presented in the thesis.

Chapter 8

Gravity measurements using survival resonances

This chapter will investigate an atomic gravimeter that exploits the survival resonances described in Chapter 6. For the purpose of sensing the gravitational field, the atoms interact with a vertically arranged standing wave (parallel to the local gravitational acceleration g). Gravity removes the survival resonances since it adds extra phases during the evolution between the light pulses. However, effectively accelerating the standing-wave interference pattern can make it co-move with the free falling atoms. This leads to the reemergence of the survival resonances, which can be used to deduce the local g-value.

The chapter is heavily based on the paper [51] that is conditionally accepted, which requires minor corrections. It begins with a brief description of the experimental procedure, and then studies the survival resonances in the presence of the local gravitational field. Additionally, it presents the evolution of the height and width of the resonances that emerge as a function of the standing-wave acceleration a. This is used for searching for an appropriate parameter combination. Finally, it presents a measurement of g reaching a precision of 5 ppm by interrogating over a drop distance less than 1 mm, and also gives

a brief discussion of the potential limitation of this technique. The last section provides the conclusion.

8.1 Survival resonances in the presence of gravity

This section studies how the survival probability of the atom evolve when the standing wave acceleration a is swept. Similar to Chapter 6, we again use the F = 3 (or 2) hyperfine ground state of the ^{85}Rb atoms as the initial (dark) ground state. The standing-wave light is formed by counter-propagating two light beams with the intensity of 15 mW/cm^2, and is 10 MHz red detuned to the open atomic transitions from F = 3 to F$'$ = 2. The pulse sequence has $N = 5$ pulses with a duration of $\tau = 400$ ns. These parameter are the same in the present chapter unless otherwise stated.

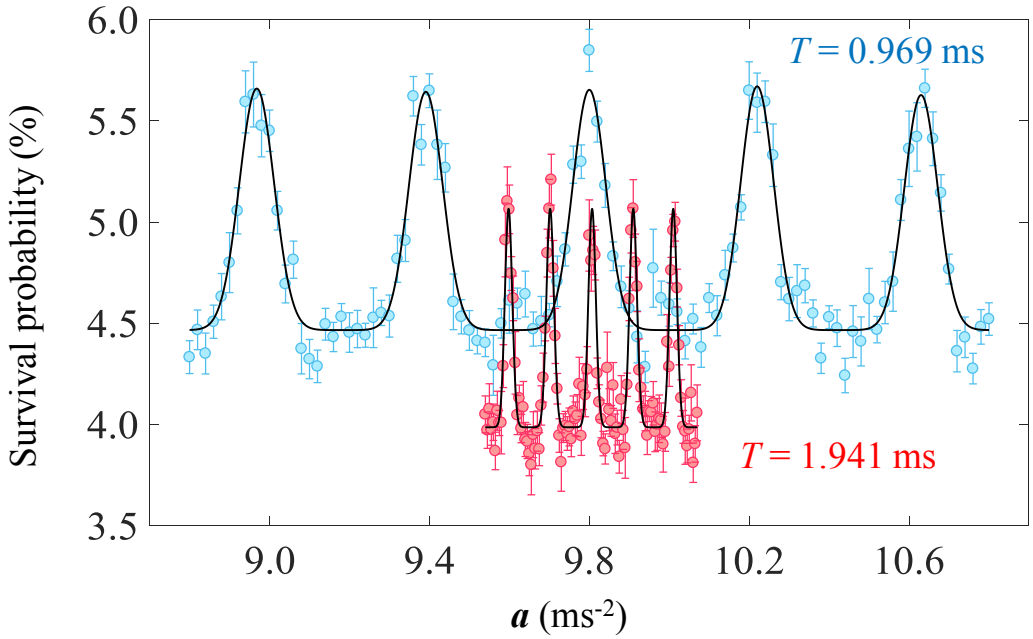

Figure 8.1: The measured survival probability as a function of the standing-wave acceleration a, for pulse period T=0.969 ms (blue markers: $15T_{\mathrm{T}}$) and 1.941 ms (red markers $30T_{\mathrm{T}}$). The markers are the average of 20 experimental runs and the error-bars show the standard deviation of the mean. The solid black lines are the fitting curves with five Gaussian peaks.

Figure 8.1 displays two data series as a function of a for $T = 0.969$ ms ($15T_{\mathrm{T}}$, blue circles) and 1.941 ms ($30T_{\mathrm{T}}$, red circles). In both data sets, a peak appears when a matches g. The black lines are the fits with a sum of five Gaussian functions that share the same peak height, width, and offset. The peak position of each Gaussian function is a free parameter. The peak position of the central Gaussian yields the local g-value.

We can conceptually explain the survival resonances shown in Fig. 8.1 as follows: when the evolution between the light pulses includes gravity, the self-image [see Fig. 3.3(c)] does not align with the subsequent standing wave, since the atoms accelerate. Nevertheless, by moving the standing-wave interference pattern spatially such it matches the self-image, the survival resonance re-emerges. Equation 3.23 shows that the second exponential term will suppress the atomic survival when $a \neq g$, while it becomes the identity operator when $a = g$.

An interesting feature of the resonances shown in Fig. 8.1 is that the survival resonances not only appear for $a = g$ but also occur when:

$$a = g + j\frac{\lambda}{2}\frac{1}{T^2}, \tag{8.1}$$

where $j \in \mathbb{Z}$ and $\lambda/2$ is the spatial period of the standing wave. To understand this, we consider the initial atomic cloud as an incoherent sum of plane-waves, and apply a pulse at $t = (n'-1)T$ to the atomic waves. The spatially periodic standing wave in combination with the Bloch's theorem ensures that the atomic state originating from the plane wave $|p_0\rangle$ has the form of $\sum_m c_m[t = (n'-1)T]|p_0 + 2m\hbar k_L\rangle$, where p_0 is the initial momentum and $c_m[t = (n'-1)T]$ denotes the time-dependent amplitude of the m-th diffraction order (where $m \in \mathbb{Z}$). Applying the free evolution operator $\widetilde{\widetilde{F}}_{n'}$ in Eq. 3.23 on this state from

$(n'-1)T$ to $n'T$ yields:

$$\begin{aligned}
&\tilde{\tilde{F}}_{n'}\sum_m c_m[t=(n'-1)T]|p_0+2m\hbar k_L\rangle \\
&=\exp\left(-\frac{i}{\hbar}\frac{p^2}{2M}T\right)\exp\left(\frac{i}{\hbar}\left[\frac{p\,(g-a)}{2}\left(2n'-1\right)\right]T^2\right)\sum_m c_m[t=(n'-1)T]|p_0+2m\hbar k_L\rangle \\
&=\exp\left(-\frac{i}{\hbar}\frac{\left(p_0+2m\hbar k_L\right)^2}{2M}T\right)\exp\left(\frac{i}{\hbar}\left[\frac{\left(p_0+2m\hbar k_L\right)(g-a)}{2}\left(2n'-1\right)\right]T^2\right) \\
&\quad\times\sum_m c_m[t=(n'-1)T]|p_0+2m\hbar k_L\rangle.
\end{aligned} \tag{8.2}$$

Inserting $T=\ell T_{\mathrm{T}}/2$ ($\ell\in\mathbb{Z}$) and a in Eq. 8.1 into Eq. 8.2, we have:

$$\begin{aligned}
&\exp\left(-\frac{i}{\hbar}\frac{4p_0\hbar k_L m+4m^2(\hbar k_L)^2}{2M}\ell\frac{T_{\mathrm{T}}}{2}\right)\exp\left(-\frac{i}{\hbar}\left[\frac{(2m\hbar k_L)}{2}j\frac{\pi}{k_L}\left(2n'-1\right)\right]\right) \\
&\quad\times\sum_m c_m[t=(n'-1)T]|p_0+2m\hbar k_L\rangle \\
&=\exp\left(-\frac{i}{\hbar}\frac{p_0\hbar k_L m+m^2(\hbar k_L)^2}{M}\ell\frac{\pi M}{\hbar k_L^2}\right)\exp\left(-i\left[mj\left(2n'-1\right)\right]\pi\right) \\
&\quad\times\sum_m c_m[t=(n'-1)T]|p_0+2m\hbar k_L\rangle \\
&=\exp\left(-i\pi\left[m^2\ell+m\left(\frac{p_0}{\hbar k_L}+j\left(2n'-1\right)\right)\right]\right)\sum_m c_m[t=(n'-1)T]|p_0+2m\hbar k_L\rangle.
\end{aligned} \tag{8.3}$$

where $\lambda=2\pi/k_L$, and we have omitted a global phase that is independent of m. From this we see that the effect of an integer j is equivalent to a shift of the initial momentum p_0 with amount of $j\hbar k_L$. Since the survival probability is averaged over a broad initial momentum distribution, there is no net effect from shifting it and a survival resonance equivalent to $j=0$ emerge for all $j\in\mathbb{Z}$. When j is a fractional number, p_0 becomes pulse number n' dependent, which leads the resonant survival being wiped out by different pulses.

8.2 The resonance's dependence on experimental parameters

A leading motivation of this chapter is to understand the behavior of survival resonances as a function of the standing-wave acceleration a with different experimental parameters. To this end, we performed a series of experiments by studying the incisiveness and height of the resonances as a function of several variables. Note that we acquire the resonant peaks as a function of a by using the specific T-values that allow for an observable survival resonance (see Fig. 6.2). Figures 8.2, 8.3 and 8.4 show the width (and height in one case) as a function of light detuning, intensity, pulse number and pulse interval, respectively. The width and height are obtained by fitting a Gaussian to the measured (or calculated) data around the central peak shown in Fig. 8.1.

8.2.1 Strength of interaction

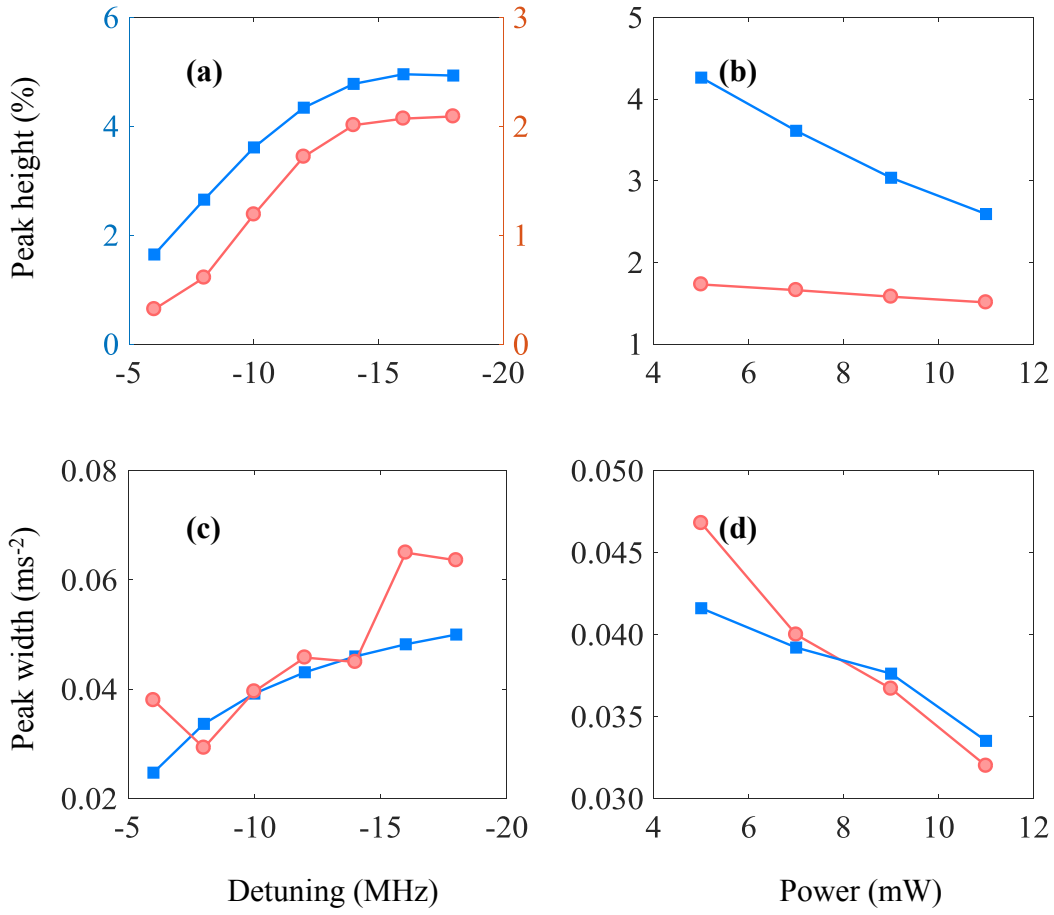

Figure 8.2: Measured (red circles) and calculated (blue squares) peak height (a and b) and peak width (standard deviation σ) (c and d) as a function of the laser detuning (a and c) and power (b and d) of the standing wave. The pulse period T is at the 15^{th} Talbot time.

In this sub-section, we investigate the dynamics of the system as a function of the light intensity and detuning of the standing wave, which are the two parameters of alternating the atom-light interaction. When the strength of this interaction increases, the survival resonance peak as a function of a becomes narrower, but lose height.

Figure 8.2 (a and c) show growing trends of the height and the width when the standing-

wave light detuning increases. However, when the detuning exceeds 14 MHz, the photon scattering rate at the anti-nodes of the standing wave is insufficient to remove all atoms. The growth in the peak height thereby ceases. If the detuning is increased further the system approach a standard AODKR, where there are no dissipation embedded in the standing wave since the photon scattering rate is negligible (see Eq. 2.35). The atoms thereby survive regardless their position and the survival resonances vanish. When changing the optical power of the standing wave, Fig. 8.2 (b and d) shows that the height and width decrease with increasing intensity. This is not surprising since stronger intensity leads the atoms to scatter more photons and go to the dark state with a higher efficiency.

In Fig. 8.2 (a and b), the trends of experimental data and the calculation agree but the experimental data shows a smaller peak height. This is because we use relative long pulse period, and as shown in Fig. 6.2, the data displays a decay of the peak height that is not captured by the calculation.

8.2.2 Number of pulses

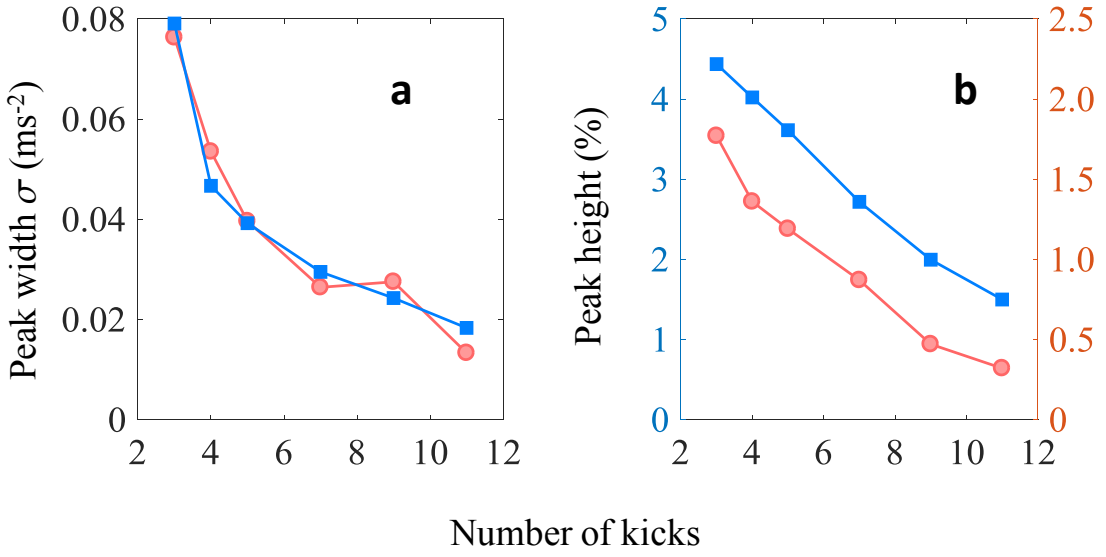

Figure 8.3: Measured (red circles) and calculated (blue squares) peak width(a) and height(b) as a function of the pulse number N. (b) The left y-axis is for calculated data, while the right y-axis is for measured data. The pulse period T is at the 15^{th} Talbot time.

To further understand the dynamics of the system, we now study how the survival resonance peak evolve with the pulse number N. In Fig. 8.3(a), both experiment and calculation show that the peak width becomes narrower when the number of the standing wave pulses (N) increase. This monotonic trend can be understood since a higher N causes a population of higher diffraction orders that accumulate phase at higher rates during the free evolution. This therefore requires a to be close to g to guarantee that different diffraction orders are in phase at the application of the subsequent pulses. For the peak width as a function of T rather than a, Fig. 6.8 shows a similar decrease trend. Furthermore, increasing N increases the total interrogation time.

Figure 8.3(b) shows a decline trend of the peak height when increasing the pulse

number N since there is a finite probability for photon scattering even when close to the standing wave nodes. A similar trend can be seen in Fig. 6.6 where the peak height is a function of the pulse period T.

8.2.3 Pulse period

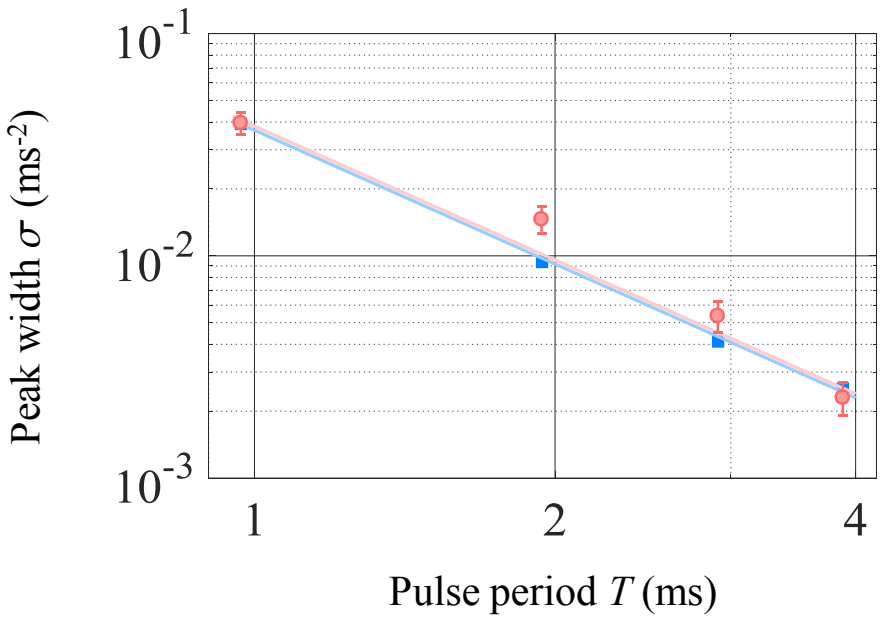

Figure 8.4: Measured (red circles with error-bars) and calculated (blue squares) peak width as a function of pulse period T. The error-bars of the measured data represent one standard deviation confidence interval for the Gaussian fitting to the survival resonant peaks. The blue (or red) curve is a scaling law to the calculated (or measured) data with a fixed power value of -2.

In an interferometer, it is natural to improve the measurement sensitivity by increasing the overall interrogation time [26]. This can be directly seen in Fig. 8.1 that displays a narrower peak when increasing T. We therefore turn the attention to how the survival resonance peak evolves when extending the pulse period T.

Figure 8.4 displays the measured (red circles) and calculated (blue squares) peak width when varying the pulse period T from the 15-th to the 60-th Talbot time. The monotonic

decrease can be understood from Eq. 3.23. The second term, which is responsible for the peak, contains the product of $g - a$ and T^2. The width should therefore display a scaling law as a function of T with the power of -2. The solid lines in Fig. 8.4 are fits to the calculation (blue curve) and measurement (red curve) with a T^{-2} law. We see that the fitted curves capture the data reasonably well. Classical physics conceptually explains the T^{-2} dependence, since the position of a free falling atom is proportional to the square of the fall time.

It is worth mentioning that when varying T, the decay of the peak height is minimal (data not shown). This is not surprising since the strength of the atom-light interaction and the pulse number are fixed. Consequently, increasing the pulse period provides a way of getting a high sensitivity (narrow width) without losing signal size (peak height).

8.3 Measurement of g and discussion

While our present apparatus is not optimized for precision measurements, it is interesting to estimate if it is feasible to reach a precision in μGal regime which would make it of great interest for geoscience applications. In this section, we carry out a measurement of g and discuss how it can be improved.

8.3.1 Measurement of g

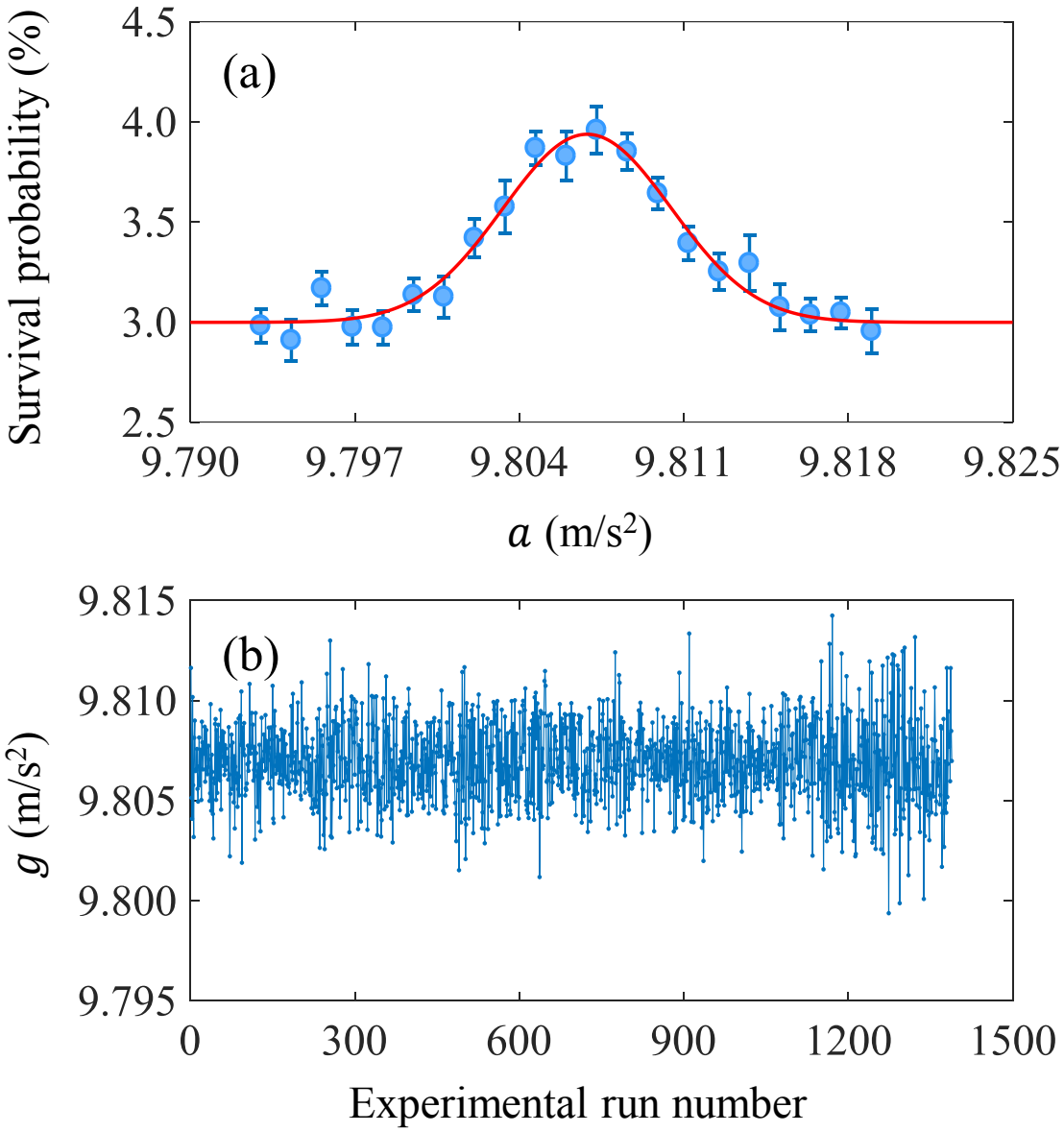

Figure 8.5: The measurement of g. (a) A survival resonance peak against a that is similar to Fig. 8.1 but with pulse separation T=3.882 ms ($60T_{\mathrm{T}}$). The red line is a Gaussian fitting for extracting the g-value. (b) A continuous measurement of g over about 1400 repetitions.

To measure g we first map out the survival resonance using $T = 3.882$ ms (60^{th} T_{T}), $N = 5, \tau = 400$ ns, $\Delta/2\pi = -10$ MHz to F = 3 to F$' = 2$ transition and an intensity of

each standing wave beam of 15 mW/cm^2. Figure 8.5(a) displays the measured data and we fit it with a Gaussian function. We then employ a standard protocol for performing high-rate measurement by taking data on the maximal slopes on each side of the fringe [21]. About 1400 repetitions yields a g-value of 980710(5) mGal (corrected for a present angle of $\theta = 3.3$ mrad between the standing wave and the direction of the gravitational force) [shown in Fig. 8.5(b)].

8.3.2 Discussions

The uncertainty of 5 mGal achieved above is insufficient for many geophysics applications. However, it is virtually the same performance of the first proof-of-principle atomic interferometer based on stimulated Raman transitions using a similar drop distance [19]. Subsequent development has proven that Raman-interferometry is a feasible method for reach a precision in the sub-μGal regime [23]. Now I would like to discuss how to achieve a similar improvement in our atomic interferometer.

The experiment presently uses a 1 mm fall distance. However, by going to a fountain geometry of 10 cm height, we will obtain a 300 fold reduction of the uncertainty due to the narrowing of the peak with T (see Fig. 8.4) [19, 20]. Implementing atomic shot-noise limited detection and increasing the atom number from the present $\sim 10^5$ to above 10^6 should give further improvement of more than an order of magnitude [135]. Additionally, feeding the lost atoms back to the system can improve the signal-to-noise by another factor of more than 2 (see Chapter 7).

For a 10 cm height fountain geometry, the free dropping takes about 300 ms to complete. After the detection, we recycle the atoms from the previous run and use them for the subsequent experiment [136], which generally takes around 50 ms. Consequently, the time scale of the measurements is approximately 350 ms for each shot. 1400 repetitions can therefore be accomplished within 10 min that is a typical averaging time for CG-5 spring-based gravimeter to reach a precision of ~ 10 μGal.

The error given in the measurements is the standard deviation of the mean [137], which could improve with $1/\sqrt{N}$ (with N the number of measurements). Taking more data by repeating the experiments can therefore lead the precision to further improve by $\sqrt{N}$.

Since we use near resonant light for the standing wave, the presence of the atoms affects the wavelength of the standing wave light by changing the index of refraction. This effect is negligible compared to our present uncertainty. But it will need to be considered in improved measurements. The method to evaluate the change of the refractive index is outlined in Ref. [138]. Similar to other kinds of atomic gravimeters, the effects of Coriolis force, gravity gradients, wavefront distortions and so on, will also impact the results and need to be corrected in a similar manner as done in [22].

8.4 Summary

This chapter presented a proof-of-principle atomic gravimeter through measuring the survival resonances in the presence of the gravitational field. We studied the dependences of the peak height and width against a variety of experimental parameters, and found a good parameter combination that gives a high sensitivity for the current apparatus. With this setting, we demonstrated a measurement of g reaching a precision of 5 ppm with a drop distance of less than 1 mm. Finally, we briefly discussed the potential limitation of this technique.

Chapter 9

Conclusions and Future work

9.1 Conclusions

Light-pulse atom interferometry is a fast developing field and the ambition of making portable devices has never failed to attract attention in the atomic physics community. The thesis provides a method based on survival resonances that may allow for the construction of relatively low cost, compact, but high precision atomic gravimeters.

The thesis has presented the survival resonances and their applications. In an atom-optics system driven by the temporally and spatially periodic dissipation, the survival resonances emerge as a result of the matter-wave Talbot-Lau interference. For short pulse periods, the four-level model gives an excellent agreement between experiments and calculations, without any fitted parameters. For long pulse periods, the measured resonant peaks show a reduction of the peak height that the model fails to capture. Nevertheless, the model can predict the width well.

A. The survival resonances

The three critical findings for survival resonances are:

- Exposing the atoms to a horizontal standing-wave light pulses (or to a pulsed

standing-wave light that effectively accelerates with the local gravitational acceleration g), the system displays a series of survival resonances as a function of the pulse period T, which are separated by half the Talbot time $T_{\mathrm{T}}/2$.

• The standing-wave light pulse simultaneously acts as a phase and an amplitude grating for the atomic wave function. The phase modulation leads to a micro-lensing effect that results in a high and asymmetric resonant peak.

• The width of the survival resonances displays a sub-Fourier scaling law with increasing the pulse number.

B. The applications using survival resonances

The two applications based on the survival resonances are:

• Feeding back lost atoms results in an enhancement of the survival resonances and therefore better use of resources. The enhanced resonant signal may find the application in precision measurements.

• With a vertically arranged standing-wave light, varying its effective acceleration a reveals a series of survival resonances, from which we can accurately deduce the local gravitational acceleration g. A proof-of-principle atomic gravimeter achieves a precision of 5 ppm with a drop distance less than 1 mm. The present results indicate that with an appropriate design and a fountain geometry of 10 cm height, we will reach a precision in a unit of μGal with an averaging time of few minutes.

9.2 The future work

There are several technical advantages of using survival resonances for an atomic gravimeter. The standing-wave light is near resonant, which allows for deriving the light from the same laser used for cooling atoms, making the laser system requirement simple. Meanwhile, the strong atom-light interaction of near-resonant light gives a low optical intensity

requirement. Additionally, the Talbot-Lau effect facilitated survival resonances allow for their observations by using a thermal atomic source, making the cooling stages simple and short. Furthermore, the internal state detection and the ability to recycle the atoms from the previous run can give high repetition rates. The method of using survival resonances may therefore be of interest for a low cost and compact absolute atomic gravimeter.

The future work based on the findings in this thesis is to construct a portable absolute atomic gravimeter with a precision in the μGal regime. Additionally, it will be of interest to apply the feeding-back mechanism to further improve the sensitivity of the measurement. The easy implementation and low requirements on the laser system may allow such technique to have the potential to cut down the price of the present atomic gravimeters.

Appendix A

MATLAB code

This appendix provides the MATLAB code that simulates the dynamics of the system described in Chapter 3. Figure A.1 shows the programming environment of MATLAB (R2016b).

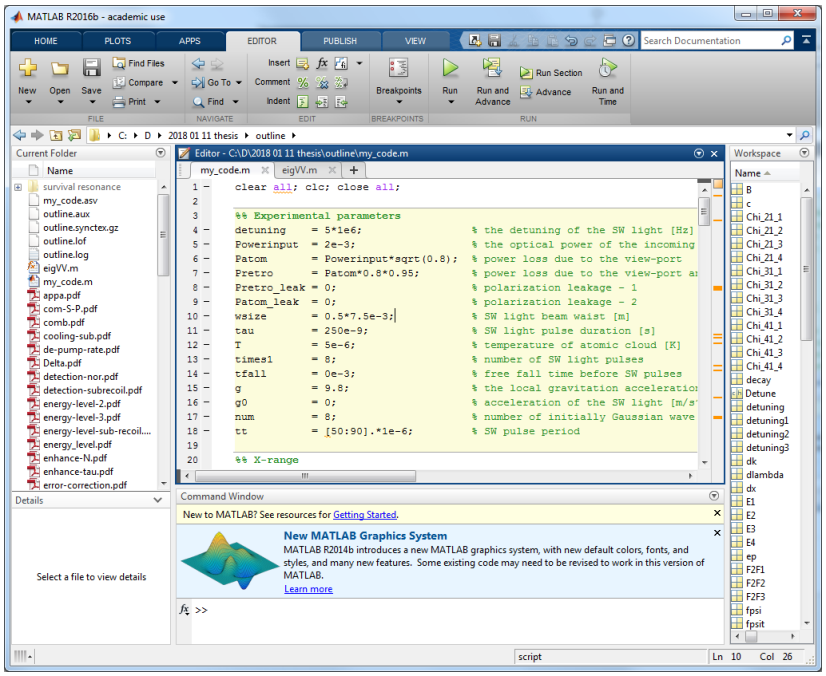

Figure A.1: The MATLAB environment.

We use a combination of the main program with a function. The main program defines

the fundamental physical constants and experimental parameters, calculates the survival probability, and saves the outcomes of the simulation. While the function computes the grating operator.

A.1 Main program

```
clear all; clc; close all;

%% Experimental parameters
detuning     = 5*1e6;                  % the detuning of the SW
    light [Hz]
Powerinput   = 2e-3;                   % the optical power of the
    incoming laser beam [W]
Patom        = Powerinput*sqrt(0.8);   % power loss due to the
    view-port
Pretro       = Patom*0.8*0.95;         % power loss due to the
    view-port and retro-mirror
Pretro_leak  = 0;                      % polarization leakage - 1
Patom_leak   = 0;                      % polarization leakage - 2
wsize        = 0.5*7.5e-3;             % SW light beam waist [m]
tau          = 400e-9;                 % SW light pulse duration [
    s]
T            = 5e-9;                   % temperature of atomic
    cloud [K]
times1       = 5;                      % number of SW light pulses
tfall        = 0e-3;                   % free fall time before SW
    pulses
```

```
15 g            = 0;                    % the local gravitation
       acceleration [m/s^2]
16 g0           = 0;                    % acceleration of the SW
       light [m/s^2]
17 num          = 8;                    % number of initially
       Gaussian wave packets
18 tt           = [50:90].*1e-6;        % SW pulse period
19
20 %% X-range
21 dx           = 1e-8;                 % x-axis resolution
22 L            = 4e-4;                 % x-axis range
23 N            = (L+dx)/dx;
24 x            = linspace(-1/2,1/2,N)*L;
25
26 %% Fundamental Physical Constants
27 hbar         = 1.054571628e-34;      % Planck's Constant
28 c            = 2.99792458e8;         % speed of light in vacuum
29 kb           = 1.3806504e-23;        % Boltzmann's Constant
30 ep           = 8.854e-12;            % Permittivity of Vacuum
31 m            = 1.409993199e-25;      % the mass of Rb-85 atom
32 sigma        = hbar/sqrt(2*m*kb*T);  % width of the Gaussian
       wave packets
33
34 %% Four electric fields
35 Iatom        = 2*Patom/pi/wsize^2;
36 E1           = sqrt(2*Iatom/c/ep);
```

```
37 Iretro    = 2*Pretro/pi/wsize^2;
38 E2        = sqrt(2*Iretro/c/ep);
39 Iretro_l  = 2*Pretro_leak/pi/wsize^2;
40 E3        = sqrt(2*Iretro_l/c/ep);
41 Iatom_l   = 2*Patom_leak/pi/wsize^2;
42 E4        = sqrt(2*Iatom_l/c/ep);
43
44 %% standing-wave light frequency
45 freq      = 384.230406373e12 + 1.7708439228e9 - 20.435e6;
46 lambda    = c/freq;
47 k1        = 2*pi/lambda;
48 decay     = 2*pi*6.0666e6;          % decay rate [Hz]
49
50 %% dipole matrix elements for F=2 to excited states
51 JerJ      = 3.58425e-29;            % D2 line transition dipole
       matrix element
52 F2F1      =      [0              sqrt(3/20)     sqrt(1/5)     sqrt
       (3/20)     0           ];
53 JerJ1     = mean(F2F1)*JerJ;
54 F2F2      = abs([-sqrt(7/27) -sqrt(7/108)  0              sqrt
       (7/108)    sqrt(7/27)]);
55 JerJ2     = mean(F2F2)*JerJ;
56 F2F3      = abs([-sqrt(2/27) -sqrt(16/135) -sqrt(2/15)  -sqrt
       (16/135) -sqrt(2/27)]);
57 JerJ3     = mean(F2F3)*JerJ;
58
```

```
59 detuning1 = 2*pi*(detuning + 63.401e6 + 29.372e6);
60 detuning2 = 2*pi*(detuning + 63.401e6);
61 detuning3 = 2*pi*detuning;
62 M1         = hbar*detuning1+i*hbar*decay/2;
63 M2         = hbar*detuning2+i*hbar*decay/2;
64 M3         = hbar*detuning3+i*hbar*decay/2;
65
66
67 Chi_21_1   = JerJ1.*E1./hbar;
68 Chi_21_2   = JerJ1.*E2./hbar;
69 Chi_21_3   = JerJ1.*E3./hbar;
70 Chi_21_4   = JerJ1.*E4./hbar;
71
72 Chi_31_1   = JerJ2.*E1./hbar;
73 Chi_31_2   = JerJ2.*E2./hbar;
74 Chi_31_3   = JerJ2.*E3./hbar;
75 Chi_31_4   = JerJ2.*E4./hbar;
76
77 Chi_41_1   = JerJ3.*E1./hbar;
78 Chi_41_2   = JerJ3.*E2./hbar;
79 Chi_41_3   = JerJ3.*E3./hbar;
80 Chi_41_4   = JerJ3.*E4./hbar;
81
82 step   = 0;
83 tic
84
```

```
85 %% Cycle for each dT pulse separation
86 % defining initial wavepackets for all atoms
87 dlambda     = lambda/(2*num);
88 position    = -lambda/4:dlambda:lambda/4-dlambda;
89 psinew      = 1/sqrt(sqrt(pi*sigma^2)).*exp(-(repmat(x,length(
       position),1).'-repmat(position,length(x),1)).^2/2/sigma^2);
90 B           = 1./sqrt(sum(abs(psinew).^2*dx));
91 psinewn     = bsxfun(@times,B,psinew);
92 % Fourier transfer [from position to momentum space]
93 dk          = 2*pi/(L+dx);    % fft [from position space to k
       space]
94 k           = ([1:N]-1)*dk;
95 fpsi        = fftshift(1/sqrt(2*pi).*fft(psinewn)*dx,1);
96 nk          = [-floor(N/2):floor(N/2)]*dk;
97 part1       = (hbar.*nk).^2/2/m*(tfall);
98 part2       = -g/2*hbar.*nk*(tfall^2);
99 Ft          = exp(-1i/hbar.*(part1+part2)).';  % time evolution
       operator
100 zzz        = bsxfun(@times, Ft,fpsi); temp=((1/sqrt(2*pi)*N)*dk*
       exp(-1i*pi*(N-1)/N.*([1:N]-1)).*exp(-1i/hbar*m*g.*x*tfall))
       .';
101 % Inverse Fourier transfer [back to position space]
102 psif        = bsxfun(@times,ifft(zzz),temp);
103 tmp         = psif;           % initial wave packets
104
105 %% Perform the evolution of the system
```

```
106 output      = zeros(length(tt),1);
107 w_sweep     = g0*k1/2;          % linearly chirping the frequency
        difference of the SW
108 t2          = 0;
109
110 % use 'eig'-Function to find the 'grating operator' G
111 % G only needs to be calculated once in the entire sequence
112 [G]         = eigVV( x,k1,w_sweep,t2,tau,Chi_21_1,Chi_21_2,
        Chi_21_3,Chi_21_4,Chi_31_1,Chi_31_2,Chi_31_3,Chi_31_4,
        Chi_41_1,Chi_41_2,Chi_41_3,Chi_41_4,M1,M2,M3);
113
114 % for a particular pulse period
115 show        = [1:10:length(tt)];
116
117 for j = 1:length(tt)
118     if j == show(find(show==j))
119         disp([num2str(j) ' / ' num2str(length(tt))]) % cycle
                counter
120     end
121     psif = tmp;
122         %% Applying the SW pulse in position space
123         for n = 1:1:times1
124             t1 = n*tt(j) + tfall;
125             t2 = (n-1)*tt(j) + tfall;
126             Udagger = (G.*exp(1i/hbar*m*g.*x*t2)).';
127             fpsit = bsxfun(@times, psif,Udagger);
```

```
128
129             %% FFT transfer wave-function from position space to
                    momentum space
130             fpsi  = fftshift(1/sqrt(2*pi).*fft(fpsit)*dx,1);
131             %% free evolution between pulses
132             part1 = (hbar.*nk).^2/2/m*(t1-t2);
133             part2 = -g/2*hbar.*nk*(t1^2-t2^2);
134             Ft    = exp(-1i/hbar.*(part1+part2)).';
135             zzz   = bsxfun(@times, Ft,fpsi);
136             temp  = ((1/sqrt(2*pi)*N)*dk*exp(-1i*pi*(N-1)/N
                    .*([1:N]-1)).*exp(-1i/hbar*m*g.*x*t1)).';
137
138             %% IFFT transfer wave-function back to position
                    space
139             psif=bsxfun(@times,ifft(zzz),temp);
140         end
141     step          = step+1;
142     output(step) = sum(sum(abs(psif).^2*dx))/num;  % survival
        probability for the specific pulse period
143 end
144 toc
145
146 %% Plotting the results
147 figure(1)
148         format long
149         height = (max(output)-min(output))          % print out
```

```
                the peak height of the survival resonance
150             T       = tt(find(output==max(output)))*1e6 % print out
                the peak position of the resonant peak
151             plot(tt*1e6,output,'o-','Color',[0 0.5 0]);
152             hold on;
153             xlabel('dT (\mus)')
154             ylabel('survival probability in F=2')
155             set(gcf,'Position',[105 450 400 300])
156
157 figure(2)
158             plot(x.*1e3,abs(psif(:,end)).^2)
159             xlabel('X coordinate (mm)'); ylabel('|\psi|^2')
160             set(gcf,'Position',[105 50 400 300])
161
162 %% save the result of the calculation
163 Npulse  = num2str(times1);
164 Tau     = num2str(tau*1e9);
165 Power   = num2str(Powerinput*1e3);
166 Detune  = num2str(detuning/1e6);
167 % Tfall   = num2str(tfall*1e3);
168 % DTTT    = num2str(TTT);
169 outfile = ['SR-' Npulse 'x' Tau 'ns-' Detune 'MHz-' Power 'mW-
      imbalanced-4level.mat'];
170 save(outfile,'tt','output');
```

The code presented above gives the program for finding the resonant pulse period T (see for example Fig. 6.1). Instead of scanning T, varying the standing wave acceleration

$\boldsymbol{a}$ will reveal a set of survival resonances similar to Fig. 8.1.

A.2 Function for grating operator

MATLAB defines functions in separate files. The code presented in this section uses a built-in function "eig" to compute the eigenvalues and corresponding eigenvectors [1] of the system Hamiltonian described in Chapter 2.

```
1 function [ cg ] = eigVV( x,k1,w_sweep,t2,tau,Chi_21_1,Chi_21_2,
    Chi_21_3,Chi_21_4,Chi_31_1,Chi_31_2,Chi_31_3,Chi_31_4,
    Chi_41_1,Chi_41_2,Chi_41_3,Chi_41_4,M1,M2,M3);
2 %  This function computes the grating operator G
3 %  A four-level model gives the full description of the
    dynamics
4
5
6 hbar = 1.054571628e-34;       % Planck's Constant
7
8 for x_index = 1:length(x);
9
10      phase_down = exp(-i*k1*x(x_index)-i*w_sweep*t2^2);
11      phase_up   = exp(+i*k1*x(x_index)+i*w_sweep*t2^2);
12
13      V12        = -1/2*hbar*conj(Chi_21_1)*phase_down - 1/2*hbar*
            conj(Chi_21_2)*phase_up ...
```

[1] $[V, D] = \mathrm{eig}(A)$ produces a diagonal matrix D of eigenvalues and a full matrix V whose columns are the corresponding eigenvectors so that $AV = VD$.

```
14                  -1/2*hbar*conj(Chi_21_3)*phase_down - 1/2*hbar*
                        conj(Chi_21_4)*phase_up  ;
15      V21         = -1/2*hbar*Chi_21_1*phase_up - 1/2*hbar*Chi_21_2*
            phase_down ...
16                  -1/2*hbar*Chi_21_3*phase_up - 1/2*hbar*Chi_21_4*
                        phase_down;
17
18      V13         = -1/2*hbar*conj(Chi_31_1)*phase_down - 1/2*hbar*
            conj(Chi_31_2)*phase_up ...
19                  -1/2*hbar*conj(Chi_31_3)*phase_down - 1/2*hbar*
                        conj(Chi_31_4)*phase_up;
20      V31         = -1/2*hbar*Chi_31_1*phase_up - 1/2*hbar*Chi_31_2*
            phase_down ...
21                  -1/2*hbar*Chi_31_3*phase_up - 1/2*hbar*Chi_31_4*
                        phase_down;
22
23      V14         = -1/2*hbar*conj(Chi_41_1)*phase_down - 1/2*hbar*
            conj(Chi_41_2)*phase_up ...
24                  -1/2*hbar*conj(Chi_41_3)*phase_down - 1/2*hbar*
                        conj(Chi_41_4)*phase_up;
25      V41         = -1/2*hbar*Chi_41_1*phase_up - 1/2*hbar*Chi_41_2*
            phase_down ...
26                  -1/2*hbar*Chi_41_3*phase_up - 1/2*hbar*Chi_41_4*
                        phase_down;
27      %% system Hamiltonian
28      Ham = [0      V12   V13   V14    ;
```

```
29              V21   -M1   0     0       ;
30              V31   0     -M2   0       ;
31              V41   0     0     -M3]    ;
32      %% eigen-system
33      [Vector,Value] = eig(Ham);
34      %% find the eigenvalues and corresponding eigen-vectors
35      eig_value_1     = Value(1,1); Time_evo_1 = exp(-i/hbar*
            eig_value_1*tau);
36      eig_value_2     = Value(2,2); Time_evo_2 = exp(-i/hbar*
            eig_value_2*tau);
37      eig_value_3     = Value(3,3); Time_evo_3 = exp(-i/hbar*
            eig_value_3*tau);
38      eig_value_4     = Value(4,4); Time_evo_4 = exp(-i/hbar*
            eig_value_4*tau);
39      %% Time evolution operator
40      Time_evo        = [Time_evo_1 0 0 0;
41                         0 Time_evo_2 0 0;
42                         0 0 Time_evo_3 0;
43                         0 0 0 Time_evo_4];
44      state_inita     = [1;0;0;0];
45      state_final     = Vector*Time_evo*inv(Vector)*state_inita;
46      %% grating operator
47      cg(x_index)     = state_final(1);
48  end
49  end
```

Appendix B

Gauge-transformation

This appendix outlines the gauge-transformations in Chapter 3.

Taylor Series and Translation Operator

The Taylor expansion of an infinitely differentiable function $f(x)$ about a real or complex number a is [139]:

$$\begin{aligned} f(x) = f(a) + f'(a)(x-a) + \frac{f''(a)}{2!}(x-a)^2 + \frac{f^{(3)}(a)}{3!}(x-a)^3 + \cdots \\ + \frac{f^{(n)}(a)}{n!}(x-a)^n + \cdots . \end{aligned} \tag{B.1}$$

Expand the function $f(x+\Delta x)$ around x gives:

$$\begin{aligned} f(x+\Delta x) &= f(x) + \frac{df(x)}{dx}(\Delta x) + \frac{1}{2!}\frac{d^{(2)}f(x)}{dx^2}(\Delta x)^2 + \frac{1}{3!}\frac{d^{(3)}f(x)}{dx^3}(\Delta x)^3 + \cdots \\ &\quad + \frac{1}{n!}\frac{d^{(n)}f(x)}{dx^n}(\Delta x)^n + \cdots \\ &= \sum_{n=0}^{+\infty} \frac{(\Delta x)^n}{n!}\frac{d^{(n)}f(x)}{dx^n} \\ &= \exp\left(\Delta x \frac{d}{dx}\right) f(x). \end{aligned} \tag{B.2}$$

$\exp\left(\Delta x \frac{d}{dx}\right)$ can be viewed as a translation operation that transfers the function $f(x)$ to $f(x+\Delta x)$.

Using the Taylor series in Eq. B.2, we can construct the translation operator $\mathcal{T}(\Delta x)$ that shifts the wave function from $\psi(x)$ to $\psi(x+\Delta x)$ as:

$$\begin{aligned}\mathcal{T}(\Delta x)\psi(x) &= \exp\left(i\frac{\Delta x p}{\hbar}\right)\psi(x)\\ &= \exp\left[i\frac{\Delta x}{\hbar}\left(-i\hbar\frac{d}{dx}\right)\right]\psi(x)\\ &= \exp\left(\Delta x\frac{d}{dx}\right)\psi(x)\\ &= \psi(x+\Delta x),\end{aligned} \tag{B.3}$$

where we use the relation $p=-i\hbar\frac{d}{dx}$. The unitary operator $T^{\dagger}(\Delta x)$ gives:

$$\mathcal{T}^{\dagger}(\Delta x)\psi(x) = \psi(x-\Delta x) \tag{B.4}$$

We can also establish the translation operator $\mathcal{U}(\Delta p)$ to translate a wave function $\phi(p)$ in momentum space:

$$\begin{aligned}\mathcal{U}(\Delta p)\phi(p) &= \exp\left(-i\frac{x\Delta p}{\hbar}\right)\phi(p)\\ &= \exp\left[-i\frac{\Delta p}{\hbar}\left(i\hbar\frac{d}{dp}\right)\right]\phi(p)\\ &= \exp\left(\Delta p\frac{d}{dp}\right)\phi(p)\\ &= \phi(p+\Delta p).\end{aligned} \tag{B.5}$$

where $x=i\hbar\frac{d}{dp}$. The unitary operator $\mathcal{U}^{\dagger}(\Delta p)$ gives:

$$\mathcal{U}^{\dagger}(\Delta p)\phi(p) = \phi(p-\Delta p). \tag{B.6}$$

System Hamiltonian in the laboratory-frame

The Hamiltonian H in Eq. 3.20 is:

$$\begin{aligned}H =& \frac{p^2}{2M} + Mgx - \left(\hbar\Delta + \frac{i\hbar\Gamma}{2}\right)|e\rangle\langle e|\\ &+ \frac{\hbar\Omega}{2}\cos\left[k_L\left(x+\frac{1}{2}at^2\right)\right]\times\left(\sum_{n'=0}^{N}\Pi\left(t-n'T,\tau\right)\right)\left(|e\rangle\langle g| + |g\rangle\langle e|\right).\end{aligned} \tag{B.7}$$

It contains the gravitational potential energy Mgx of the atom where the positive x direction is up when g is positive. The standing wave accelerates downwards when a is positive.

Compared with the Hamiltonian given in Ref. [50], the gravitational potential energy Mgx and the accelerating standing wave break the spatial symmetry of the system. To restore the symmetry and simply the calculation, we will apply a series of gauge-transformations as follows.

We first translate the atomic wave function to a frame that moves at the standing-wave acceleration a in the position space by using the translation operator $\mathcal{T}(\Delta x) = \exp\left(i\frac{\Delta x}{\hbar}p\right)$ (in Eq. B.3) with $\Delta x = \frac{1}{2}at^2$. Using the time evolution of the atomic state ψ:

$$i\hbar\frac{\partial\psi}{\partial t} = H\psi, \tag{B.8}$$

and taking the time derivative of the gauge-transformed state $\widetilde{\psi} = \mathcal{T}^\dagger\psi$ yields:

$$\begin{aligned} i\hbar\frac{\partial}{\partial t}\left[\mathcal{T}^\dagger\psi\right] &= atp\mathcal{T}^\dagger\psi + \mathcal{T}^\dagger H\psi \\ &= atp\mathcal{T}^\dagger\psi + \mathcal{T}^\dagger H\mathcal{T}\mathcal{T}^\dagger\psi \\ &= \left(\mathcal{T}^\dagger H\mathcal{T} + atp\right)\mathcal{T}^\dagger\psi. \end{aligned} \tag{B.9}$$

This means the time evolution of the gauge-transformed state $\widetilde{\psi}$ is governed by the gauge-transformed Hamiltonian $\widetilde{H} = \mathcal{T}^\dagger H\mathcal{T} + atp$. Substituting H of Eq. B.7 in Eq. B.9, we have:

$$\begin{aligned} \widetilde{H} =& \frac{p^2}{2M} + Mg\left(x - \frac{1}{2}at^2\right) + apt - \left(\hbar\Delta + \frac{i\hbar\Gamma}{2}\right)|e\rangle\langle e| \\ &+ \frac{\hbar\Omega}{2}\cos\left(k_L x\right) \times \left(\sum_{n'=0}^{N}\Pi\left(t - n'T, \tau\right)\right)\left(|e\rangle\langle 3| + |3\rangle\langle e|\right). \end{aligned} \tag{B.10}$$

We now outline the detailed derivation of each component in Eq. B.10:

1. The kinetic energy $\frac{p^2}{2M}$:

$$\exp\left(-i\frac{\Delta x}{\hbar}p\right)\left[\frac{p^2}{2M}\right]\exp\left(i\frac{\Delta x}{\hbar}p\right) = \frac{p^2}{2M}. \tag{B.11}$$

The kinetic energy commute with $\mathcal{T}$ and $\mathcal{T}^\dagger$, which leaves it unchanged after the operation since $\mathcal{T}\mathcal{T}^\dagger = I$.

2. The gravitational potential energy Mgx:

$$\begin{aligned}
&\underbrace{\exp\left(-i\frac{\Delta x}{\hbar}p\right)\overbrace{(Mgx)\overbrace{\exp\left(i\frac{\Delta x}{\hbar}p\right)}^{1}f(x)}^{2}}_{3}\\
&=\exp\left(-i\frac{\Delta x}{\hbar}p\right)(Mgx)\,f(x+\Delta x)\\
&=Mg(x-\Delta x)\psi(x),
\end{aligned}\tag{B.12}$$

where $f(x)$ is an arbitrary infinitely differentiable function. The over-braces and under-brace indicate the order that we carry out the operations.

3. The standing-wave light pattern $\cos\left[k_L\left(x+\frac{at^2}{2}\right)\right]$:

$$\begin{aligned}
&\exp\left(-i\frac{\Delta x}{\hbar}p\right)\cos\left[k_L\left(x+\frac{at^2}{2}\right)\right]\exp\left(i\frac{\Delta x}{\hbar}p\right)f(x)\\
&=\exp\left(-i\frac{\Delta x}{\hbar}p\right)\cos\left[k_L\left(x+\frac{at^2}{2}\right)\right]f(x+\Delta x)\\
&=\cos\left(k_Lx\right)f(x).
\end{aligned}\tag{B.13}$$

The procedure is the same as the one used in Eq. B.12.

See Eq. B.10, the standing wave is stationary after the gauge-transformation. But the system is still not spatially periodic due to the Mgx term.

To further simplify $\widetilde{H}$, we apply another gauge-transformation in momentum space, where the translation operator $\mathcal{U}(\Delta p)=\exp\left(-i\frac{x}{\hbar}\Delta p\right)$ (in Eq. B.5) with $\Delta p=Mgt$. Taking the time derivative of $\widetilde{\widetilde{\psi}}=\mathcal{U}^\dagger\widetilde{\psi}$ gives:

$$\begin{aligned}
i\hbar\frac{\partial}{\partial t}\left[\mathcal{U}^\dagger\widetilde{\psi}\right]&=-Mgx\mathcal{U}^\dagger\widetilde{\psi}+\mathcal{U}^\dagger\widetilde{H}\widetilde{\psi}\\
&=-Mgx\mathcal{U}^\dagger\widetilde{\psi}+\mathcal{U}^\dagger\widetilde{H}\mathcal{U}\mathcal{U}^\dagger\widetilde{\psi}\\
&=\left(\mathcal{U}^\dagger\widetilde{H}\mathcal{U}-Mgx\right)\mathcal{U}^\dagger\widetilde{\psi}.
\end{aligned}\tag{B.14}$$

This implies the time evolution of the state $\widetilde{\widetilde{\psi}}$ is governed by the Hamiltonian $\widetilde{\widetilde{H}}=$

$\mathcal{U}^\dagger \widetilde{H} \mathcal{U} - Mgx$. Substituting $\widetilde{H}$ of Eq. B.10 in Eq. B.14, we can get:

$$\begin{aligned}\widetilde{\widetilde{H}} = \frac{p^2}{2M} - (g-a)\,pt + \frac{Mg}{2}(g-3a)\,t^2 - \left(\hbar\Delta + \frac{i\hbar\Gamma}{2}\right)|e\rangle\langle e| \\ + \frac{\hbar\Omega}{2}\cos(kx) \times \left(\sum_{n'=0}^{N} \Pi\left(t - n'T, \tau\right)\right)\left(|e\rangle\langle 3| + |3\rangle\langle e|\right).\end{aligned} \tag{B.15}$$

Here, we also provide derivations for each component in $\widetilde{\widetilde{H}}$, where the method is same as those used in equations from Eq. B.11 to B.13.

1. The kinetic energy $\frac{p^2}{2M}$:

$$\begin{aligned}&\exp\left(i\frac{x}{\hbar}\Delta p\right)\frac{p^2}{2M}\exp\left(-i\frac{x}{\hbar}\Delta p\right)f(p) \\ &= \exp\left(i\frac{x}{\hbar}\Delta p\right)\frac{p^2}{2M}f(p+\Delta p) \\ &= \frac{(p-\Delta p)^2}{2M}f(p) \\ &= \frac{p^2 - 2pMgt + (Mgt)^2}{2M}f(p) \\ &= \left[\frac{p^2}{2M} - pgt + \frac{Mg^2t^2}{2}\right]f(p),\end{aligned} \tag{B.16}$$

where $f(p)$ is an arbitrary infinitely differentiable function in momentum space. We carry out calculation in an order from right to left that is the same as used in Eq. B.12. Comparing the first and last line, we have $\mathcal{U}^\dagger \frac{p^2}{2M}\mathcal{U} = \frac{p^2}{2M} - pgt + \frac{Mg^2t^2}{2}$.

2. The gravitational potential energy Mgx and the standing-wave light pattern $\cos(k_L x)$:

$$\exp\left(i\frac{x}{\hbar}\Delta p\right)Mgx\exp\left(-i\frac{x}{\hbar}\Delta p\right) = Mgx \tag{B.17}$$

$$\exp\left(i\frac{x}{\hbar}\Delta p\right)\cos(k_L x)\exp\left(-i\frac{x}{\hbar}\Delta p\right) = \cos(k_L x) \tag{B.18}$$

Mgx and $\cos(k_L x)$ are the functions of x, which commute with $\mathcal{U}$ and $\mathcal{U}^\dagger$. This leaves them unaltered.

3. *apt* term:

$$\begin{aligned}&\exp\left(i\frac{x}{\hbar}\Delta p\right)(apt)\exp\left(-i\frac{x}{\hbar}\Delta p\right)f(p) \\ &= \exp\left(i\frac{x}{\hbar}\Delta p\right)(apt)f(p+\Delta p) \\ &= \left[a(p-\Delta p)t\right]f(p) \\ &= \left[apt - aMgt^2\right]f(p)\end{aligned} \tag{B.19}$$

The method for getting $\mathcal{U}^{\dagger}(apt)\mathcal{U} = apt - aMgt^2$ is the same as used in Eq. B.16.

Summary

After these two consecutive gauge-transformations, we restore the spatial periodicity of the system, and the position of the standing-wave pattern is time-independent. This comes at the expense of having time dependence during the free evolution. Nevertheless, $\widetilde{\widetilde{H}}$ in Eq. B.15 is desirable for computation since the free evolution only contains p, and can be therefore calculated very efficiently in momentum space. On the other hand, during a pulse, the atom-light interaction is only a function of the position x, which implies we can preform very efficient calculation in position space. The fast-Fourier-Transform allows us to transfer the atomic states between these two spaces efficiently, which means the calculation can be fast.

References

[1] T. P. Heavner, S. R. Jefferts, E. A. Donley, J. H. Shirley, and T. E. Parker, **NIST-F1: recent improvements and accuracy evaluations**, Metrologia, **42**, 411 (2005).

[2] S. Bize, *et al.* **Cold atom clocks and applications**, Journal of Physics B: Atomic, Molecular and Optical Physics, **38**, S449 (2005).

[3] A. D. Cronin, J. Schmiedmayer, and D. E. Pritchard, **Optics and interferometry with atoms and molecules**, Rev. Mod. Phys. **81**, 1051 (2009).

[4] C. L. Degen, F. Reinhard, and P. Cappellaro, **Quantum sensing**, Rev. Mod. Phys. **89**, 035002 (2017).

[5] P. R. Berman, **Atom Interferometry**, Academic, New York, (1996).

[6] M. Landry, **Searching for gravitational waves with LIGO An introduction to LIGO and a few things gravity wave**, LIGO Hanford Observatory, California Institute of Technology

[7] J. Abadie et al. (The LIGO Scientific Collaboration, The Virgo Collaboration), **All-sky search for periodic gravitational waves in the full S5 LIGO data**, Phys. Rev. D **85**, 022001 (2012).

[8] B.P. Abbott, *et al.* (LIGO Scientific Collaboration and Virgo Collaboration), **Observation of Gravitational Waves from a Binary Black Hole Merger**, Phys. Rev. Lett. **116**, 061102 (2016).

[9] B.P. Abbott, *et al.* (LIGO Scientific Collaboration and Virgo Collaboration), **GW151226: Observation of Gravitational Waves from a 22-Solar-Mass Binary Black Hole Coalescence**, Phys. Rev. Lett. **116**, 241103 (2016).

[10] B.P. Abbott, *et al.* (LIGO Scientific and Virgo Collaboration), **GW170104: Observation of a 50-Solar-Mass Binary Black Hole Coalescence at Redshift 0.2**, Phys. Rev. Lett. **118**, 221101 (2017).

[11] B.P. Abbott, *et al.* (LIGO Scientific Collaboration and Virgo Collaboration), **GW170814: A Three-Detector Observation of Gravitational Waves from a Binary Black Hole Coalescence**, Phys. Rev. Lett. **119**, 141101 (2017).

[12] B.P. Abbott, *et al.* (LIGO Scientific Collaboration and Virgo Collaboration), **GW170817: Observation of Gravitational Waves from a Binary Neutron Star Inspiral**, Phys. Rev. Lett. **119**, 161101 (2017).

[13] L. de Broglie, **Recherches sur la Théorie des Quanta (Researches On the quantum theory)**, Ph.D. thesis, Universite de Paris, Paris, France (1924).

[14] S. Chu, C. Cohen-Tannoudji, and W. D. Phillips, **for development of methods to cool and trap atoms with laser light**, The Nobel Prize in Physics 1997.

[15] W. D. Phillips, **Nobel Lecture: Laser cooling and trapping of neutral atoms**, Rev. Mod. Phys. **70**, 721 (1998).

[16] C. N. Cohen-Tannoudji, **Nobel Lecture: Manipulating atoms with photons**, Rev. Mod. Phys. **70**, 707 (1998).

[17] S. Chu, **Nobel Lecture: The manipulation of neutral particles**, Rev. Mod. Phys. **70**, 685 (1998).

[18] P. L. Gould, G. A. Ruff, and D. E. Pritchard, **Diffraction of atoms by light: The near-resonant Kapitza-Dirac effect**, Phys. Rev. Lett. **56**, 827 (1986).

[19] M. Kasevich, and S. Chu, **Atomic interferometry using stimulated Raman transitions**, Phys. Rev. Lett. **67**, 181 (1991).

[20] M. Kasevich and S. Chu, **Measurement of the Gravitational Acceleration of an Atom with a Light-Pulse Atom Interferometer**, Appl. Phys. B **54**, 321-332 (1992).

[21] A. Peters, K. Y. Chung, and S. Chu, **Measurement of gravitational acceleration by dropping atoms**, Nature (London) **400**, 849 (1999).

[22] A. Peters, K.Y. Chung, and S. Chu, **High-precision gravity measurements using atom interferometry**, Metrologia **38**, 25 (2001).

[23] Z. Hu, B. Sun, X. Duan, M. Zhou, L. Chen, S. Zhan, Q. Zhang, and J. Luo, **Demonstration of an ultrahigh-sensitivity atom-interferometry absolute gravimeter**, Phys. Rev. A **88**, 043610 (2013).

[24] T. L. Gustavson, P. Bouyer, and M. A. Kasevich, **Precision Rotation Measurements with an Atom Interferometer Gyroscope**, Phys. Rev. Lett. **78**, 2046 (1997).

[25] E. A. Cornell, W. Ketterle, and C. E. Wieman, **for the achievement of Bose-Einstein condensation in dilute gases of alkali atoms, and for early fundamental studies of the properties of the condensates**, The Nobel Prize in Physics 2001.

[26] S. Chiow, T. Kovachy, H. C. Chien, and M. A. Kasevich, **102 $\hbar k$ Large Area Atom Interferometers**, Phys. Rev. Lett. **107**, 130403 (2011).

[27] S. M. Dickerson, J. M. Hogan, A. Sugarbaker, D. M. S. Johnson, and M. A. Kasevich, **Multiaxis Inertial Sensing with Long-Time Point Source Atom Interferometry**, Phys. Rev. Lett. **111**, 083001 (2013).

[28] H. Müntinga et al., **Interferometry with Bose-Einstein Condensates in Microgravity**, Phys. Rev. Lett. **110**, 093602 (2013).

[29] P. Bouyer, **A New Starting Point for Atom Interferometry**, Physics **6**, 92 (2013).

[30] M. J. Snadden, J. M. McGuirk, P. Bouyer, K. G. Haritos, and M. A. Kasevich, **Measurement of the Earth's Gravity Gradient with an Atom Interferometer-Based Gravity Gradiometer**, Phys. Rev. Lett. **81**, 971 (1998).

[31] J. M. McGuirk, G. T. Foster, J. B. Fixler, M. J. Snadden, and M. A. Kasevich, **Sensitive absolute-gravity gradiometry using atom interferometry**, Phys. Rev. A **65**, 033608 (2002).

[32] F. Sorrentino, A. Bertoldi, Q. Bodart, L. Cacciapuoti, M. de Angelis, Y.-H. Lien, M. Prevedelli, G. Rosi1, and G. M. Tino, **Simultaneous measurement of gravity acceleration and gravity gradient with an atom interferometer**, Appl. Phys. Lett. **101**, 114106 (2012).

[33] F. Riehle, Th. Kisters, A. Witte, J. Helmcke, and Ch. J. Bordé, **Optical Ramsey spectroscopy in a rotating frame: Sagnac effect in a matter-wave interferometer**, Phys. Rev. Lett. **67**, 177 (1991).

[34] A. Lenef, T. D. Hammond, E. T. Smith, M. S. Chapman, R. A. Rubenstein, and D. E. Pritchard, **Rotation Sensing with an Atom Interferometer**, Phys. Rev. Lett. **78**, 760 (1997).

[35] I. Dutta, D. Savoie, B. Fang, B. Venon, C.L. Garrido Alzar, R. Geiger, and A. Landragin, **Continuous Cold-Atom Inertial Sensor with 1 nrad/sec Rotation Stability**, Phys. Rev. Lett. **116**, 183003 (2016).

[36] P. Cladé, E. Mirandes, M. Cadoret, S. Guellati-Khélifa, C. Schwob, F. Nez, L. Julien, and F. Biraben, **Determination of the Fine Structure Constant Based on Bloch Oscillations of Ultracold Atoms in a Vertical Optical Lattice**, Phys. Rev. Lett. **96**, 033001 (2006).

[37] M. Cadoret, E. Mirandes, P. Clad, S. Guellati-Khélifa, C. Schwob, F. Nez, L. Julien, and F. Biraben, **Combination of Bloch Oscillations with a Ramsey-Bord Interferometer: New Determination of the Fine Structure Constant**, Phys. Rev. Lett. **101**, 230801 (2008).

[38] R. Bouchendira, P. Cladé, S. Guellati-Khélifa, F. Nez, and F. Biraben, **New Determination of the Fine Structure Constant and Test of the Quantum Electrodynamics**, Phys. Rev. Lett. **106**, 080801 (2011).

[39] R. H. Parker, C. Yu, W. Zhong, B. Estey, H. Müller, **Measurement of the fine-structure constant as a test of the Standard Model**, Science, **360**, 191, (2018).

[40] J. B. Fixler, G. T. Foster, J. M. McGuirk, and M. A. Kasevich, **Atom Interferometer Measurement of the Newtonian Constant of Gravity**, Science, **315**, 74 (2007).

[41] G. Lamporesi, A. Bertoldi, L. Cacciapuoti, M. Prevedelli, and G. M. Tino, **Determination of the Newtonian Gravitational Constant Using Atom Interferometry**, Phys. Rev. Lett. **100**, 050801 (2008).

[42] G. Rosi, F. Sorrentino, L. Cacciapuoti, M. Prevedelli, and G. M. Tino, **Precision measurement of the Newtonian gravitational constant using cold atoms**, Nature, **510**, 518 (2014).

[43] S. Dimopoulos, P. W. Graham, J. M. Hogan, and M. A. Kasevich, **Testing General Relativity with Atom Interferometry**, Phys. Rev. Lett. **98**, 111102 (2007).

[44] R. Geiger, L. Amand, A. Bertoldi, B. Canuel, W. Chaibi, C. Danquigny, I. Dutta, B. Fang, S. Gaffet, J. Gillot, D. Holleville, A. Landragin, M. Merzougui, I. Riou, D. Savoie, P. Bouyer, **Matter-wave laser Interferometric Gravitation Antenna (MIGA): New perspectives for fundamental physics and geosciences**, arXiv:1505.07137 (2015).

[45] A. Bonnin, N. Zahzam, Y. Bidel, and A. Bresson, **Simultaneous dual-species matter-wave accelerometer**, Phys. Rev. A **88**, 043615 (2013).

[46] H. Müntinga, *et al.*, **Interferometry with Bose-Einstein Condensates in Microgravity**, Phys. Rev. Lett. **110**, 093602 (2013).

[47] A. Sugarbaker, S. M. Dickerson, J. M. Hogan, D. M. S. Johnson, and M. A. Kasevich, **Enhanced Atom Interferometer Readout through the Application of Phase Shear**, Phys. Rev. Lett. **111**, 113002 (2013).

[48] D. Schlippert, J. Hartwig, H. Albers, L.L. Richardson, C. Schubert, A. Roura, W.P. Schleich, W. Ertmer, and E.M. Rasel, **Quantum Test of the Universality of Free Fall**, Phys. Rev. Lett. **112**, 203002 (2014).

[49] G. M. Tino, and F. Vetrano, **Is it possible to detect gravitational waves with atom interferometers?** Classical Quant. Grav. **24**, 2167, (2007).

[50] S. Chai, J. Fekete, P. McDowall, S. Coop, T. Lindballe, and M. F. Andersen, **Survival resonances in an atom-optics system driven by temporally and spatially periodic dissipation**, Phys. Rev. A **97**, 033616 (2018).

[51] S. Chai, J. Fekete, M. F. Andersen, **Measuring the local gravitational field using survival resonances in a dissipatively driven atom-optics system**, submitted to Phys. Rev. A.

[52] S. Fray, C. A. Diez, T. W. Hänsch, and M. Weitz, **Atomic Interferometer with Amplitude Gratings of Light and Its Applications to Atom Based Tests of the Equivalence Principle**, Phys. Rev. Lett. **93**, 240404 (2004).

[53] S. Dimopoulos, P. W. Graham, J. M. Hogan, and M. A. Kasevich, **General relativistic effects in atom interferometry**, Phys. Rev. D **78**, 042003 (2008).

[54] P. Hamilton, M. Jaffe, J. M. Brown, L. Maisenbacher, B. Estey, and Holger Müller, **Atom Interferometry in an Optical Cavity**, Phys. Rev. Lett. **114**, 100405 (2015).

[55] S. Abend, M. Gebbe, M. Gersemann, H. Ahlers, H. Müntinga, E. Giese, N. Gaaloul, C. Schubert, C. Lmmerzahl, W. Ertmer, W.P. Schleich, and E.M. Rasel, **Atom-Chip Fountain Gravimeter**, Phys. Rev. Lett. **117**, 203003 (2016).

[56] J. Schmiedmayer and M. Arndt, **Embracing Quantum Metrology with Wide Arms**, Physics **4**, 74 (2011).

[57] L. Zhou, Z. Y. Xiong, W. Yang, B. Tang, W. C. Peng, K. Hao, R. B. Li, M. Liu, J. Wang, M. S. Zhan, **Development of an atom gravimeter and status of the 10-meter atom interferometer for precision gravity measurement**, General Relativity and Gravitation, **43**, 1931 (2011).

[58] J. E. Debs, P. A. Altin, T. H. Barter, D. Dring, G. R. Dennis, G. McDonald, R. P. Anderson, J. D. Close, and N. P. Robins, **Cold-atom gravimetry with a Bose-Einstein condensate**, Phys. Rev. A **84**, 033610 (2011).

[59] H. Müller, S. Chiow, Q. Long, S. Herrmann, and S. Chu, **Atom Interferometry with up to 24-Photon-Momentum-Transfer Beam Splitters**, Phys. Rev. Lett. **100**, 180405 (2008).

[60] J. Fekete, S. Chai, S. A. Gardiner, and M. F. Andersen, **Resonant transfer of large momenta from finite-duration pulse sequences**, Phys. Rev. A **95**, 033601 (2017).

[61] T. Mazzoni, X. Zhang, R. Del Aguila, L. Salvi, N. Poli, and G. M. Tino, **Large-momentum-transfer Bragg interferometer with strontium atoms**, Phys. Rev. A **92**, 053619 (2015).

[62] https://www.muquans.com/index.php/products/aqg

[63] V. Ménoret, P. Vermeulen, N. L. Moigne, S. Bonvalot, P. Bouyer, A. Landragin, and B. Desruelle, **Gravity measurements below 10^9 g with a transportable absolute quantum gravimeter**, Scientific Reports, **8**, 12300 (2018).

[64] https://aosense.com/applications/geodetic-geophysical-sensors/

[65] A. D. Cronin, and R. Trubko, **More Power to Atom Interferometry**, Physics **8**, 22 (2015).

[66] W. H. Oskay, D. A. Steck, V. Milner, B. G. Klappauf, M. G. Raizen, **Ballistic peaks at quantum resonance**, Optics Communications, **179**, 137 (2000).

[67] M. B. d'Arcy, R. M. Godun, M. K. Oberthaler, D. Cassettari, and G. S. Summy, **Quantum Enhancement of Momentum Diffusion in the Delta-Kicked Rotor**, Phys. Rev. Lett. **87**, 074102 (2001).

[68] S. Wu, A. Tonyushkin, and M. G. Prentiss, **Observation of Saturation of Fidelity Decay with an Atom Interferometer**, Phys. Rev. Lett. **103**, 034101 (2009).

[69] A. Ullah, S. K. Ruddell, J. A. Currivan, and M. D. Hoogerland, **Quantum resonant effects in the delta-kicked rotor revisited**, Eur. Phys. J. D **66**, 315 (2012).

[70] G. Summy and S. Wimberger, **Quantum random walk of a Bose-Einstein condensate in momentum space**, Phys. Rev. A **93**, 023638 (2016).

[71] M. G. Raizen, **Quantum Chaos with Cold Atoms**, Advances in Atomic, Molecular and Optical Physics, **41(C)**, 43 (1999).

[72] F. L. Moore, J. C. Robinson, C. Bharucha, P. E. Williams, and M. G. Raizen, **Observation of Dynamical Localization in Atomic Momentum Transfer: A New Testing Ground for Quantum Chaos**, Phys. Rev. Lett. **73**, 2974 (1994).

[73] F. L. Moore, J. C. Robinson, C. F. Bharucha, Bala Sundaram, and M. G. Raizen, **Atom Optics Realization of the Quantum δ-Kicked Rotor**, Phys. Rev. Lett. **75**, 4598 (1995).

[74] M. Sadgrove, M. Horikoshi, T. Sekimura, and K. Nakagawa, **Rectified Momentum Transport for a Kicked Bose-Einstein Condensate**, Phys. Rev. Lett. **99**, 043002 (2007).

[75] I. Dana, V. Ramareddy, I. Talukdar, and G. S. Summy, **Experimental Realization of Quantum-Resonance Ratchets at Arbitrary Quasimomenta**, Phys. Rev. Lett. **100**, 024103 (2008).

[76] M. K. Oberthaler, R. M. Godun, M. B. d'Arcy, G. S. Summy, and K. Burnett, **Observation of Quantum Accelerator Modes**, Phys. Rev. Lett. **83**, 4447 (1999).

[77] J. F. Kanem, S. Maneshi, M. Partlow, M. Spanner, and A. M. Steinberg, **Observation of High-Order Quantum Resonances in the Kicked Rotor**, Phys. Rev. Lett. **98**, 083004 (2007).

[78] C. Ryu, M. F. Andersen, A. Vaziri,M. B. d'Arcy, J. M. Grossman, K. Helmerson, and W. D. Phillips, **High-Order Quantum Resonances Observed in a Periodically Kicked Bose-Einstein Condensate**, Phys. Rev. Lett. **96**, 160403 (2006).

[79] [7] G. Behinaein, V. Ramareddy, P. Ahmadi, and G. S. Summy, **Exploring the Phase Space of the Quantum δ-Kicked Accelerator**, Phys. Rev. Lett. **97**, 244101 (2006).

[80] P. Szriftgiser, J. Ringot, D. Delande, and J. C. Garreau, **Observation of Sub-Fourier Resonances in a Quantum-Chaotic System**, Phys. Rev. Lett. **89**, 224101 (2002).

[81] I. Talukdar, R. Shrestha, and G. S. Summy, **Sub-Fourier Characteristics of a δ-kicked-rotor Resonance**, Phys. Rev. Lett. **105**, 054103 (2010).

[82] B. Daszuta and M. F. Andersen, **Atom interferometry using δ-kicked and finite-duration pulse sequences**, Phys. Rev. A **86**, 043604 (2012).

[83] P. McDowall, A. Hillard, M. McGovern, T. Grünzweig, and M. F. Andersen, **A fidelity treatment of near-resonant states in the atom-optics kicked rotor**, New J. Phys. 11, 123021 (2009).

[84] Z.-Y. Ma, M. B. d'Arcy, and S. A. Gardiner, **Gravity-Sensitive Quantum Dynamics in Cold Atoms**, Phys. Rev. Lett. **93**, 164101 (2004).

[85] M. Weitz, T. Heupel, and T. W. Hänsch, **Multiple Beam Atomic Interferometer**, Phys. Rev. Lett. **77**, 2356 (1996).

[86] P. D. McDowall, **Atom interferometry using near resonant standing waves of light**, Ph.D. thesis, (2014).

[87] E. Ott, **Chaos in Dynamical System**, Cambridge University Press, Cambridge, UK, (2002).

[88] D. W. Keith, M. L. Schattenburg, Henry I. Smith, and D. E. Pritchard, **Diffraction of Atoms by a Transmission Grating**, Phys. Rev. Lett. **61**, 1580 (1988).

[89] M. S. Chapman, C. R. Ekstrom, T. D. Hammond, J. Schmiedmayer, B. E. Tannian, S. Wehinger, and D. E. Pritchard, **Near-field imaging of atom diffraction gratings: The atomic Talbot effect**, Phys. Rev. A **51**, R14(R) (1995).

[90] R. E. Grisenti, W. Schöllkopf, J. P. Toennies, G. C. Hegerfeldt, and T. Köhler, **Determination of Atom-Surface van der Waals Potentials from Transmission-Grating Diffraction Intensities**, Phys. Rev. Lett. **83**, 1755 (1999).

[91] A. Turlapov, A. Tonyushkin, and T. Sleator, **Optical mask for laser-cooled atoms**, Phys. Rev. A **68**, 023408 (2003).

[92] A. Turlapov, A. Tonyushkin, and T. Sleator, **Talbot-Lau effect for atomic de Broglie waves manipulated with light**, Phys. Rev. A **71**, 043612 (2005).

[93] F. L. Pedrotti, L. M. Pedrotti, and L. S. Pedrotti, **Introduction to optics**, Cambridge University Press, UK (2007)

[94] D. A. Steck. **Rubidium 85 D Line Data**, available online at *http://steck.us/alkalidata/rubidium85numbers.pdf* (revision 2.1.6, 20 September 2013).

[95] D. J. Griffiths, **Introduction to Quantum Mechanics** Prentice Hall, Upper Saddle River, NJ, (1995).

[96] C. J. Foot, **Atomic Physics**, Oxford University Press, New York, (2005).

[97] V. P. Chebotayev, B. Ya. Dubetsky, A. P. Kasantsev, and V. P. Yakovlev, **Interference of atoms in separated optical fields**, J. Opt. Soc. Am. B **2**, 1791 (1985).

[98] P. W. Milonni, and J. H. Eberly, **Lasers**, New York: Wiley, (1988).

[99] P. Meystre, **Atom optics**, Springer Science and Business Media, (2001).

[100] C. Cohen-Tannoudji, J. Dupont-Roc, and G. Grynberg, **Atom-photon interactions: basic processes and applications**, New York : J. Wiley, (1992).

[101] E. W. Weisstein, **Modified Bessel Function of the First Kind**, From MathWorld–A Wolfram Web Resource.

[102] H. Talbot, **Facts relating to optical science**, Philos. Mag. **9** 401-407 (1836).

[103] W. B. Case, M. Tomandl, S. Deachapunya, and M. Arndt, **Realization of optical carpets in the Talbot and Talbot-Lau configurations**, Opt. Express **17**, 20966-20974 (2009).

[104] M. Chapman, C. Ekstrom, T. Hammond, J. Schmiedmayer, B. Tannian, S. Wehinger, and D. Pritchard, **Near-field imaging of atom diffraction gratings: The atomic Talbot effect**, Phys. Rev. A **51** R14 (1995).

[105] S. Nowak, Ch. Kurtsiefer, T. Pfau, and C. David, **High-order Talbot fringes for atomic matter waves**, Opt. Lett. **22**, 1430-1432 (1997).

[106] L. Deng, E. W. Hagley, J. Denschlag, J. E. Simsarian, Mark Edwards, Charles W. Clark, K. Helmerson, S. L. Rolston, and W. D. Phillips, **Temporal, Matter-Wave-Dispersion Talbot Effect**, Phys. Rev. Lett. **83**, 5407 (1999).

[107] E. Lau, **Beugungserscheinungen an Doppelrastern**, Ann. Phys. **6**, 417 (1948).

[108] M. F. Andersen, and T. Sleator, **Lattice Interferometer for Laser-Cooled Atoms**, Phys. Rev. Lett. **103**, 070402 (2009).

[109] S. B. Cahn, A. Kumarakrishnan, U. Shim, T. Sleator, P. R. Berman, and B. Dubetsky, **Time-Domain de Broglie Wave Interferometry**, Phys. Rev. Lett. **79**, 784 (1997).

[110] H. J. Metcalf and P. Straten, **Laser cooling and trapping**, Springer, New York, (1999).

[111] C. Wieman, G. Flowers, and S. Gilbert, **Inexpensive laser cooling and trapping experiment for undergraduate laboratories**, American Journal of Physics **63**, 317 (1995).

[112] J. Dalibard and C. Cohen-Tannoudji, **Laser cooling below the Doppler limit by polarization gradients: simple theoretical models**, J. Opt. Soc. Am. B **6**, 2023-2045 (1989).

[113] P. D. Lett, R. N. Watts, C. I. Westbrook, W. D. Phillips, P. L. Gould, and H. J. Metcalf, **Observation of Atoms Laser Cooled below the Doppler Limit**, Phys. Rev. Lett. **61**, 169 (1988).

[114] P. J. Ungar, D. S. Weiss, E. Riis, and Steven Chu, **Optical molasses and multilevel atoms: theory**, J. Opt. Soc. Am. B **6**, 2058-2071 (1989).

[115] http://www.ni.com

[116] S. Coop, **An Optical Mask for Atomic Interferometry Experiments**, Master thesis, (2014).

[117] H. J. Lewandowski, D. M. Harber, D. L. Whitaker, and E. A. Cornell, **Simplified System for Creating a Bose-Einstein Condensate**

[118] https://www.mdcvacuum.com

[119] https://www.saesgetters.com/products-functions/products/dispensers/alkali-metals-dispensers

[120] P. D. McDowall, T. Grünzweig, A. Hilliard, and M. F. Andersen, **An atomic beam source for fast loading of a magneto-optical trap under high vacuum**, Rev. Sci. Instrum. **83**, 055102 (2012).

[121] Daryl W. Preston, **Dopplerfree saturated absorption: Laser spectroscopy**, American Journal of Physics **64**, 1432 (1998).

[122] D. J. McCarron, S. A. King, and S, L, Cornish, **Modulation transfer spectroscopy in atomic rubidium**, Measurement Science and Technology, **19**, 105601 (2008).

[123] T. Esslinger, F. Sander, A. Hemmerich, T. W. Hänsch, H. Ritsch, and M. Weidemller, **Purely optical dark lattice**, Opt. Lett. **21**, 991-993 (1996)

[124] G. Salomon, L. Fouch, P. Wang, A. Aspect, P. Bouyer, and T. Bourdel, **Gray-molasses cooling of ^{39}K to a high phase-space density**, Europhys. Lett. **104**, 63002 (2013).

[125] G. Colzi, G. Durastante, E. Fava, S. Serafini, G. Lamporesi, and G. Ferrari, **Sub-Doppler cooling of sodium atoms in gray molasses**, Phys. Rev. A **93**, 023421 (2016).

[126] K. S. Johnson, J. H. Thywissen, N. H. Dekker, K. K. Berggren, A. P. Chu, R. Younkin, and M. Prentiss, **Localization of Metastable Atom Beams with Optical Standing Waves: Nanolithography at the Heisenberg Limit**, Science **280**, 1583 (1998).

[127] F. S. Cataliotti, R. Scheunemann, T. W. Hänsch, and M. Weitz, **Superresolution of Pulsed Multiphoton Raman Transitions**, Phys. Rev. Lett. **87**, 113601 (2001).

[128] F. Reiter, A. S. Srensen, P. Zoller and C. A. Muschik, **Dissipative quantum error correction and application to quantum sensing with trapped ions**, Nature Communications **8**, 1822 (2017).

[129] A. Aspect, E. Arimondo, R. Kaiser, N. Vansteenkiste, and C. Cohen-Tannoudji, **Laser cooling below the one-photon recoil energy by velocity-selective coherent population trapping: theoretical analysis**, J. Opt. Soc. Am. B 6, 2112-2124 (1989).

[130] H. Krauter, C. A. Muschik, K. Jensen, W. Wasilewski, J. M. Petersen, J. Ignacio Cirac, and E. S. Polzik, **Entanglement Generated by Dissipation and Steady State Entanglement of Two Macroscopic Objects**, Phys. Rev. Lett. **107**, 080503 (2011).

[131] Y. Lin, J. P. Gaebler, F. Reiter, T. R. Tan, R. Bowler, A. S. Sørensen, D. Leibfried, and D. J. Wineland, **Dissipative production of a maximally entangled steady state of two quantum bits**, Nature (London) **504**, 415 (2013).

[132] M. J. Kastoryano, F. Reiter, and A. S. Sørensen, **Dissipative Preparation of Entanglement in Optical Cavities**, Phys. Rev. Lett. **106**, 090502 (2011).

[133] P. Schindler, J. T. Barreiro, T. Monz, V. Nebendahl, D. Nigg, M. Chwalla, M. Hennrich, and R. Blatt, **Experimental Repetitive Quantum Error Correction**, Science **332**, 1059 (2011).

[134] D. Nigg, M. Müller, E. A. Martinez, P. Schindler, M. Hennrich, T. Monz, M. A. Martin-Delgado, and R. Blatt, **Quantum computations on a topologically encoded qubit**, Science **345**, 302 (2014).

[135] E. Rocco, R. N. Palmer, T. Valenzuela, V. Boyer, A. Freise, and K. Bongs, **Fluorescence detection at the atom shot noise limit for atom interferometry**, New Journal of Physics **16**, 093046 (2014).

[136] D. L. Butts, J. M. Kinast, B. P. Timmons, and R. E. Stoner, **Light pulse atom interferometry at short interrogation times**, J. Opt. Soc. Am. B **28**, 416 (2011).

[137] J. R. Taylor, **An introduction to error analysis: the study of uncertainties in physical measurements**, 2nd ed edn. University Science Books, Sausalito, Calif, (1997).

[138] G. K. Campbell, E. Leanhardt, J. Mun, M. Boyd, E. W. Streed, W. Ketterle, and D. E. Pritchard, **Photon Recoil Momentum in Dispersive Media**, Phys. Rev. Lett. **94**, 170403 (2005).

[139] E. W. Weisstein, **Taylor Series**, from MathWorld–A Wolfram Web Resource. http://mathworld.wolfram.com/TaylorSeries.html